# NICKEL-BASED SINGLE CRYSTAL SUPERALLOYS FOR INDUSTRIAL GAS TURBINES

by

ATSUSHI SATO

A thesis submitted to

The University of Birmingham

for the degree of

DOCTOR OF PHILOSOPHY

Department of Metallurgy and Materials

College of Engineering and Physical Science

The University of Birmingham

September 2011

# Abstract

The oxidation resistance of four prototype single crystal nickel-based superalloys for industrial gas turbine applications is studied. All contain greater quantities of Cr than in most existing single crystal superalloys; two are alloyed with Si, one with Re. To explain the results, the factors known to influence the rate of $Al_2O_3$ scale formation are considered. Models are developed to predict whether any given alloy composition will form a continuous $Al_2O_3$ scale. These are used to rationalise the dependence of $Al_2O_3$ scale formation on alloy composition in these systems.

The mechanical behaviour of a new single crystal nickel-based superalloy for industrial gas turbine applications is also studied under creep and out-of-phase thermomechanical fatigue (TMF) conditions. Neutron diffraction methods and thermodynamic modelling are used to quantify the variation of the gamma prime (γ') strengthening phase around the γ' solvus temperature; these aid the design of primary ageing heat treatments to develop either uniform or bimodal microstructures of the γ' phase. During TMF, localised shear banding occurs with the γ' phase penetrated by dislocations; however during creep the dislocation activity is restricted to the matrix phase. The factors controlling TMF resistance are rationalised.

# Preface

Parts of this thesis have appeared in the following publications:

*Accepted*

- *Sato, A., Chiu, Y. L. and Reed, R. C. (2011). Oxidation of nickel-based single-crystal superalloys for industrial gas turbine applications. Acta Materialia 59(1): 225-240.*

- *Sato, A., Moverare, J. J., Hasselqvist, M. and Reed, R. C. (2011). On the Oxidation Resistance of Nickel-Based Superalloys. Advanced Materials Research 278: p.174-179.*

- *Sato, A., Moverare, J. J., Hasselqvist, M. and Reed, R. C. (2011). On the Mechanical Behaviour of a New Single Crystal Superalloy for Industrial Gas Turbine Applications. Metallurgical and Materials Transaction A: Accepted.*

- *Sato, A., Chiu, Y. L., Marquis, E. A. and Reed, R. C. (2011). On the Alumina Formation of Nickel-Based Single Crystal Superalloys for Industrial Gas Turbines Applications. Materials at High Temperatures: Accepted.*

- *Moverare, J. J., Sato, A., Johansson, S., Hasselqvist, M., Reed, R. C., Kanesund, J. and Simonsson, K. (2011). On Localized Deformation and Recrystallization as a Damage Mechanisms During Thermomechanical Fatigue of Single Crystal Nickel-Based Superalloys. Advanced Materials Research 278: p.357-362.*

- *Moverare, J. J., Sato, A., Hasselqvist, M., Karlsson, F. and Reed, R. C. (2011). A New Single Crystal Superalloy for Power Generation Applications. 8th International Charles Parsons Turbine Conference, Portsmouth, UK, p.G2-2.*

*In Progress*

- *Sato, A. and Reed, R. C. (2011). On the Oxidation Behaviour of Nickel-Based Superalloys for High Temperature Applications. Acta Materialia, in progress.*

- *Bensch, M., Sato, A., Warnken, N., Affeldt, E,. Reed R.C. and Glatzel, U. (2011). On The Modelling of the Oxidation of Single Crystal Superalloys. Acta Materialia: in progress.*

- *Moverare, J.J., Segersäll, M. Sato, A., Johansson, S. and Reed, R.C. (2012). Thermomechanical fatigue of single-crystal superalloys - influence of composition and microstructure. Superalloys2012, in progress.*

# Dedication

To my wife Qian and my children Rin and Rena.

# Acknowledgments

I am hugely grateful for the guidance and advice of my supervisors Prof. Roger C Reed, Prof. Nick R. Green and Prof. Hugh E. Evans without whom this simply would not have been possible. The invaluable advice and support of Dr. Mary P. Taylor, Dr. Yu-Lung Chiu at the University of Birmingham and Dr. Cathie Rae at the University of Cambridge, Prof. Emmanuelle A. Marquis in the University of Michigan is acknowledged.

The authors are grateful to Siemens Industrial Turbomachinery AB in Sweden for sponsoring this work. The invaluable advice and support of Prof. Johan J. Moverare at the Linköping University and Dr. Magnus Hasselqvist, Helena Oskarsson (Manager), Leif Berglin and Dr. Xin-Hai Li at Siemens Industrial Turbomachinery AB in Sweden is acknowledged.

Peter Cranmer at the University of Birmingham for casting, Jeff Sutton at the University of Birmingham for XRD analysis and Zailing Zhu at the University of Birmingham for calculations, Dr. Ming Chu for TEM foil preparation, Mick Wickins for mould preparation, Frank Biddlestone for DSC, Dr. Edward Oliver at the ISIS facility at Rutherford Appleton Laboratory and Dr. David Dye at Imperial College London for in-situ neutron diffractometry are thanked for their invaluable assistance.

# Contents

# Chapter 1. Literature Review

## 1.1 Introduction

A gas turbine engine generates electricity or thrust, for jet propulsion. In simple terms, it produces energy by mixing air and fuel, typically by igniting them in a combustor, see Fig. 1.1. Then, combustion gas rotates turbine blades that are directly linked to its compressor, and is finally released by allowing it to expand to outside pressure. Generally speaking, higher operating temperatures improve the efficiency of a gas turbine, and lower $CO_2$ emission levels. Therefore, superior high temperature materials have been required. The outstanding high temperature properties of nickel-based superalloys make them attractive candidates for gas turbines.

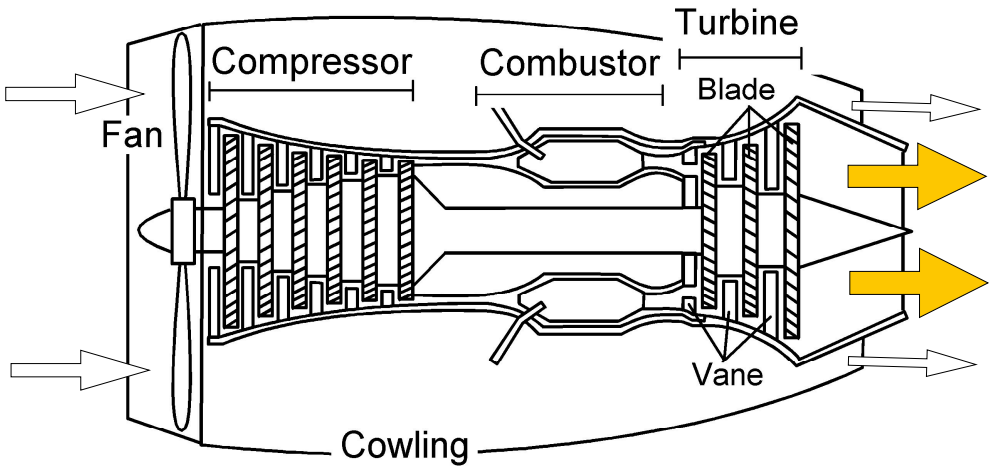


**Fig.1.1 Schematic structure of a typical gas turbine engine.**

## 1.2 Nickel-Based Single Crystal Superalloys

Essential elements in nickel-based superalloy are nickel and aluminium. Aluminium can oxidize to a protective oxide, alumina, at high temperature. Additionally, nickel and aluminium can form the $L1_2$ type intermetallic phase [1], $Ni_3Al$ (Fig.1.2 and 1.3) which confers high temperature strength, particularly in creep and fatigue. Secondly, both nickel solution phase (γ phase) and $L1_2$ phase (γ' phase) have wide range of solution limits. Hence, it is possible to put additional elements in to improve both mechanical and environmental properties. For instance, tungsten, rhenium and tantalum can improve high temperature creep strength. Moreover, chromium improves both oxidation and corrosion resistances.

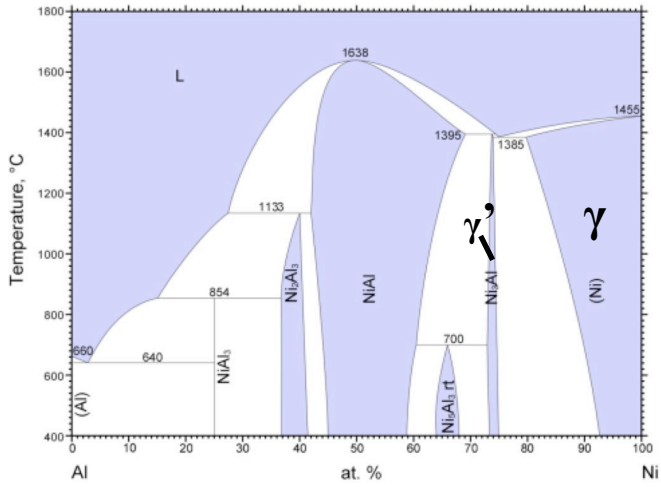


**Fig.1.2 Ni-Al binary phase diagram [2].**

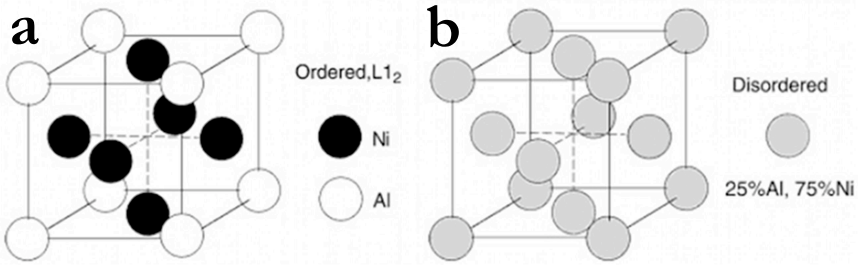


**Fig.1.3 Arrangements of Ni and Al atoms in (a) the ordered $Ni_3Al$ phase and (b) after disordering. Reproduced from [3].**

## 1.2.1 Historical Development of the Superalloys

It is not rare that nickel-based superalloys are cast in single crystal due to some beneficial effects at high temperature. Since 1940s, heat resistance alloys were developed with the addition of nickel and aluminium to improve high temperature properties. For examples, this precursor is now called Nimonic 80 (20Cr-1.2Al-2.4Ti, Ni-bal in wt.%). Then, in order to improve high temperature strength, two methods were attempted: (1) increasing volume fraction of precipitate *f* and (2) increasing the amount of solid solution strengthening elements. However, increases of both (1) and (2) made it harder to produce in wrought due to its forging problem. The technology of vacuum casting had applied since 1950s, and this technology eliminated the compositional limitation due to the forging. The representative of the developed alloy is called IN738LC. Moreover, unidirectional solidification technology was developed in 1970s in US [4], and this technology enabled us to remove whole grain boundaries parallel to stress direction. Grain boundary is known to be the fracture point during creep at high temperature [5]. Therefore, this technology enable to improve the creep properties, especially in its elongation (~4% in conventional cast MarM200 alloy became ~20% in directionally solidified MarM200 alloy at 982ºC [5]). Incidentally, there are grain boundaries remaining parallel to the longitudinal direction, and these different grains have different crystal orientations. This differences caused the different elongation rate during creep; and as a result, the crack propagation to longitudinal direction became a problem. The following idea of single crystal came up to solve this problem. Nickel-based single crystal superalloys does not have grain boundary; therefore, grain boundary strengthening elements such as C and B became no longer necessary. Removing these make them possible to be heat-treated at higher temperature, and help to remove the macro segregation inherited from casting.

## 1.2.2 Superalloys for Industrial Gas Turbines

Historically, nickel-based superalloys have been developed for aeroengines. For instance, a survey in 1980 in the USA indicated that 73% of superalloys are applied for jet engines; on the other hand, 10% are used for industrial gas turbines (IGTs) for power generation [5]. This implies that there were fewer demands of superior nickel-based superalloys for IGTs. Unfortunately, this is the reason why the development of nickel-based superalloys for IGTs are not well developed, see Fig.1.4. Additionally, the environmental properties of nickel-based superalloys for aeroengines is not adequate for IGTs. This is because the usage of engines and fuel types are totally different. For examples, a jet engine requires the highest output for short time (e.g. 10 mins for takeoff). IGTs used with relatively lower output for a long time (e.g. a week continuously). Moreover, high quality of fossil fuel is used for jet engines, but fuels with <10000 ppmw sulphur for IGTs [3].

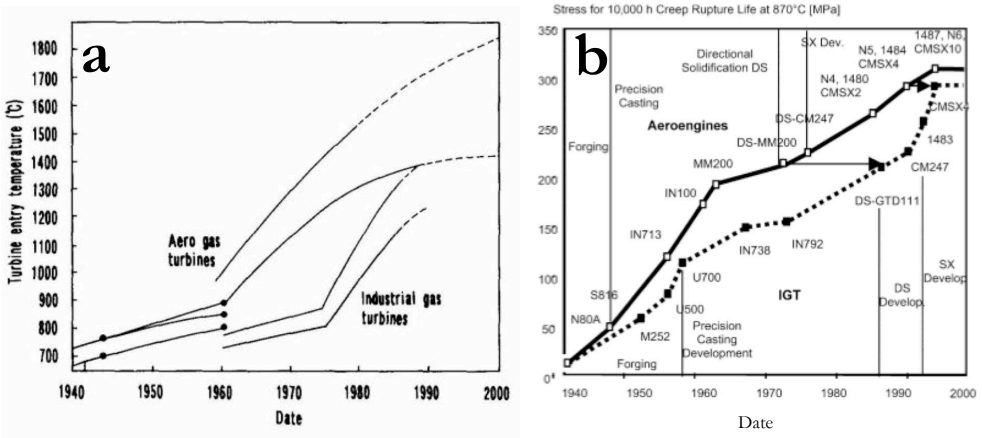


**Fig.1.4. (a) Gas entry temperatures showing the delay in industrial gas turbine technologies, (b) creep rupture strength of materials for aeroengine and industrial gas turbine engine [5, 6].**

# 1.3 High Temperature Oxidation

In order to withstand hot oxidized gas for at least a decade, oxidation is one of the critical requirements for nickel-based superalloys. If insufficient, the turbine blade oxidizes dramatically. The faster this oxidation reaction be, the thinner the turbine blade becomes; resulting in a decreases in mechanical properties within each blade [7]. The following represents a brief yet crucial background to the high temperature oxidation of superalloys.

## 1.3.1 Stability and Driving Force

It should be noticed that even though the industrial materials are exposed to such a high temperature environment, the oxidation reaction is commonly exothermic, i.e. $\Delta G_f$ <0. Here, note that the more $\Delta G_f$ is negative, the more the oxide is stabilised; in other words, the greater the driving force for oxidation. Pure metals' $\Delta G_f$ were summarized in the so-called Ellingham diagram, which is introduced by Ellingham in 1944 and extended by Richardson and Jeffes in 1948. The Ellingham diagram can be used to (i) determine the order of formation of oxides and (ii) determine the partial pressure of oxygen that is in equilibrium with a metal oxide. Note however that it is not always the most stable oxide which becomes the rate-controlling oxide, and the kinetics of oxide growth should be considered.

The Gibbs free energy of formation of the $M_xO_y$ oxide with 1 mol of reactant $O_2$, $\Delta G_f$, can be expanded consistent with the Van't Hoff isotherm [8, 9] according to

$$\Delta G_f = \Delta G_0 + RT \ln\left(\frac{a_{\mathrm{MxOy}}^{2/y}}{a_{\mathrm{M}}^{2x/y} \cdot P_{\mathrm{O_2}}}\right) \tag{1.1}$$

where $\Delta G_0$ is the standard free energy of formation, $T$ is absolute temperature and $R$ is the gas constant. The activity of the oxide of element M is represented by $a_{\mathrm{MxOy}}$ (this is commonly taken to be unity) and $a_{\mathrm{M}}$ is the activity of element M in the multi-component system which is subject to oxidation.

## 1.3.2 Wagner's Theory of Parabolic Oxidation

There are two basic assumptions in the Wagner's theory of parabolic oxidation [10]: (i) theory is valid only for compact scales of reaction products, and (ii) volume diffusion of the reacting ions or the transport of electrons across the scale is rate-determining. Under these assumptions consistent with Fick's first law, the number of molecules of oxygen reacted at time $t$, $dn/dt$, is

$$\frac{dn}{dt} = \frac{1}{e^2 z_a^2 z_c^2} \int_{P_{\mathrm{O}_2}^{ins}}^{P_{\mathrm{O}_2}^{outs}} \sigma_t t_{el} (t_c + t_a) z_c dP_{O_2} \frac{1}{\Delta x} \tag{1.2}$$

where $\Delta x$ is the thickness of oxide, $P_{\mathrm{O}_2}^{outs}$ and $P_{\mathrm{O}_2}^{ins}$ represents the partial pressure of oxygen at outer surface of oxide (ambient/oxide interface which would be 0.2 if air) and inner surface of oxide (oxide/metal interface which can be obtained from Equation 1.1 by placing $\Delta G_f$ equal to zero), respectively. $\sigma_t$ is the conductivity of the $M_xO_y$ oxide and $t_c$, $t_a$ and $t_{el}$ represent the transport numbers ($0 < t < 1$) of cation, anion and electrons, respectively. The metal ion's and the oxygen ion's valences are denoted $z_c$ and $z_a$, respectively; assuming stoichiometric oxide, then $M_xO_y = M_{|z_a|}O_{z_c}$. The elementary charge is represented by $e$. In 1981, de Wit [11] rationalized Wagner's theory of parabolic oxidation with driving force of oxidation, $\Delta G_f$ as follows. The electrical conductivity and

the transport number generally are a function of $P_{O_2}$ ; assuming an average value to these quantities, they can be taken out of the integral in Equation 1.2, *viz.*

$$\frac{dn}{dt} = \frac{\overline{\sigma_t t_{el}(t_c + t_a)}}{e^2 z_a^2 z_c^2 \Delta x} \int_{P_{O_2}^{ins}}^{P_{O_2}^{outs}} z_c dP_{O_2} \tag{1.3}$$

where the over bar indicates that average values are to be taken. By solving the integral term, one has

$$\int_{P_{O_2}^{ins}}^{P_{O_2}^{outs}} z_c dP_{O_2} = z_c \left( P_{O_2}^{outs} - P_{O_2}^{ins} \right) \tag{1.4}$$

Additionally, from classic thermodynamics theory,

$$\Delta G_f = \mu_{M_{|z_a|}O_{z_c}} - |z_a| \, \mu_{Metal} - z_c \, \mu_{O_{vap}} \tag{1.5}$$

$$\mu_{M_{|z_a|}O_{z_c}} = |z_a| \, \mu_{M_{MO}}^{ins} + z_c \, \mu_{O_{MO}}^{ins} \tag{1.6}$$

where $\mu_{M_{|z_a|}O_{z_c}}$ is the chemical potential of the stoichiometric oxide $M_{|z_a|}O_{z_c}$ , $\mu_{Metal}$ is the chemical potential of metal, $\mu_{O_{vap}}$ is the chemical potential of the oxygen, $\mu_{M_{MO}}^{ins}$ is the chemical potential of the metal at the inner interface, $\mu_{O_{MO}}^{ins}$ is the chemical potential of the oxygen at inner interface, respectively. Assuming the local equilibrium at ambient/ oxide and oxide/metal interfaces; then eq.1.5 would be modified as

$$\Delta G_f = \mu_{M_{|z_a|}O_{z_c}} - |z_a| \, \mu_{M_{MO}}^{ins} - z_c \, \mu_{O_{MO}}^{outs} \tag{1.7}$$

Inserting Eq.1.6 to Eq.1.7 then

$$\begin{aligned}\Delta G_f &= \left|z_a\right| \mu_{\mathrm{M_{MO}}}^{ins} + z_c \mu_{\mathrm{O_{MO}}}^{ins} - \left|z_a\right| \mu_{\mathrm{M_{MO}}}^{ins} - z_c \mu_{\mathrm{O_{MO}}}^{outs} \\ &= z_c \mu_{\mathrm{O_{MO}}}^{ins} - z_c \mu_{\mathrm{O_{MO}}}^{outs} \\ &= -z_c \left( \mu_{\mathrm{O_{MO}}}^{outs} - \mu_{\mathrm{O_{MO}}}^{ins} \right)\end{aligned} \tag{1.8}$$

Inserting Eq.1.8 to Eq.1.4, then one can obtain

$$\frac{dn}{dt} = -\frac{\overline{\sigma_t t_{el}(t_c + t_a)}}{e^2 z_a^2 z_c^2 \Delta x} \Delta G_f \tag{1.9}$$

Parabolic oxidation can be commonly described as

$$\frac{dn}{dt} = \frac{k_t}{\Delta x} \tag{1.10}$$

Comparing with Eq.1.9 and Eq.1.10, one can obtain the parabolic oxidation rate $k_t$ as

$$k_t = -\frac{\sigma_t \left(t_a + t_c\right) t_{el}}{z_c^2 z_a^2 e^2} \Delta G_f \tag{1.11}$$

Thus, indeed the parabolic oxidation rate from Wagner's theory is related to the driving force factor $\Delta G_f$. This is further elaborated in chapter 3.

## 1.3.3 Dissolution of Foreign Cations in an Oxide

The presence of foreign cations affects the oxidation rate. For example, see [12], assume that the parent oxide is MO and that small amounts of a foreign element oxide $Mf_2O_3$ are dissolved in MO. The Mf-ions have in this case a valence of +3, and if it is assumed that the Mf-ions occupy normal M-sites in MO, the dissolved Mf-ions will have one positive effective charge each. These additional positive effective charges from $\mathrm{Mf}_{\mathrm{M}}^{\cdot}$ must for electroneutrality reasons be balanced by creation of an equivalent concentration of negative effective charges. If these are electronic defects, the dissolution process may be written

$$\mathrm{Mf_2O_3} \rightleftharpoons 2\mathrm{Mf}_{\mathrm{M}}^{\cdot} + 2e' + 2\mathrm{O_O} + 1/2\ \mathrm{O_2} \qquad (1.12)$$

and thus the electron concentration is increased.

Note that the number of Mf in the left and right terms should be the same due to the *mass balance law* before and after the defect formation (hence the reason for the 2 in front of $\mathrm{Mf}_{\mathrm{M}}^{\cdot}$). Second, because the Mf is going to be located on an M-site in MO, and also 2 of $\mathrm{Mf}_{\mathrm{M}}^{\cdot}$ sites are formed (increase of charges considered separately), then the term of $2O_O$ must be created, consistent with '*a ratios of regular lattice sites law*' (ratio of $2\mathrm{Mf}_{\mathrm{M}}^{\cdot}$ : $2O_O$ should be same as the ratio in the parent oxide i.e. M : O = 1 : 1). Third, to maintain the *mass balance law,* $1/2\ O_2$ term is needed. Finally, to maintain *electroneutrality law* due to an increase of +1 effective charges × 2 holes from $+2\,\mathrm{Mf}_{\mathrm{M}}^{\cdot}$, then 2*e*' (i.e. -2) is present. For further details, readers are referred to [12].

## 1.3.4 Pettit's Oxidation Group I, II & III

Until 1971, Giggins and Pettit [13, 14] summarised the three different oxidation modes observed in the Ni-Al-Cr ternary system. Fig.1.5a represents the representative micrograph of so-called "Group I" oxidation mode observed on Ni-2Cr-4Al alloy after 20 hours at 1000ºC. Note that a thick outer scale of NiO is formed. The sub-scale precipitate below NiO scale was reported to be composed of a mixture of $Cr_2O_3$, $Al_2O_3$ and $Ni(Cr,Al)_2O_4$. Oxidation rates in Group I alloys are the same or even worse than that of pure Ni, see Fig. 1.6; thus Group I type oxidation mode leads to fatal oxidation damage on nickel-based alloys. Fig.1.5b shows the typical cross-section for "Group II" alloys, e.g. Ni-20Cr-2Al after 21 hours at 1100ºC. A continuous $Cr_2O_3$ oxide is present, but thick NiO is not. The oxidation rate of Group II alloys is controlled by the formation of $Cr_2O_3$ (see Fig.1.6). Finally Fig.1.5c illustrates the Group III oxidation mode observed, e.g. on Ni-20Cr-4Al after 20 hours at 1200ºC. Here, $Al_2O_3$ is rate controlling (see Fig.1.6). Typically the oxidation rate for Group III alloys is lower than for those in Group I and II.

One major aim of this work is to shed light on the factors influencing oxide growth on Group III alloys.

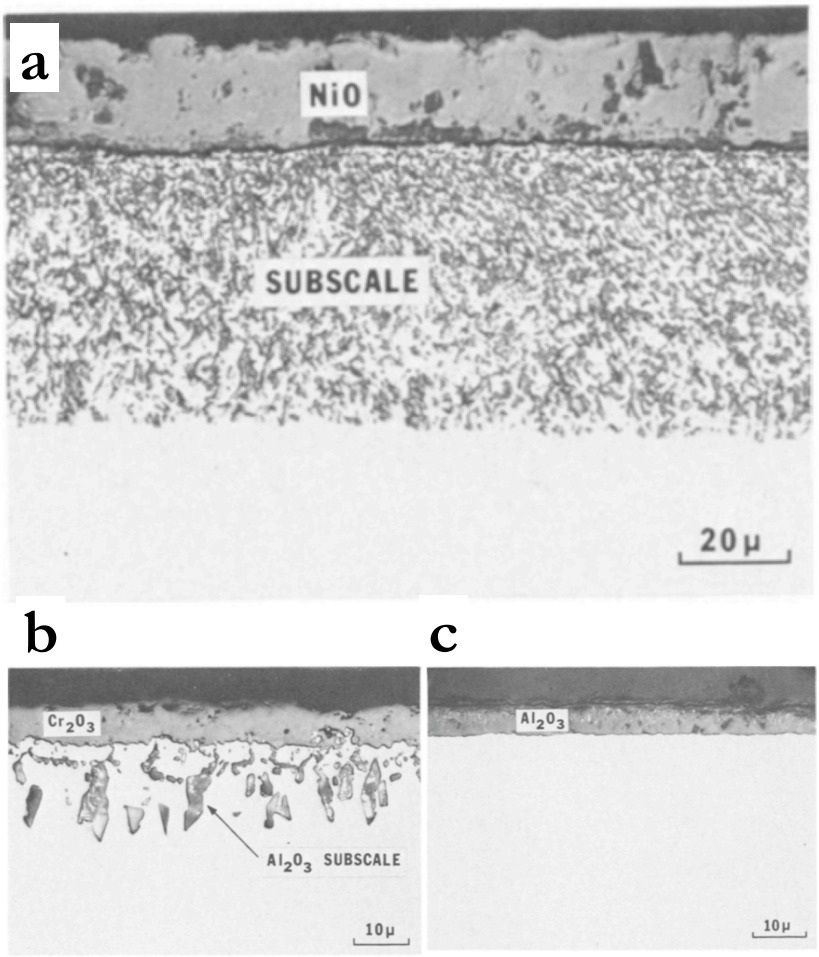


**Fig.1.5 Oxide morphology formed on Ni-Al-Cr alloys exposed at temperature between 1000°C to 1200°C. (a) Group I, (b) Group II and (c) Group III [14].**

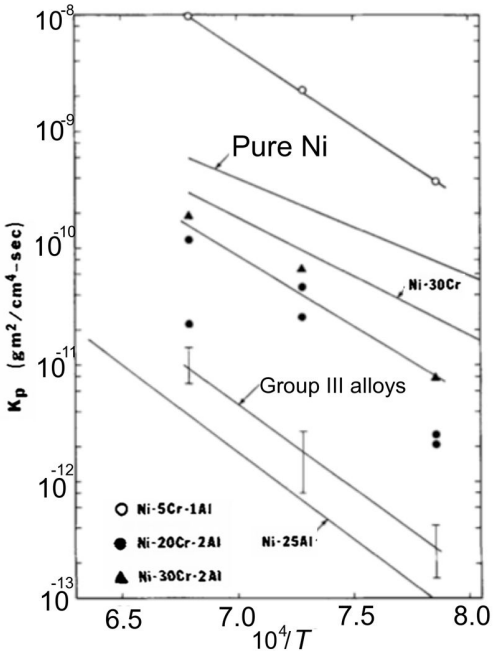


**Fig.1.6 Temperature dependence of the parabolic rate constants obtained for the oxidation of a typical Group I alloy (Ni-5Cr-1Al), Group II alloys (Ni-20Cr-2Al, Ni-30Cr-2Al), and Group III alloys. Parabolic rate constants for the growth of NiO on pure nickel, $Cr_2O_3$ on Ni-30Cr, and $Al_2O_3$ on Ni-25Al are included for comparison[14].**

## 1.3.5 Transport Mechanisms of Alumina and its Transformation

In 1992, Brumm et al. [15] investigated the transformation of $Al_2O_3$ on β-NiAl alloys. The oxidation rates of three different $Al_2O_3$ (γ, θ and α) were summarized on an Arrhenius plot (see Fig.1.7a). γ-$Al_2O_3$ was formed on NiAl during short time oxidation at 900ºC followed by transformation to θ-$Al_2O_3$ after 10 hours. It is suspected that the diffusion in θ-$Al_2O_3$ is faster than that in γ, giving faster oxidation rates. Transformation of θ to α-$Al_2O_3$ is considered to be slow at 900ºC: α-$Al_2O_3$ was detected after 60 hours. Nucleation of α-$Al_2O_3$ is known to take place at the oxide/gas phase boundary. It is also reported that θ-$Al_2O_3$ tends to form whiskers on its surface at both 900 and 1000ºC, despite the fact that it was reported that whiskers appear at temperature up to 950ºC in Ref.[16]. Oxidation rate deceleration in the report of Ref.[17] is considered to be due to the transformation of $Al_2O_3$ from θ to α. Table 1.1 summaries the crystallography of the γ-, θ- and α-$Al_2O_3$ respectively.

The effect of Cr on the transformation of $Al_2O_3$ on NiAl was also reported [15]. No significant effect of Cr was observed on the oxidation rate in the θ-$Al_2O_3$ regime (<900ºC), see Fig.1.7b. The higher the Cr content, the faster the transition time; a resulting increase of the final parabolic oxidation rate in θ/α-$Al_2O_3$ transition regime is observed. The reasons for the increase are suggested to be (i) the presence of $Cr_2O_3$ in the γ or θ-$Al_2O_3$ increase the nucleation site of $Al_2O_3$, then (ii) create finer grain size of $Al_2O_3$. Increase the number of grain boundary (iii) increase the number of diffusion paths for both Al and O; resulting in (iv) the increase of oxidation rate, see Fig.1.8 for this model.

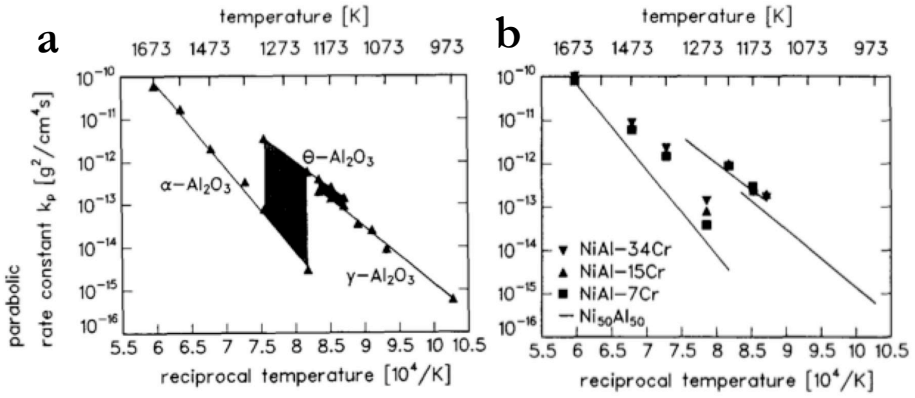


**Fig.1.7 Arrhenius plots of the parabolic rate constants $k_p$ of (a) NiAl and (b) NiAl-Cr alloy, respectively [15].**

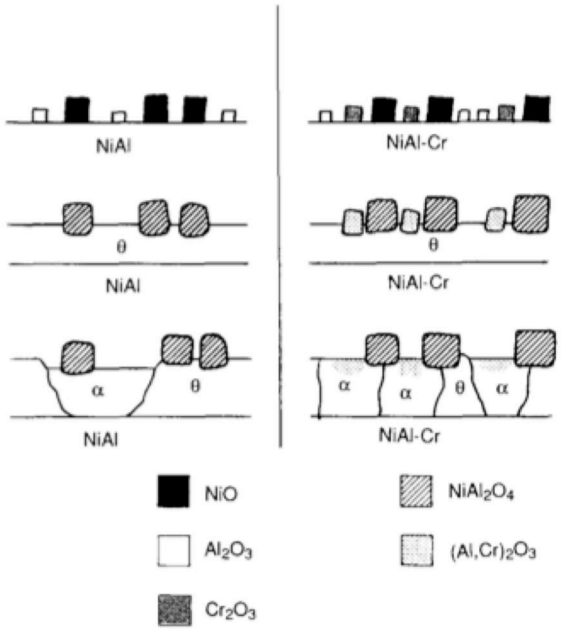


**Fig.1.8 Schematic model of the chromium effect on transformation kinetics [15].**

**Table1.1 Crystallography of the $Al_2O_3$. Refs[18, 19])**

| $Al_2O_3$ | System | Space Group | Space Group No. | Lattice Parameter (nm) | α |
|---|---|---|---|---|---|
| γ | Cubic | Fd-3m | 227 | a=b=c= 0.790 | 90º |
| θ | Monoclinic | C2/m | 12 | a=0.563, b=0.295, c=1.186 | 103.42º |
| α | Hexagonal | R-3c | 167 | a=0.4758, c=1.2991 | 120º |

In 1991, Quadakkers et al. [20] investigated the transport in $Al_2O_3$ on FeCrAl alloys using air/air with $^{18}O$ isotope and secondary neutrals mass spectrometry (SNMS) at temperature between 900ºC and 1100ºC. In this work, alloys were firstly oxidised with $^{18}O$ isotope, followed by with $^{16}O$. In the case of MA956 alloy, there is concentrated $^{18}O$ in the inner side of the scale (Fig.1.9a, Fig.1.9b and Fig.1.9c) with its content slowly increasing from the metal/oxide interface toward the surface; this indicates strongly that grain boundary transport of oxygen is the dominating oxide growth process in this regime (i.e. n-type). However, the shorter the exposure time, the less this M/O interface peaks are at 1000ºC (see Fig.1.9d, Fig.1.9e and Fig.1.9f); implying that the transport in $Al_2O_3$ is time dependent. Both outward aluminium diffusion and inward oxygen diffusion probably both via grain boundary was proposed for the $Y_2O_3$-free Fe-20Cr-5Al alloy (i.e. n/p-type mixture); on the other hand, sole diffusion of oxygen ion at grain boundaries is proposed for the MA956 alloy (n-type). This is supported by the observation of $Y_2O_3$ formation at grain boundary in $Al_2O_3$ of MA956 alloy, which is controlling outward $Al^{3+}$ ion diffusion but enhancing inward $O^{2-}$ diffusion. The effect of $\theta$ to $\alpha$ transformation on the growth mechanism between $Y_2O_3$-free/containing alloys could not verified. Note here that it is also reported by Quaddakkers that the base metal cations dominate the defect structure of the $Al_2O_3$. Fig.1.10 shows the typical example of iron and chromium concentrations in the oxide scale on MA956 after two-stage oxidation at 900ºC (total 45 hours). One can see that the base metal (Fe or Cr) cations in $Al_2O_3$ are typically at levels of 0.5 at.%. Additional analysis by Prescott et al. [21] in 1992 using Auger found that Fe impurity in $Al_2O_3$ on Fe-25Al alloy is 0.1at.%, moreover Ni in $Al_2O_3$ on Ni-32Al is under the detection limit (<0.1at.%).

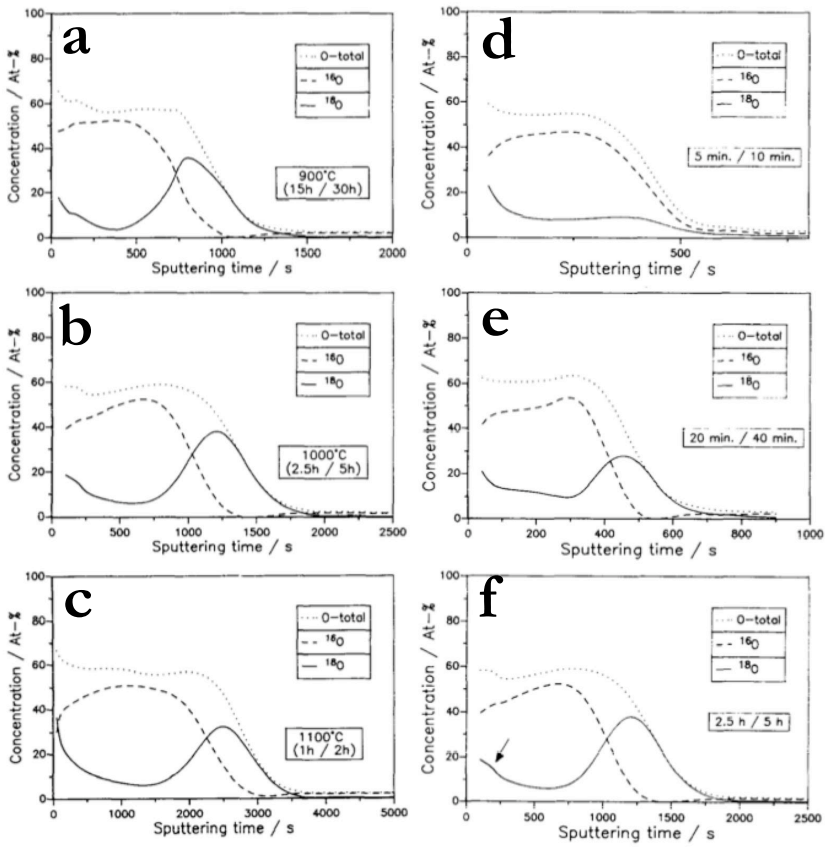


**Fig.1.9 Oxygen isotope distribution in oxide scales of MA956 after two-stage oxidation for *temperature* dependence: (a) 900ºC 15/30 hours, (b) 1000ºC 2.5/5 hours, (c) 1100ºC 1/2 hours, and for *time* dependence: (d) 1000ºC 5/10 mins, (e) 1000ºC 20/40 mins and (f) 1000ºC 2.5/5 hours, respectively. Note that the appearance of $^{18}O$ peak at M/O interface is not obvious in the very early stage of oxidation, see (d), (e) and (f); implying that transport in $Al_2O_3$ is *time* dependent. The sputtering time in the oxide correspond to the distance of around 0.3 nm per sec, but sputter rate in oxide and in the matrix are different [20].**

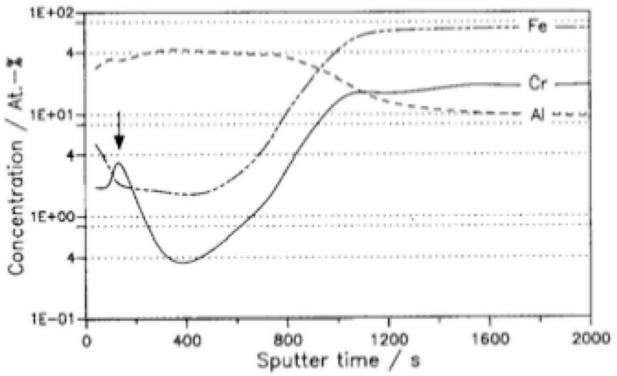


**Fig.1.10 Typical example of iron and chromium concentrations in the oxide scale on MA956 after two-stage oxidation at 900ºC (total 45 hours)[20].**

In 1995, Pint et al. [22] investigated the transport mechanism in θ-$Al_2O_3$ using tracer analysis with oxygen isotope $^{18}O/^{16}O$ and secondary ion mass spectrometry (SIMS). This work confirms that θ-$Al_2O_3$ grows primarily by the outward transport of Al (p-type) rather than inward transport of oxygen commonly seen in the growth of α-$Al_2O_3$ (n-type), see Fig.1.11. A time-temperature-transformation (TTT) diagram for the θ-α transformation was proposed for oxidation on the β-NiAl alloy under 1 atm of dry, flowing $O_2$ ( See Fig. 1.12).

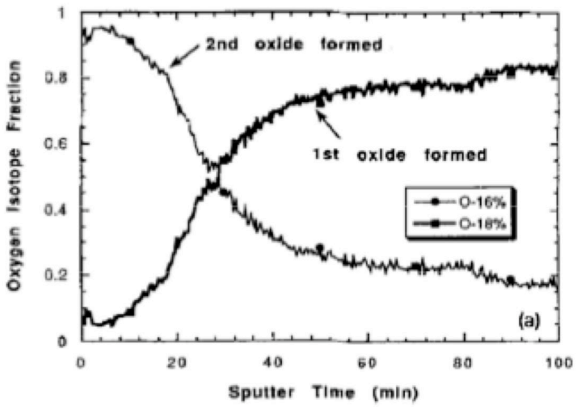


**Fig.1.11 SIMS sputter-depth profiles of the scale formed on MA956 alloy exposed for 1 hour (15mins in $^{18}O$ and 45mins in $^{16}O$) at 950°C [22]. The second oxidant $^{16}O$ is found primarily near the surface, indicating that the scale grows primarily by the outward diffusion of Al.**

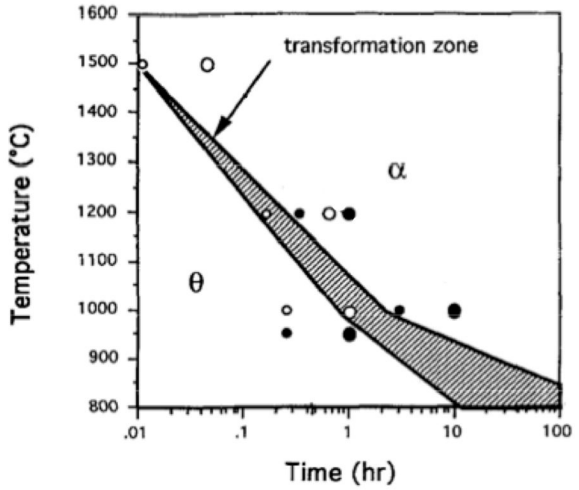


**Fig.1.12 Approximate time-temperature dependence of the formation of θ- and α-$Al_2O_3$ on the polycrystalline β-NiAl [22].**

## 1.3.6 Chromium Oxide

Due to its importance in corrosion resistance, the formation of chromium oxide is also reviewed. Electrical conductivity of chromia ($Cr_2O_3$) can be classified into two distinct groups [12]: a high temperature group above 1000ºC, and a lower temperature group below that. The electrical conductivity exhibits no oxygen pressure dependence at higher temperature, but there is a small pressure dependence in the low temperature regime. Secondly, high-temperature oxidation of pure Cr involves growth of $Cr_2O_3$ scales. The oxidation is controlled by outward migration of Cr-ions (p-type), as indicated by Pt-makers studies; this is because Cr can diffuse 3 orders of magnitude faster than oxygen diffusion. It is also reasonable to assume that the self-diffusion coefficient is independent of oxygen pressure; furthermore, considering Wagner's theory, then $k_p \propto \log P_{O_2}^{outs}$ where $P_{O_2}^{outs}$ is the partial pressure of oxygen at outer metal/oxide interface; thus, a pressure dependence is expected on the oxidation rate, but it may be small at high oxygen pressures.

Small alloying elements can affect oxidation rates of Cr. For example, Hagel [23] found that Li (valence of 2+) doped chromium and Cr with 0.5wt.%Fe had parabolic rate constants smaller by about a factor of ten compared to unalloyed Cr. Trivalent alloying element additions to Cr did not significantly affect the oxidation rate (Cr is also 3+). Ti alloying additions (valence of 4+) were found to increase the oxidation rate [24].

Note that Caplan et al. [25] and Tedmon [26] found that $Cr_2O_3$ can further oxide to $CrO_3$, which is in the gaseous state at temperatures above 1000ºC. Therefore, in general, $Cr_2O_3$ is not considered as the stable oxide at 1000ºC or higher.

## 1.4 High Temperature Deformation

In the gas turbine engine, alloys used for guide vanes must be chosen largely for their oxidation resistance; however, blade alloys should also endure the stress arising from centrifugal loading. Materials will mostly be under isothermal stress states at high temperature, so that creep extension is a possibility. Creep [5] is defined as time-dependent strain occurring under a stress which is lower than the yield stress. Metals with higher melting point tend to exhibit better creep resistance, largely because the self-diffusion is strongly correlated with the homologous temperature. Creep deformation can be ignored at lower temperatures but, fatigue may be a problem there. This is because stress can increase locally to cause plastic deformation, which in turn leads to fatigue cracking. The following consideres on isothermal and non-isothermal deformation of nickel-based superalloys.

## 1.4.1 Creep Deformation

In 1966, Mclean [27] summarised creep deformation as follows. If $T_M$ is the melting point of the metal in question, the different regimes roughly cover the temperature ranges of 0-0.3$T_M$, 0.3-0.5$T_M$, 0.5-0.9$T_M$ and 0.9-1.0$T_M$. It is the middle two temperature ranges which are of prime concern in gas turbine engineering. Creep become significant at temperature above 0.56$T_M$ (>650ºC) in the case of nickel-based superalloys; hence the third group (i.e. 0.5-0.9$T_M$) should be specifically considered. Here, exclusively at above 0.5$T_M$, steady state creep rate can be expressed by the self-diffusion in simple metals, indicating that climb of dislocations is the process controlling the rate of recovery.

In 2009, Dyson [28] made a comprehensive review of creep rate in nickel-based superalloys at temperature range from 600ºC to 900ºC (0.5-0.7$T_M$). No γ' shearing is considered. As above, climb of dislocation (Fig.1.13) is considered to be the rate-controlling process, but only when the glide rate in the matrix is fast enough. If so, the creep rate can be estimated in terms of a diffusion coefficient (demonstrated in Ref. [29]) and a hyperbolic function of the γ' interspacing. On the other hand, when the glide rate is slow (when applied stress is low) then creep shear rate is controlled by general steady state creep rate, $b\rho v$ ,where, $b$ is burgers vector, ρ is the dislocation density, $v$ is the average velocity of dislocation motion (i.e. glide rate) within the matrix. Good agreement between experiment and calculation was observed for the minimum creep rate (see Fig.1.14). Note however that this model is only applicable when the applied stress is low; in the case of high stress, particle shearing or Orowan looping should be considered.

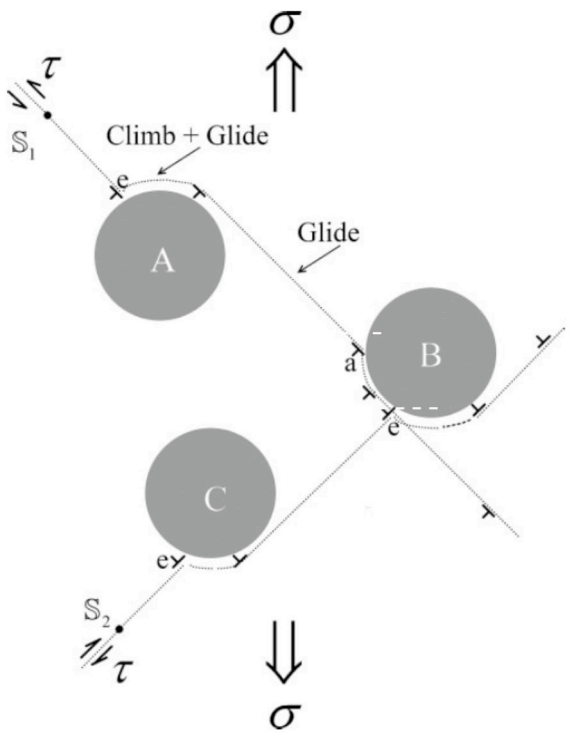


**Fig.1.13 Schematic illustration of particle strengthened alloy, loaded under uniaxial tension, with interparticle spacing, smaller than dislocation spacing [28].**

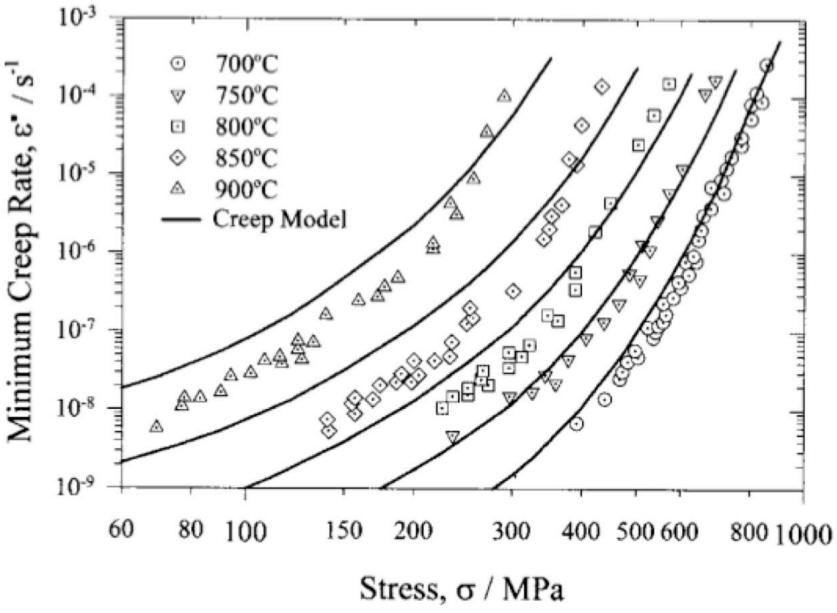


**Fig.1.14 Comparison of industry generated minimum creep rate data of Nimonic 90 in temperature range 700-900°C, with predictions of dispersion controlled creep model [28].**

## 1.4.2 Effect of Microstructure on Creep

In 1983, Caron & Khan [30] investigated the effect of microstructure on creep deformation on single crystal superalloy CMSX-2 at conditions of 760ºC/760MPa and 1050ºC/120MPa, respectively. Note that both condition is above $0.5T_M$. The uniform distribution of γ' (Fig.1.15c) was found to perform better than irregular distributions (Fig. 1.15a) for all creep conditions. In the low temperature/high stress regime, shearing of precipitates occurs, together with homogenous deformation in the uniform microstructure which is believed to confer lower creep rate than for irregular distributions (see Fig.1.16). Here, higher stabilities of dislocation networks were found at the γ/γ' interfaces in uniform microstructure, see Fig.1.15d. At high temperature/low stress regime, it is believed that the perfection of the rafting structure (this will be reviewed shortly) contributed to the lower creep rate.

Considering the fact that dislocation bowing occurs preferentially at largest precipitate interspacing (when the Orowan stress [31] will be lowest), then an irregular distribution possesses more weak points for creep deformation than the uniform distribution. From this point of view, it is likely that uniform microstructure is superior because lower minimum γ' inter spacing can be achieved.

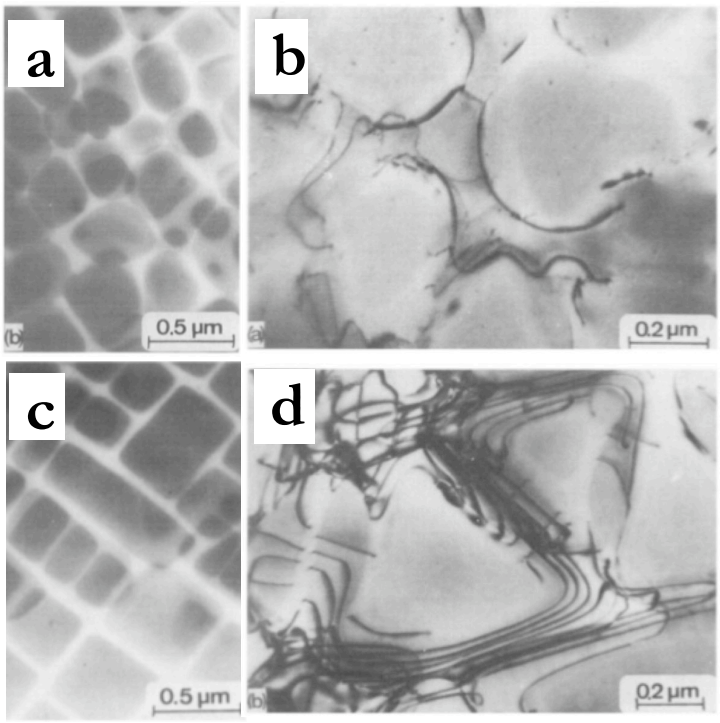


**Fig.1.15 TEM micrographs of CMSX-2 with (a) irregular spherical distribution ($T_1$), (b) dislocation configuration around irregular distribution precipitate in primary creep, (c) uniform cuboidal distribution ($T_2$) and (d) dislocation configurations around spherical precipitates in primary creep. Creep condition: 760ºC/750MPa. The foils in (b) and (d) are from the [111] plane [30].**

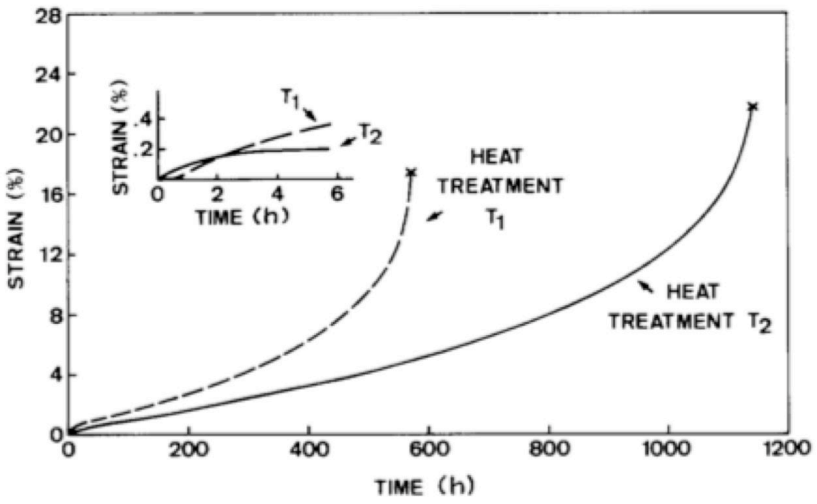


**Fig.1.16 Creep curves for CMSX-2 at 760ºC/750MPa. $T_1$: Irregular spherical distribution, $T_2$: Uniform cuboidal distribution [30].**

## 1.4.3 Effect of Rafting on Creep

The effect of directional coarsening (known as rafting) on the mechanical properties of nickel-based superalloys is controversial; thus this should be reviewed with caution. Most commercial superalloys have negative misfit; in this case, rafting is known to improve the tensile creep performance in the high temperature/low stresses regime when dislocations climb over the γ' particles. On the other hand, it is detrimental in the low temperatures/ high stresses regime when dislocations cut the γ' particles [5]. The formation of rafts improves the creep rupture life under creep conditions of 1050ºC/120MPa (Fig.1.17a); yet, pre-rafted microstructure ($T_4$ in Fig.1.17b) is inferior than cuboidal ($T_2$) at 850ºC/500MPa [32].

Secondly, it has also been found that dislocation glide+climb motion along γ/γ' interface with axis parallel to the <001> direction is considerably slower than along the interface with axis perpendicular to the <001> [33]. This implies that rafts parallel to the stress axis should retard creep. Since only small creep strains are tolerated in practice (<1-2%), pre-rafting in compression does offer an advantage (see Fig.1.18) [34]. This also means that a positive misfit superalloy has potential to offer better creep resistance than a negative one in principle; however, as the additions of most strengthening elements for nickel-based superalloys tends the γ/γ' misfit to the negative, this becomes less likely in practice.

Finally, having larger negative misfit has been reported to increase creep resistance (Fig. 1.19) [35] by the formation of a denser dislocation network at the γ/γ' interface (Fig.1.20) [36-39]. The influence of phase stabilities on minimum creep rate should also be taken into account [40]; both CMSX-10 [41] (see Fig.1.21) and TMS-138 [42, 43] are prone to form topologically closed packed (TCP) phases, see Fig.1.20.

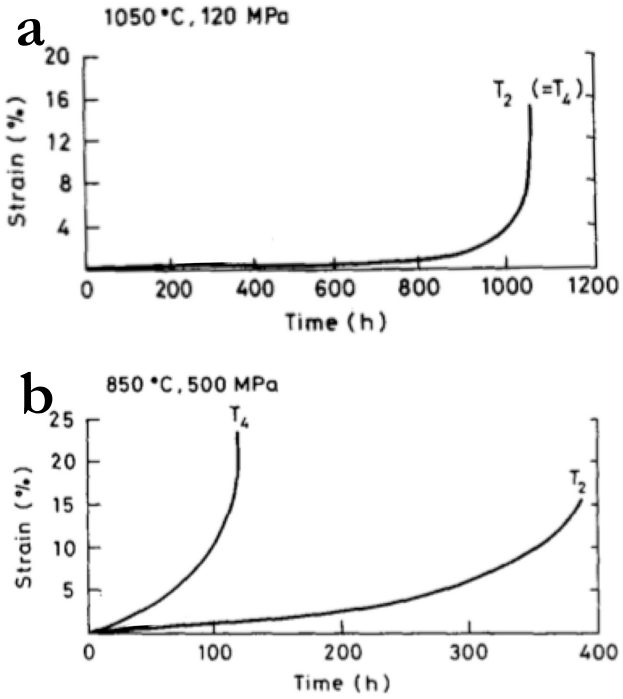


**Fig.1.17 Creep curves for CMSX-2 after various heat treatments (a) 1050ºC/120MPa and (b) 850ºC/500MPa. Note that pre-rafted microstructure ($T_4$) is produced from uniform cuboidal distribution ($T_2$) by applying 1050ºC/120MPa for 15 hours. Reproduced from [32].**

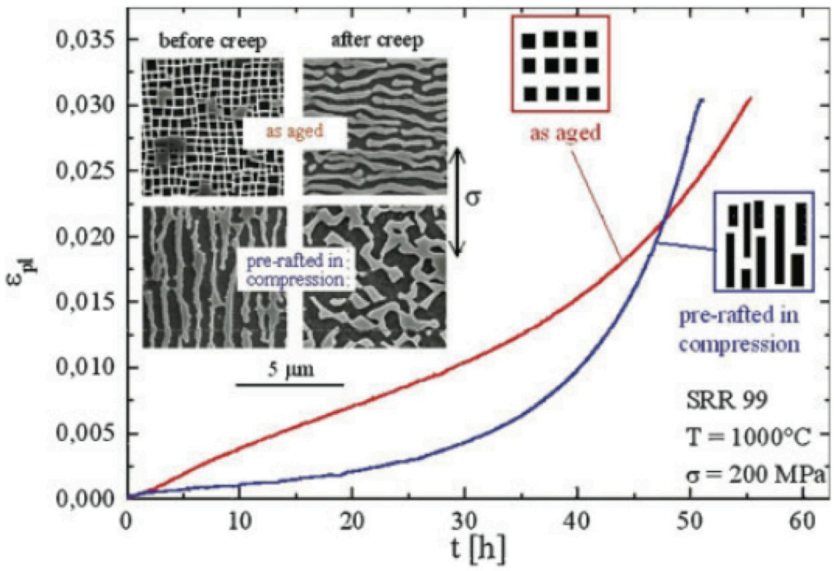


**Fig.1.18 Comparison of tensile creep behaviours of single crystals of the superalloy SRR99 with initial as aged γ/γ' microstructure and with initial γ/γ' microstructure pre-rafted in compression: insets show initial microstructures before and after creep for both cases [33, 34].**

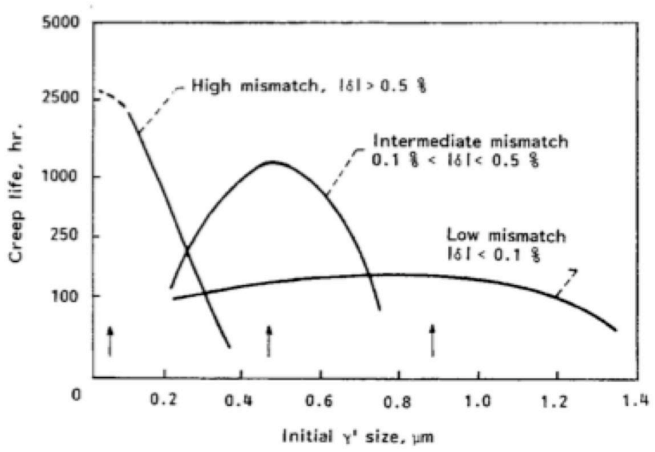


**Fig.1.19 Creep lives for alloys with various misfit and initial γ' sizes. The alloys with large misfits have the longest creep lives [35]. Note that alloys with volume fraction of around 56% are summarised.**

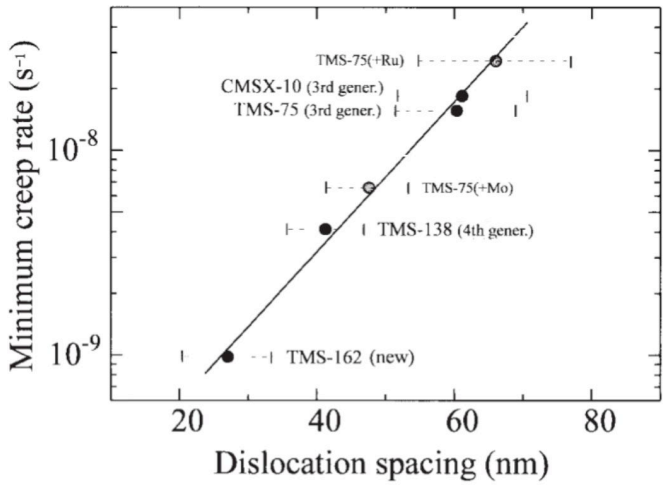


**Fig.1.20 Minimum creep rates of CMSX-10, TMS-75 (with and without Ru or Mo), TMS-138 and TMS-162 as a function of their interfacial dislocation spacing [39].**

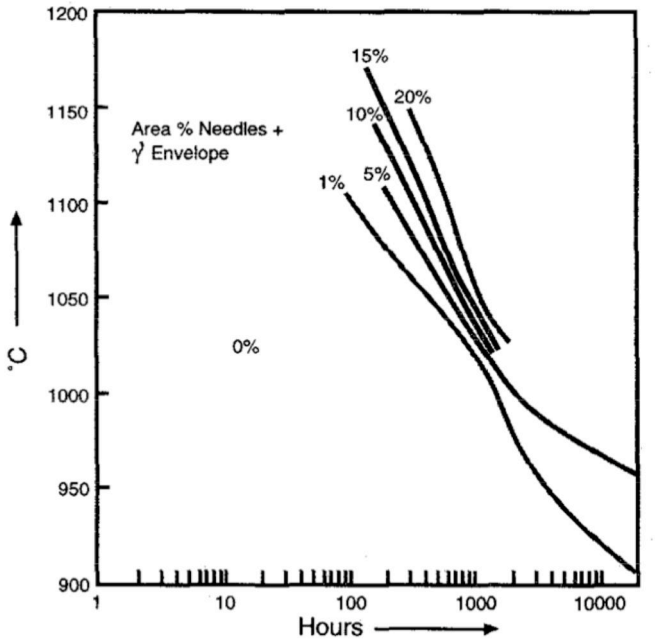


**Fig.1.21 TTT diagram for TCP phase formation in CMSX-10 [41].**

## 1.4.4 Directional Coarsening Mechanism

In 1994, Pollock and Argon [31] published a seminal paper in the driving force of the rafting formation on the high γ' volume fraction containing superalloy CMSX-3. It demonstrated that the driving force for rafting in negative misfit alloys under tensile stress comes from the preferential dissolution of precipitates adjacent to the horizontal channels and by subsequent diffusional flow of precipitate alloying element toward the vertical channels and matrix alloying elements toward the horizontal channels (Fig.1.22). This diffusion process is driven by the interfacial dislocation as a result of the initiation of local creep flow, involving sources and sinks and/or diffusional conduits.

To sum up, rafting can easily be achieved at higher temperature due to higher effective diffusion rate. The time to initiate rafting $t$ can be described as $t = d^2/D_{\text{eff}}$ where $d$ is the diameter of the γ' phase (minimum diffusion distance required to raft), and $D_{\text{eff}}$ is the effective diffusion coefficient at the creep temperature (because matrix preferentially contains slower diffusion elements such as Re). From the above, a smaller precipitate size is clearly beneficial for promoting raft formation.

The influence of γ' distribution on the formation of rafting is considered as follows. Firstly, it is known that secondary γ' is dissolved during high temperature creep (for example at 1150ºC [44]) and will re-precipitate upon cooling (Fig.1.23). In other words, secondary γ' does not raft at high temperature, but primary γ' does. Furthermore, it is suggested that matrix coalescence will be more difficult with widely dispersed precipitates in low volume fraction alloys. Then it is concluded that the rafting structure can be promoted when the interspacing of primary γ' is short.

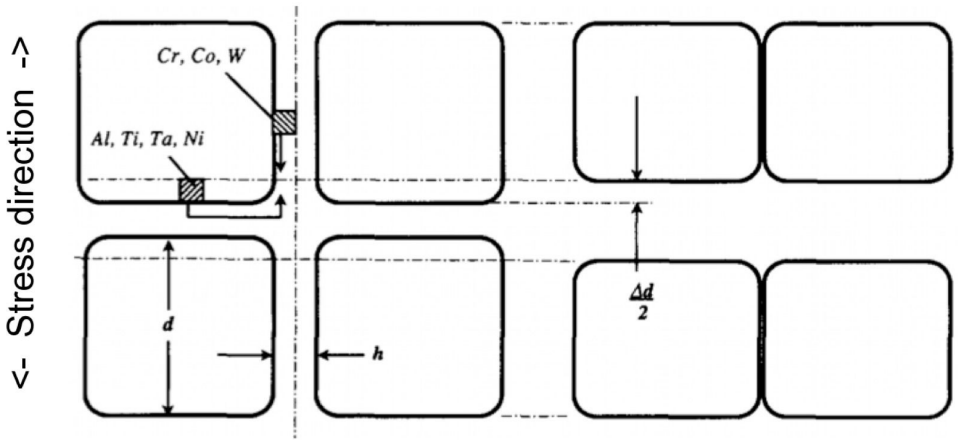


**Fig.1.22 Directional coarsening by preferential dissolution along the horizontal matrix channels and coalescence in the vertical matrix channels [31].**

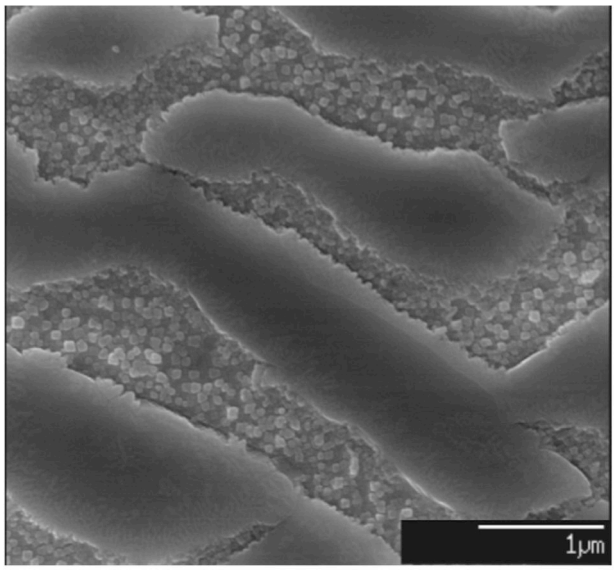


**Fig.1.23 Secondary electron micrograph of rafted CMSX-4 crept at 1150°C/100MPa showing the precipitation of secondary γ' upon cooling [44].**

## 1.4.5 Precipitation Hardening

It has been mentioned in previous sections that the 0.3-0.5$T_M$ and 0.5-0.9$T_M$ ($T_M$: melting point) are the important temperature ranges for materials used in practice. The deformation in the higher temperature range has reviewed already based upon creep theory; yet the lower temperature (0.3-0.5$T_M$) will be considered in this section. It was mentioned that cross slip of dislocations would be more important than climb in the lower of these ranges due to lower activation energy of diffusion than that at 0.5-0.9$T_M$ [5, 27]. Hence, creep deformation (section 1.4.1-1.4.4) will be unimportant at <0.5$T_M$. Instead, flow stress or yield strength should be considered. In general, alloys can be strengthened significantly by dislocation obstacles such as $Ni_3Al$ (γ'), see Fig.1.24 [3, 45].

In the case of nickel-based superalloys, the maximum peak strength is found around 800ºC i.e. $T_M \approx 0.6$ (see Fig.1.25) [3]. Below this temperature, by assuming the square lattice array of precipitate, i.e. extremely uniform distribution of γ' (Fig.1.26), critical resolved shear stress (CRSS), $\tau_{CRSS}$ for weakly coupled dislocation can be described as [3, 46];

$$\tau_{CRSS} = \frac{\gamma_{APB}}{2b}\left(\left(\frac{6\gamma_{APB} fr}{\pi T}\right)^{1/2} - f\right) \tag{1.13}$$

where $\gamma_{APB}$ is the anti-phase boundary (APB) energy, $b$ is Burgers vector, $r$ is the radius of the precipitate, and $f$ is the volume fraction of precipitate, respectively. Note that when the chemical composition of material is identical, the APB energy and $f$ will be constant; thus, CRSS should be a sole function of $\sqrt{r}$. In the case of strongly coupled dislocations, readers are referred to [46-48].

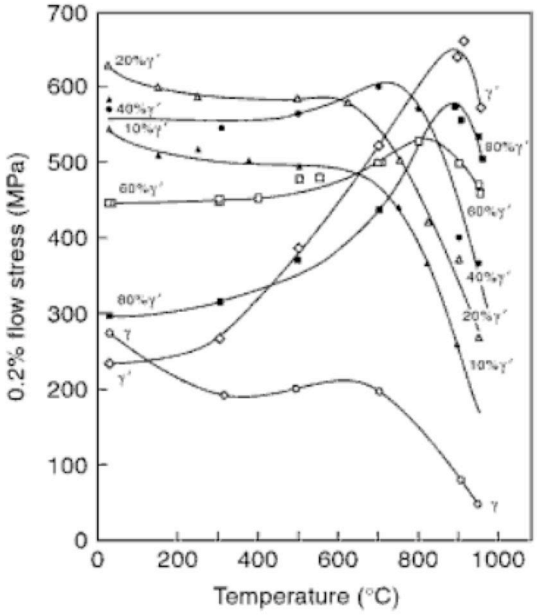


**Fig.1.24 Variation of the yield stress with temperature for alloys with different γ' volume fraction[3].**

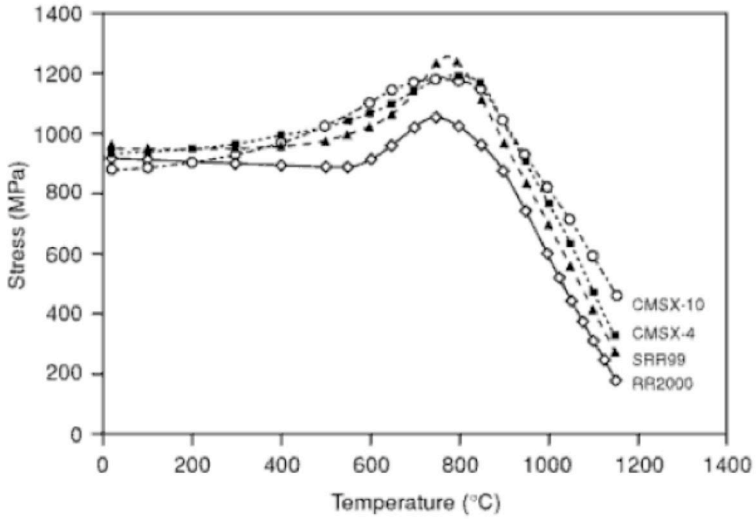


**Fig.1.25 Variation of the yield stress of a number of single-crystal superalloys with temperature [3].**

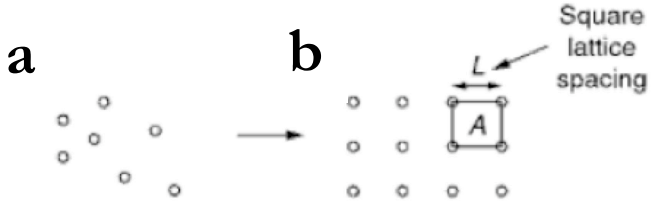


**Fig.1.26 Representation of a random distribution of γ' particles on the slip plane, (a) by a 'square lattice array' (b) such that the number density is identical in both cases[3].**

## 1.4.6 Total Strain under Isothermal Fatigue

Fatigue deformation occurs only when plastic strain is generated, and this can be caused by stress localisation even though the nominal applied stress are below the yield strength [3, 49]. Hence the elastic strain term also should be taken into account.

Under isothermal strain-controlled fatigue, the total strain range $\Delta\varepsilon_{tot}$ is given by the sum of the elastic and plastic strain ranges ($\Delta\varepsilon_e$ and $\Delta\varepsilon_p$) according to [49]

$$\Delta\varepsilon_{tot} = \Delta\varepsilon_e + \Delta\varepsilon_p \tag{1.14}$$

Here, $\Delta\varepsilon_e$ can be obtained from Hooke's law ($=\Delta\sigma_e/E$). Also, $\Delta\varepsilon_p$ can be calculated by Coffin-Manson's law, and also experimentally obtained from the width of stress-strain hysteresis loop at zero stress. Furthermore, $\Delta\varepsilon_{tot}$ can be described with the extension of Coffin-Manson's law together with elastic term and number of cycles to failure $N_f$ as [50]

$$\Delta\varepsilon_{tot} = c_e \cdot N_f^a + c_p \cdot N_f^b \tag{1.15}$$

where $a$ and $b$ are the fatigue strength exponent and fatigue ductility exponent, and reported to be around -0.12 and -0.6, respectively. Furthermore, $c_e$ and $c_p$ are the fatigue strength coefficient and fatigue ductility coefficient, respectively. These can be influenced not only by materials, but also by testing condition, and thus need to be found experimentally.

## 1.4.7 Mechanical Strain under Thermomechanical Fatigue

In practice, the applied load/strain and temperature can be altered independently. This case is known as *thermomechanical* fatigue (TMF) [34, 51, 52], and should be distinguished from the isothermal case. In-phase (IP) TMF is defined when strain increases with increasing temperature (Fig.1.27a); also, out-of-phase (OP) when strain decreases with increasing temperature (Fig.1.27b). OP-TMF is rather detrimental [53, 54], because the oxide is in tension at low temperatures when the oxide has insufficient ductility to prevent cracking (Fig.1.28), and has been often considered [55-60]. In the case of TMF, the internal stress arising due to the thermal expansion should be taken into account. Mechanical strain, $\varepsilon_{mech,}$ is defined by subtracting the thermal strain, $\varepsilon_{th,}$ from total strain $\varepsilon_{tot}$ and can be described as

$$\varepsilon_{mech} = \varepsilon_{tot} - \varepsilon_{th} = \varepsilon_{tot} - \alpha (T - T_0) \tag{1.16}$$

where $T_0$ is the reference temperature at the beginning of the test, $T$ is the test temperature and $\alpha$ is the thermal expansion coefficient [55]. The mechanical strain can be considered to be the same as the total strain (Equation 1.15) in isothermal fatigue testing [61]. Likewise the inelastic strain $\varepsilon_{in,}$ can be experimentally obtained from the width of stress-strain hysteresis loop at zero stress. Note that inelastic strain range includes the plastic strain, creep strain and other strain component such as transformation strain. When mechanical strain ranges are plotted against number of cycles to failure, the result may be on curved lines when influenced by both elastic + inelastic material parameters [49]. Also when $\Delta\varepsilon_e > \Delta\varepsilon_{in}$ which occurs when $\Delta\varepsilon_{mech}$ is small enough, one can expect that the strong materials perform better than ductile ones.

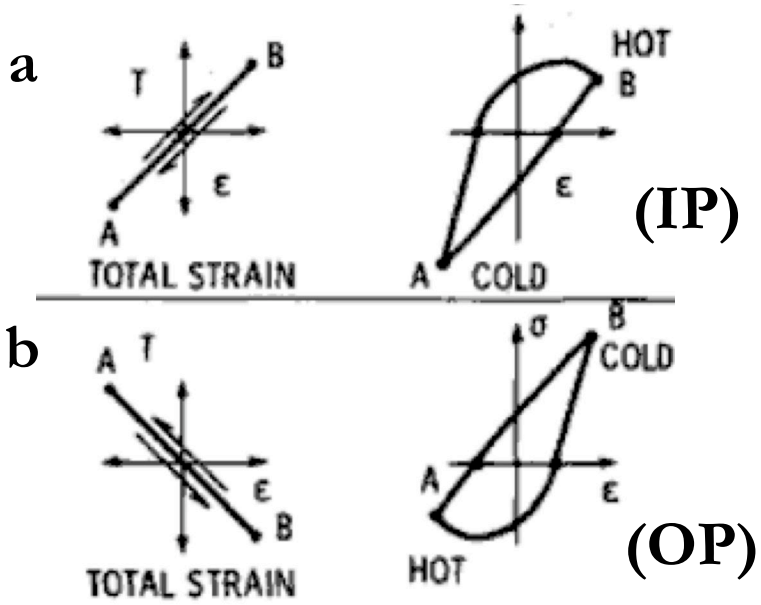


**Fig.1.27 Temperature $T$ and stress $\sigma$ with respect to total strain $\varepsilon$ for different TMF cycle shapes: (a) in-phase TMF(IP), (b) out-of-phase TMF (OP). Reproduced from [52].**

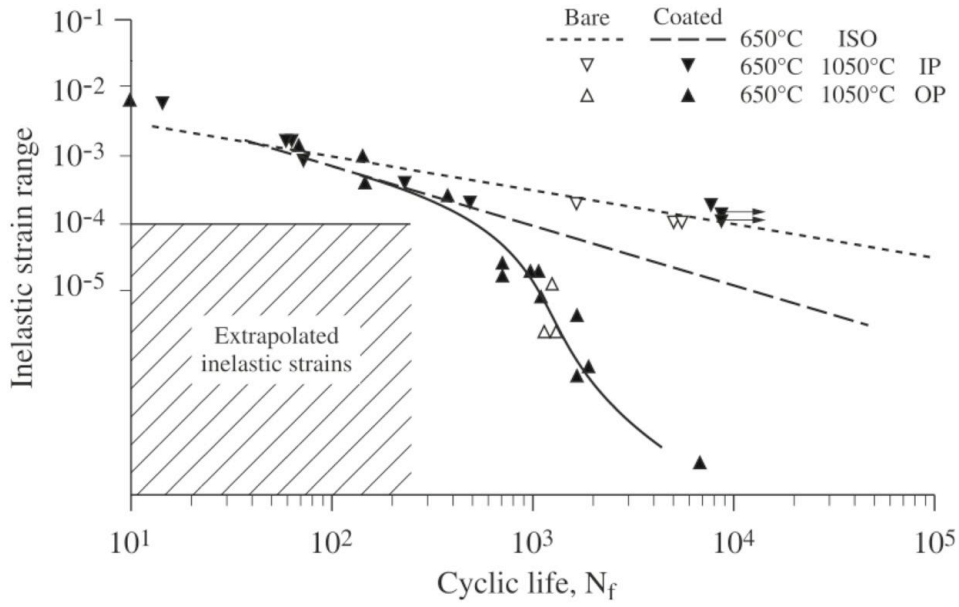


**Fig.1.28 Fatigue life curves for PWA-1480 in both in-phase (IP) and out-of-phase (OP) testing compared to isothermal fatigue (denoted as ISO) at 650ºC. Data are provided for bare and coated specimens [54].**

## 1.4.8 Effect of Oxidation on Fatigue Crack Propagation

In 1989, Neu and Sehitoglu [61] proposed three life controlling factors for TMF in iron base alloys: (i) creep, (ii) fatigue and (iii) oxidation. Although these factors have been mentioned already, additional considerations concerning the effect of oxidation on TMF are discussed here.

When the stress amplitude places the nominal stresses at or beyond the elastic limit, failure occurs typically within $10^5$ cycles, with a majority of the fatigue life being spent in the propagation (rather than initiation) stage [3]. Hence, provided that plastic deformation occurs during TMF, *crack propagation* should be the dominant controlling factor in TMF, rather than crack initiation. Then, the propagation rate might be described with an oxidation term, but only when the crack tip is subjected to an oxidising environment [62]. Due to the cracks created during OP-TMF, the oxidation rate at the crack tip is expected to be higher than the parabolic rate during isothermal oxidation (see Fig.1.29) [61]. Note that these cracks in questions propagate in the direction normal to the surface; thus this should be distinguished from the one which is parallel to the surface (spallation). Typically, the oxide will fracture near the low-temperature end of the OP-TMF cycle when the oxide is more brittle and the stress is tensile [53]. Thus the crack tip temperature during TMF is expected to be much lower than that during isothermal low-cycle fatigue testing. If nickel-based supealloys have much better oxidation resistance than iron base alloys, it seems possible to assume that the effect of oxidation on crack propagation is relatively minor.

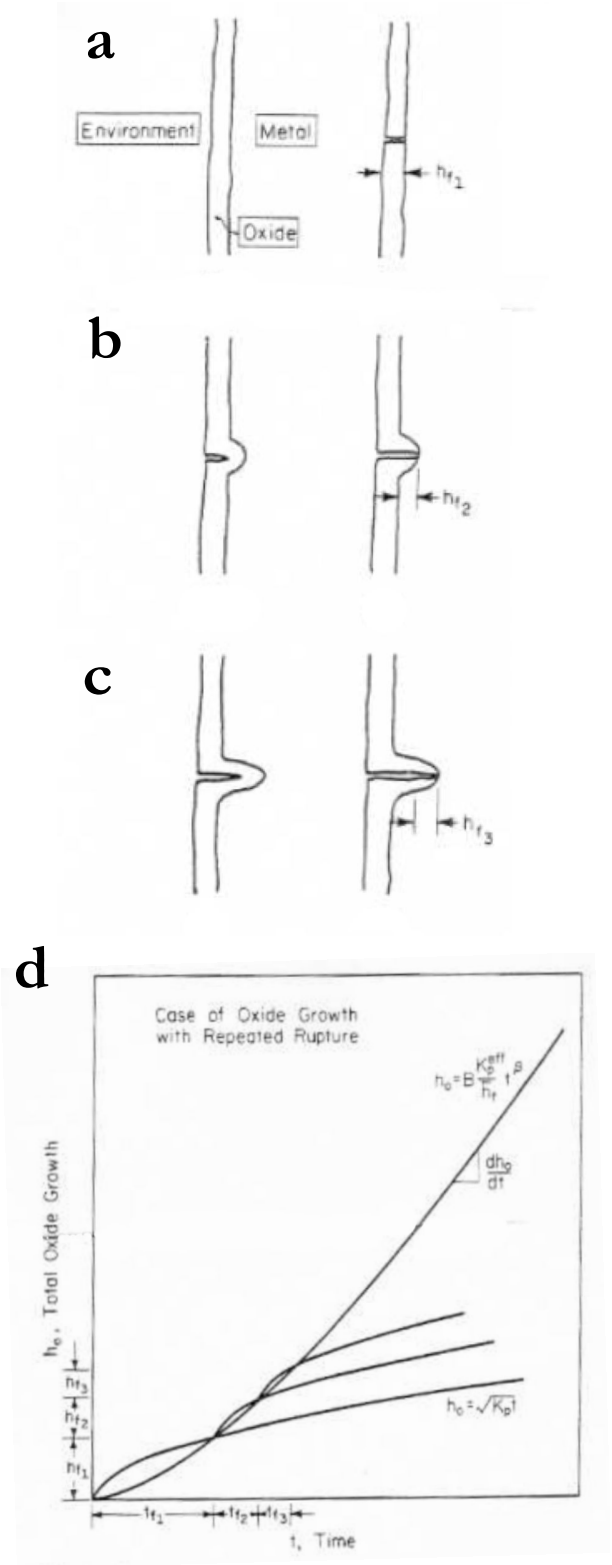


**Fig.1.29 Schematic illustration showing the (a) to (c): nucleation of oxide growth and (d) diagram illustrating oxide growth with repeated rupture. Note in (d) that oxidation rate in OP-TMF is expected to be larger than the parabolic rate. Note that $h_f$ represents the critical oxide thickness to crack initiation at time $t_f$ [61].**

## 1.4.9 Effect of Rafting on Fatigue Crack Propagation

In 1999, Ott & Mughrabi [34, 63] summarised the effect of rafting on the crack propagation rate occurring during high temperature LCF testing. All stress response on CMSX-6 with different γ' morphologies show a similar stress level of about 500 MPa until fatigue crack propagation starts [63] (Fig.1.30). The crack propagation rate was influenced by the γ/γ' morphology, and pre-rafted in compression shows best fatigue performance. Based on fractographic observations on CMSX-4, it was found that the crack propagation occurs in the γ phase or at the γ/γ' interface (Fig.1.31). At temperatures above 800ºC and when the stress is low, the dislocation motion is restricted to the γ phase, because cutting of the γ' phase by dislocations would require the formation of a high energy APB. In such circumstances, a crack tends to avoid cutting the γ' phase. Hence, it is considered that pre-rafted in compression performed as best because rafted γ' acts as an obstacle which delays fatigue crack propagation. No significant oxidation at the crack tip is seen; hence, the effect of oxidation on crack propagation rate [62] is likely to be negligible. Thus, this theory may also work for TMF, but only when γ' shearing is not present. The presence of stacking faults in γ' after OP-TMF is found, indicating that γ' shearing is present. Even in this condition, it was suggested that the deposited dislocations on the γ/γ' interface cannot escape completely from the long and irregular rod-like γ' structure (Fig.1.32) [57]. Thus rafting prohibited the long-range dislocation gliding (slip or twining) by causing local misorientation at γ/γ' interface. In contrast, the deposited dislocations are able to escape easily from the cuboidal γ/γ' interface by climbing. In short, even if γ' shearing is present or not, rod-like rafting is considered beneficial for OP-TMF.

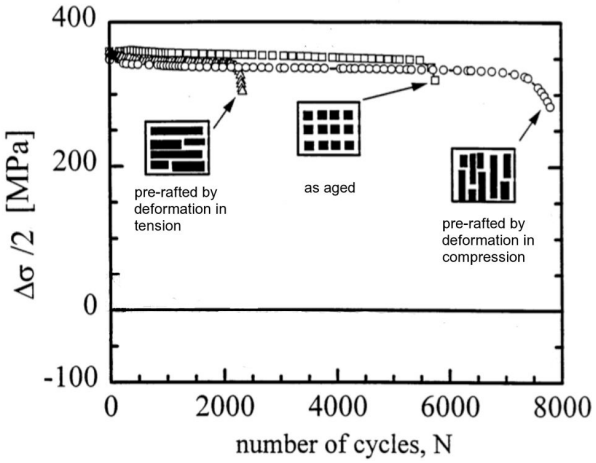


**Fig.1.30 Comparison of cyclic deformation curves (stress amplitude $\Delta\sigma/2$ versus number of cycles $N$) of single crystals of superalloy CMSX-6 with three different initial γ/γ' microstructures (as aged, pre-rafted in tension, pre-rafted in compression)[34, 63].**

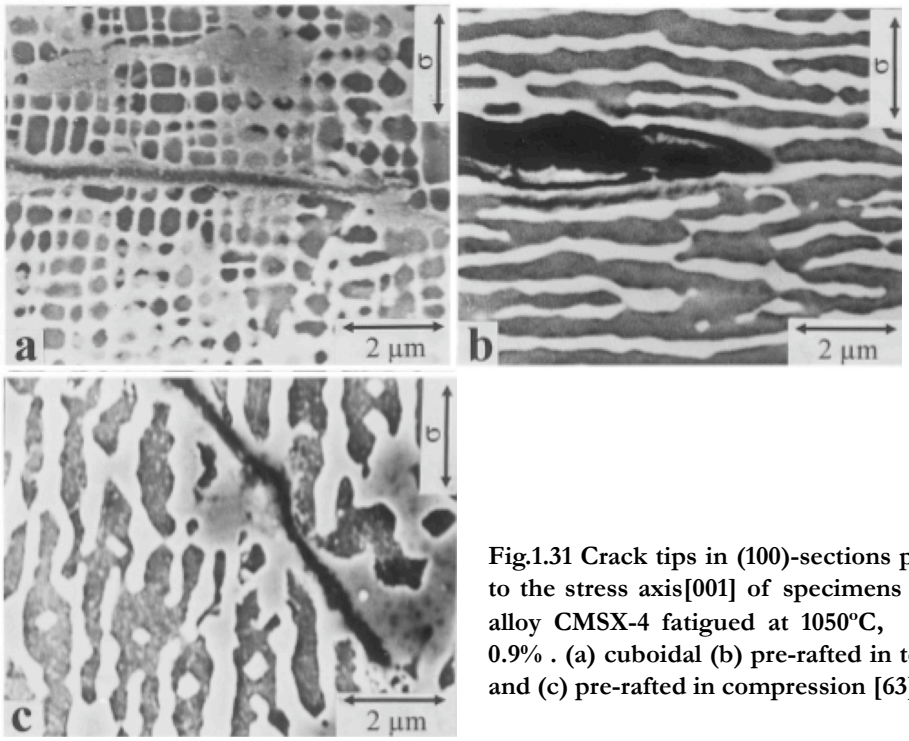


**Fig.1.31 Crack tips in (100)-sections parallel to the stress axis[001] of specimens of the alloy CMSX-4 fatigued at 1050ºC, $\Delta\varepsilon_t$ = 0.9% . (a) cuboidal (b) pre-rafted in tension and (c) pre-rafted in compression [63].**

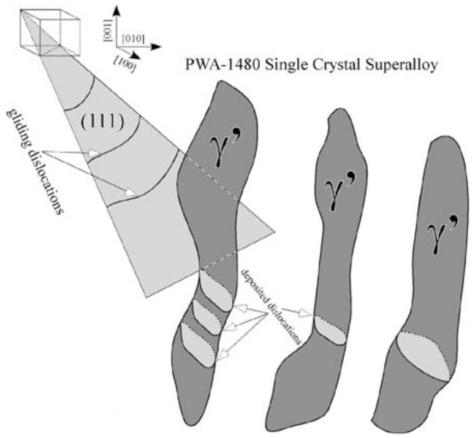


**Fig.1.32 Schematic illustration of movement of gliding dislocations in the γ/γ' structure in the PWA-1480 alloy[57].**

## 1.4.10 Lifshitz-Slyozov-Wagner Theory

It has been seen that the γ' size can influence the high temperature deformation of superalloys. Increasing γ' size may be beneficial at lower temperature (higher CRSS), yet may be detrimental at higher temperature (creep). Importantly, precipitate size can be increased by high temperature exposure; this should be reviewed.

Based upon the Lifshitz-Slyozov-Wagner (LSW) theory [64, 65], the coarsening behaviour of γ' precipitates in nickel-based superalloys can be described by

$$\left(r^3 - r_0^3\right)^{1/3} = kt^{1/3} \tag{1.17}$$

where $k$ is the coarsening rate coefficient, $r_0^3$ is the average radius of γ' phase at time $t = 0$, and $r$ is the average radius of γ' phase. The coarsening rate coefficient $k$ is given by

$$k = \left( \frac{8 D_{\text{eff}} \sigma^{\gamma/\gamma'} N_\alpha V_m}{9RT} \right)^{1/3} \tag{1.18}$$

where $D_{\text{eff}}$ is the effective diffusion coefficient, $\sigma^{\gamma/\gamma'}$ is the γ/γ' interfacial energy per unit area, $N_\alpha$ is the total mole fraction of solute in γ phase, $V_m$ is the molar volume of the γ' phase (≈ 6.8×10-6 $m^3mol^{-1}$[66]), $R$ is the gas constant and $T$ is the absolute temperature. Note that LSW theory is based upon the following main assumptions;

- Particles are spherical, with small volume fraction.
- Constant interface mobility.
- Processes such as nucleation or aggregation that introduce new particles are negligible.

The interfacial energy $\sigma^{\gamma/\gamma'}$ can be calculated as

$$\sigma^{\gamma/\gamma'} = \beta \Delta H_m \tag{1.19}$$

where $\beta$ is an empirically determined constant (≈2.13×10$^{-5}$ in this study), and $\Delta H_m$ the enthalpy of solution of 1 mole of γ' in the γ in equilibrium at the coarsening temperature. In other words, the contribution of entropy part can be neglected. Moreover, the effective diffusion coefficient, $D_{\text{eff}}$, can further be calculated [67] as

$$D_{\text{eff}} = D_0^{\gamma} \exp(-Q_{\text{eff}} / RT) \tag{1.20}$$

where

$$D_0^{\gamma} = \sum_i x_i^{\gamma'} D_i^0 \tag{1.21}$$

$$Q_{\text{eff}} = \sum_i x_i^{\gamma'} Q_i \tag{1.22}$$

where $x_i^{\gamma'}$ is the mole fraction of element $i$ in γ' phase, $D_i^0$ and $Q_i$ are the frequency factor and activation energy for the diffusion of element $i$ in the γ phase, respectively. Interdiffusion coefficients of important elements in the superalloys are summarised in Table 1.2.

**Table 1.2 Interdiffusion coefficients of element *i* in γ phase obtained from [68, 69].**

| | Ni | Co | Cr | Mo | W |
|---|---|---|---|---|---|
| $D_0$ (m$^2$·sec$^{-1}$) | 1.84×10$^{-4}$ | 2.20×10$^{-5}$ | 5.00×10$^{-5}$ | 3.00×10$^{-4}$ | 8.00×10$^{-6}$ |
| $Q$ (kJ·mol$^{-1}$) | 285 | 256 | 260 | 288 | 264 |
| | Al | Ti | Nb | Ta | Re |
| $D_0$ (m$^2$·sec$^{-1}$) | 1.87×10$^{-4}$ | 8.60×10$^{-5}$ | 9.00×10$^{-5}$ | 2.19×10$^{-5}$ | 8.20×10$^{-7}$ |
| $Q$ (kJ·mol$^{-1}$) | 268 | 257.1 | 278.7 | 251 | 255 |

# Chapter 2. Experimental Procedures

## 2.1 Introduction

### 2.1.1 Objectives

The main aim of the work within this thesis is to advance knowledge of and make new insights into the alloy design of nickel-based single crystal superalloys. Research will be firstly focused upon rationalising the oxidation kinetics of nickel-based superalloys and their chemical composition. The primary technique to be used is computer simulations based on both Wagner's theory of parabolic oxidation and Wagner-Haffe theory. Research will also be addressed into rationalising creep and thermomechanical fatigue deformation. These will be combined with the supporting experimental techniques shown in the later parts of this chapter.

### 2.1.2 Alloy Design Concept

Usually, nickel-based superalloys contain more than 8 elements (Ni, Co, Cr, Mo, W, Al, Ta, Hf), and there are thus many possibilities for new candidate alloys. In this study, the target range was selected by appealing to prior experience and then the compositions were further narrowed by various calculations. A candidate, SCA425+ was chosen in the following way. First of all, the chemical composition range applied in this project was selected. Siemens

Industrial Turbomachinery AB in Sweden considered appropriate target ranges, and decided upon [70]

(i) Cr > 12 wt.%.

(ii) Al > 4 wt.%

(iii) Low levels of Ti, Nb, V

(iv) Volume fraction of gamma prime *f* to be moderate

(v) Ta to be the main strengthening element

(vi) Relatively wide heat treatment window

The condition (i) was chosen to ensure very high corrosion resistance, which is a strong requirement for IGTs. The higher amount of aluminum (ii) promotes the formation of alumina, which promotes oxidation resistance. The third condition (iii) avoids the harmful element for oxidation resistance [71], see Fig.2.1.

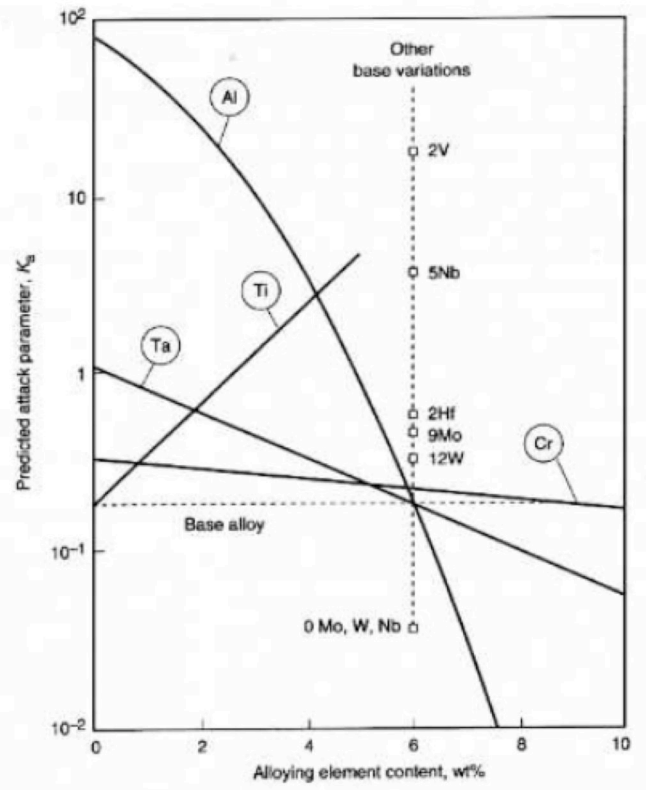


**Fig.2.1 Modelled (individual element) compositional effects on the 1100ºC cyclic oxidation attack parameter for a Ni-8Cr-6Al-6Ta-4Mo-4W-1Nb base alloy[71].**

In the case of (iv), it is well known that 62.5% and 75% of γ' confers the best creep properties at 800°C and 1000°C, respectively [72]. However, in this study, a relatively lower amount of γ' was chosen. This is because a reduction to 50% does not deteriorate the creep properties too much. Furthermore it is known that the higher fraction of the softer matrix phase γ contributes better fatigue properties. Here, low cycle fatigue (LCF) and thermal mechanical fatigue (TMF) are of prime importance. The condition (v) will increase the fraction of the γ' to the target range without significant loss of both creep and oxidation properties. Tantalum is believed to be beneficial for the cyclic oxidation resistance [71]. Increasing Mo, W or Cr decreases *f*; therefore, the addition of γ' phase forming elements i.e. Al, Ti and Ta is necessary. Titanium is known as a harmful element for oxidation, thus tantalum became sensible (note that the condition of Al is in (ii)). The heat treatment window (HTW) in condition (vi) is defined as the temperature differences between solidus and solvus; generally it is better to have a wider HTW range to ease processing.

In order to ensure the idea above was practically feasible, a first trial alloy, called STAL425, was developed as part of a joint project between Siemens (designing), Swedish research institute KIMAB (casting) and Imperial College London (investigations) in 2006. The composition of the KIMAB-cast STAL425 is given in Table 2.1.

**Table 2.1 Nominal compositions (wt.%, Ni-bal.) of superalloys related to this study.**

| | Co | Cr | Mo | W | Al | Ta | Ti | Hf | Other |
|---|---|---|---|---|---|---|---|---|---|
| KIMAB-cast STAL425 | 4.12 | 14.20 | 0.96 | 2.51 | 5.47 | 10.10 | - | 0.41 | C: 470ppm |
| IN738LC | 8.5 | 16.0 | 1.7 | 2.6 | 3.4 | 1.7 | 3.4 | - | 0.01B, 0.1Zr 0.05C |
| SCA425 | 5.00 | 16.00 | 1.00 | 4.00 | 4.00 | 5.00 | 2 | - | - |
| SCA425Hf | 5.00 | 16.00 | 1.00 | 4.00 | 4.00 | 5.00 | 2 | 0.4 | - |
| SCA425+ | 5.00 | 15.50 | 1.00 | 4.00 | 4.55 | 8.00 | - | 0.1 | - |

This composition was chosen in an attempt to satisfy the conditions above. The *f* of KIMAB-cast STAL425 was found to be 62 ± 6 %. Generally speaking, the formation of topologically close packed (TCP) phases in nickel-based single crystal superalloys [42, 43, 73-75] causes considerable mechanical property degradation [76, 77]. But here, no TCP phases were found to precipitate in KIMAB-cast STAL425 after heat treatment. Furthermore, the heat treatment dissolved the eutectic γ' phase completely; thus it is likely that this alloy has a relatively wide HTW. In short, the alloy design concept was confirmed to be very promising.

One candidate alloy, SCA425, was selected to be the base material in this PhD project, on which further design studies could be based. SCA425 was an alloy originally developed by the French Aerospace Lab, ONERA [78]. SCA425 is designed to achieve both IN738LC level of hot corrosion resistance and creep resistance equivalent to IN792. The compositions of IN738LC and SCA425 are listed in Table 2.1. The estimated amount of γ' in SCA425 is 50%. Despite the fact that a beneficial effect of Co on phase stability has been reported by Walston et al. [79], Co was further reduced from IN738LC levels in order to control and limit the primary creep deformation [80]. Secondly the grain boundary strengthening elements such as carbon and boron were removed. This is because there is no need for these elements in a single crystal superalloy. For example, the solidus temperature increases with respect to the removal of these elements, *i.e.* the HTW expands. Thirdly, all of the niobium and some of the titanium in IN738LC were replaced by aluminum and tantalum to expand the HTW furthermore. Finally, tungsten was added to substitute for some of the molybdenum. It is likely that this is because molybdenum forms volatile oxides at high temperature. A further point is that SCA425 cannot produce a continuous alumina layer at 1000°C; therefore, practically it is recommended to add 0.4 wt. % hafnium to SCA425 (termed SCA425Hf) in order improve the oxidation resistance and

moreover to improve the adhesiveness of the aluminide coating applied for oxidation protection. The composition of SCA425Hf is shown in Table 2.1 as well.

Finally, the SCA425+ alloy was developed from the original SCA425 alloy, and it is this alloy which is studied in this thesis. The alloy design targets were

(a) IN738LC level of hot corrosion resistance

(b) IN792 level of creep resistance

(c) CMSX-4 level of oxidation resistance.

Various changes and improvements were made to the new alloy. Firstly, the 2 wt.% of titanium remaining in SCA425 was completely removed. This reduction should improve the oxidation resistance, and should expand the HTW. However, as the result of this reduction, it is estimated that the *f* should decrease to 36%. Then, to compensate for this effect, further amounts of γ' former element, aluminum and tantalum, were added. Tantalum can form very stable oxide at high temperature above 800°C: $Ta_2O_5$ and/or $NiTa_2O_6$. The equivalent amounts were chosen to match *f*; in other words, the *f* of SCA425+ is designed to be equal to that of SCA425 (but the partitioning coefficient of Ta and site occupancy of Ta to Ni/Al site changes). It was found via thermodynamical calculations that 2 wt.% of titanium can be substituted by 0.54wt. % aluminum plus 4.0 wt. % tantalum, or 1.0wt.% aluminum plus 1.62wt.% tantalum. This means that several variation of Ta/Al ratio can be considered as the candidates for this study. A further thermodynamical investigation indicated that a higher Ta/Al ratio narrows the HTW slightly, but a higher level of tantalum will contribute to improve creep, so a compromise needed to be found. The nominal composition of SCA425+ chosen is given in Table 2.1. To sum up, the IN738LC-based SCA425 alloy is chosen as a basis, but this was further modified to SCA425+ to confer better properties particularly in oxidation.

Of course, what is described above is merely conjecture on the basis of modelling. A major aim of the work reported in this thesis is the testing of the predictions.

## 2.1.3 Materials

The prototype nickel-based single crystal superalloy SCA425+[70, 81] was chosen for the present work. This is a candidate for future application in industrial gas turbines partly on account of its Cr content (15.5 wt.%) which is appreciably greater than for most other single crystal alloys – many of which were designed for aero engine applications. Two derivatives of SCA425+ containing 0.25 and 0.5 wt.% Si are also studied here; it has been reported that Si is beneficial with regard to $Al_2O_3$ layer formation [82-85], but one purpose of the experimentation was to check this for the SCA425+ alloy.

Consistent with the result from chapter 3, one further derivative of SCA425+ containing 2 wt.% Re was also investigated. This alloy was used to validate whether our oxidation model works or not, see chapter 6. There is no report indicating that substituting W to Re is beneficial for oxidation; however it is predicted that this would be (chapter 3), hence this alloy was prepared and evaluated. The nominal compositions of the four alloys investigated are given in Table 2.2.

**Table 2.2 Nominal compositions (wt.%, Ni-bal) of superalloys investigated.**

| | Co | Cr | Mo | W | Al | Ta | Hf | Other |
|---|---|---|---|---|---|---|---|---|
| SCA425+ | 5.0 | 15.5 | 1.0 | 4.0 | 4.55 | 8.0 | 0.1 | - |
| SCA425+0.25Si | 5.0 | 15.5 | 1.0 | 4.0 | 4.55 | 8.0 | 0.1 | 0.25Si |
| SCA425+0.5Si | 5.0 | 15.5 | 1.0 | 4.0 | 4.55 | 8.0 | 0.1 | 0.5Si |
| SCA425+Re | 5.0 | 15.5 | 1.0 | 2.0 | 4.55 | 8.0 | 0.1 | 2Re |

# 2.2 Experimental Methodology

## 2.2.1 Mould Preparation & Bridgman Casting

An industrial scale investment casting facility at the University of Birmingham was used to prepare single crystal castings in the form of 15 mm diameter rods of length 150 mm (see Fig.2.2). Typically, three rods were cast in each run with a withdrawal speed of ~200 mm per hour; the anticipated temperature gradient was 75ºC/cm. Ceramic moulds were prepared from alumina, silica and zircon in the usual way (Table 2.3); the final mould thickness was ~6 mm. These were de-waxed in a steam furnace for 5 mins and then sintered at 1000°C for an hour in air, prior to casting. The casting stock was melted by Ross & Catherall in Sheffield, UK to industry-leading standards (see Table 2.4 and 2.5 for its composition). Chemical analysis indicated less than 7.2 ppmw of sulfur in the stock, so that – since the oxidation temperatures used here are 1000ºC or lower and the tests carried out isothermally – any influence of this element on oxidation performance will be negligible [71, 86-90]. Casting was carried out under the vacuum of better than $10^{-4}$ Pa. The single crystal bars were carefully removed from the mould, and then sand blasted. In order to confirm whether the cast bar contained surface defects, the bars were macro etched using HCl + 5~10 vol.% $H_2O_2$ solution. No freckles were observed.

**Table 2.3 – Primary and secondary slurry compositions and stucco with weights for a production size tank.**

| | Primary | Secondary |
|---|---|---|
| Slurry Type | PDS 62 | PDS 295 |
| Binder | Morrisol X30, 66kg | EHT, 52.5kg |
| Wetting agent | Synperonic N, 150ml | Victawet 12, 300ml |
| Anti-foaming agent | Octan-1-ol, 300ml | - |
| Filler | -200 mesh zircon, 300kg | -200 mesh zircon, 200kg |
| Slurry Controls | B5 (flow time for 70ml) should be 28-31 seconds | B4 (flow time for a full cup) should be 55-60 seconds |
| Stucco | AL80 (80 mech alumina) | 28/48 mesh alumina |
| Drying period | 8 hours | 2 hours |
| Coating times | 1 | 5 + sealing |

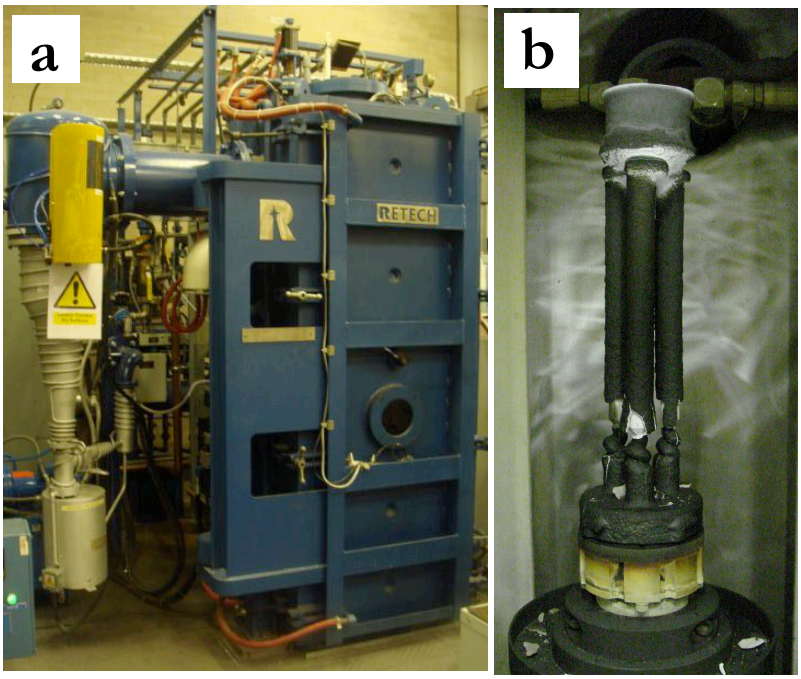


**Fig.2.2 (a) Bridgman casting furnace in University of Birmingham and (b) typical mould used for single crystal bars in this study.**

**Table 2.4 Compositions of major (wt.%) and minor (ppmw) elements in stock.**

| | Co | Cr | Mo | W | Al | Ta | Hf | Si | Re |
|---|---|---|---|---|---|---|---|---|---|
| SCA425+ | 5.03 | 15.55 | 1.00 | 4.00 | 4.52 | 7.95 | 0.10 | 0.05 | <0.05 |
| SCA425+0.25Si | 4.86 | 15.64 | 1.02 | 4.12 | 4.54 | 8.18 | 0.12 | 0.25 | <0.05 |
| SCA425+0.5Si | 5.00 | 15.39 | 1.01 | 4.06 | 4.54 | 7.97 | 0.11 | 0.51 | <0.05 |
| SCA425+Re | 5.01 | 15.57 | 0.99 | 2.01 | 4.55 | 8.04 | 0.11 | 0.05 | 1.99 |

(wt.%)

| | C | S | N | P | O | Zr | Ti | Nb |
|---|---|---|---|---|---|---|---|---|
| SCA425+ | 169 | <2 | 8 | <20 | 7 | <50 | <500 | <500 |
| SCA425+0.25Si | 130 | 7.2 | 3 | <20 | 6 | <50 | <500 | <500 |
| SCA425+0.5Si | 150 | <2 | 4.8 | <20 | 5.9 | <50 | <500 | <500 |
| SCA425+Re | 160 | 4 | 10 | <200 | 8 | <50 | <500 | <500 |

(ppmw)

## 2.2.2 Heat Treatment Studies

To remove microsegregation inherited from casting, an appropriate solutioning procedure was designed. Pieces of the as-cast material were exposed to temperatures between 1250ºC and 1320ºC, for 2 hours. The samples were first put into the furnace heated at 20ºC lower than the target temperature; then after 15 minutes the temperature was increased by +1ºC/ min to the target temperature. The solution treatment chosen are summarised in Table 2.5. Optical micrographs in the as-cast condition and after solution treatment are shown in Fig. 2.3. No incipient melting was observed. These optimal conditions were further supported by differential scanning calorimetry (DSC). Specimens of size 2 × 2 × 2 mm were cut from fully heat-treated bars, and then inserted into a NETZSCH DSC404C machine in pure-$Al_2O_3$ crucibles and analysed between 800ºC to 1400ºC. The heating and cooling rates used were 5ºC/min and 10ºC/min, respectively. The DSC results are summarised in Fig.2.4; these is consistency with the heat treatment studies above.

In order to reprecipitate γ' phase after the solution treatment above, the first ageing treatment was carried out at 1120ºC for 24 hours followed by air-cooling, unless specifically stated otherwise. The second ageing condition was 850°C 20 hours followed by air-cooling, unless specifically stated otherwise.

For simplicity, as a good predictability was found in terms of solidus temperature calculation (Fig.2.4), the solution treatment condition of SCA425+Re was first predicted around 1320ºC, hence solution treated at 1280ºC for 5 hours followed by air-cooling. First ageing condition was 1100ºC 6 hours followed by air-cooling. No incipient melting was found.

**Table 2.5 Solution treatment conditions used for the candidates (AC: Air cooling).**

| | Solution treatment |
|---|---|
| SCA425+ | 1280ºC 1 hour -> 1300ºC 5 hours, AC |
| SCA425+0.25Si | 1260ºC 1 hour -> 1280ºC 5 hours, AC |
| SCA425+0.5Si | 1230ºC 1 hour -> 1250ºC 5 hours, AC |
| SCA425+Re | 1280ºC 5 hours, AC |

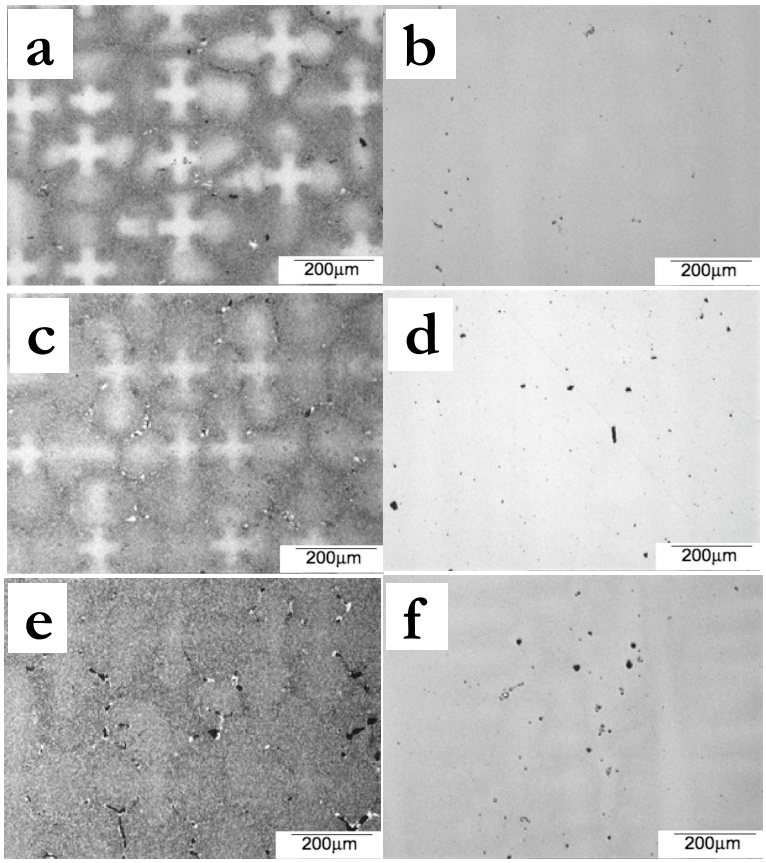


**Fig.2.3 Optical micrographs of (a) SCA425+ as cast, (b) SCA425+ 1300ºC 2 hours AC, (c) SCA425+0.25Si as cast, (d) SCA425+0.25Si 1280ºC 2 hours AC, (e) SCA425+0.5Si as cast and (f) SCA425+0.5Si 1250ºC 2 hours AC. (AC: Air cooling)**

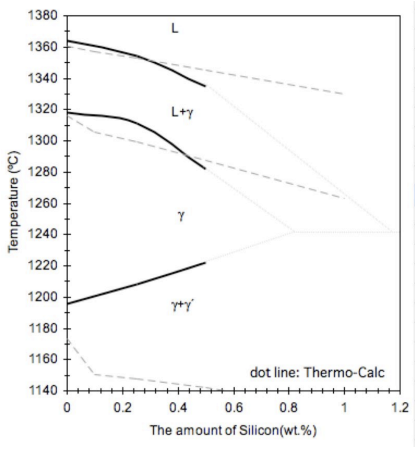


**Fig.2.4 Phase diagram of SCA425+ with respect to Si content. (L: Liquid)**

## 2.2.3 Isothermal Oxidation Test

2 mm thick discs were sliced from the heat-treated castings, polished and cleaned as described in section 2.2.8, and then placed in an alumina boat before being exposed isothermally at 900ºC, 950ºC and 1000ºC for 100 hours, respectively. Isothermal oxidation tests were performed using either a Severn Science Limited tube furnace (max: 1000ºC), Lenton Thermal Designs Limited box furnace (max: 1500ºC) or Elite Thermal Systems Limited box furnaces (max: 1100ºC) without flowing air.

## 2.2.4 Thermogravimetric Mass-Balance Analysis (TGA)

Specimens of size 1 cm × 2 cm × 0.5 mm were prepared; the surfaces were polished to 1200 grit and cleaned thoroughly in an ultrasonic bath with acetone, before analysis in a thermogravimetric mass-balance analysis (TGA) calibrated to better than ± 50 μg. A Ci Electronics MK2-M5 microbalance (Fig.2.5a) together with DISBAL control unit (Fig.2.5b) were used. Temperatures between 900ºC and 1000°C were used, with tests lasting up to 300 hours. Data logging was carried out using Labweigh software.

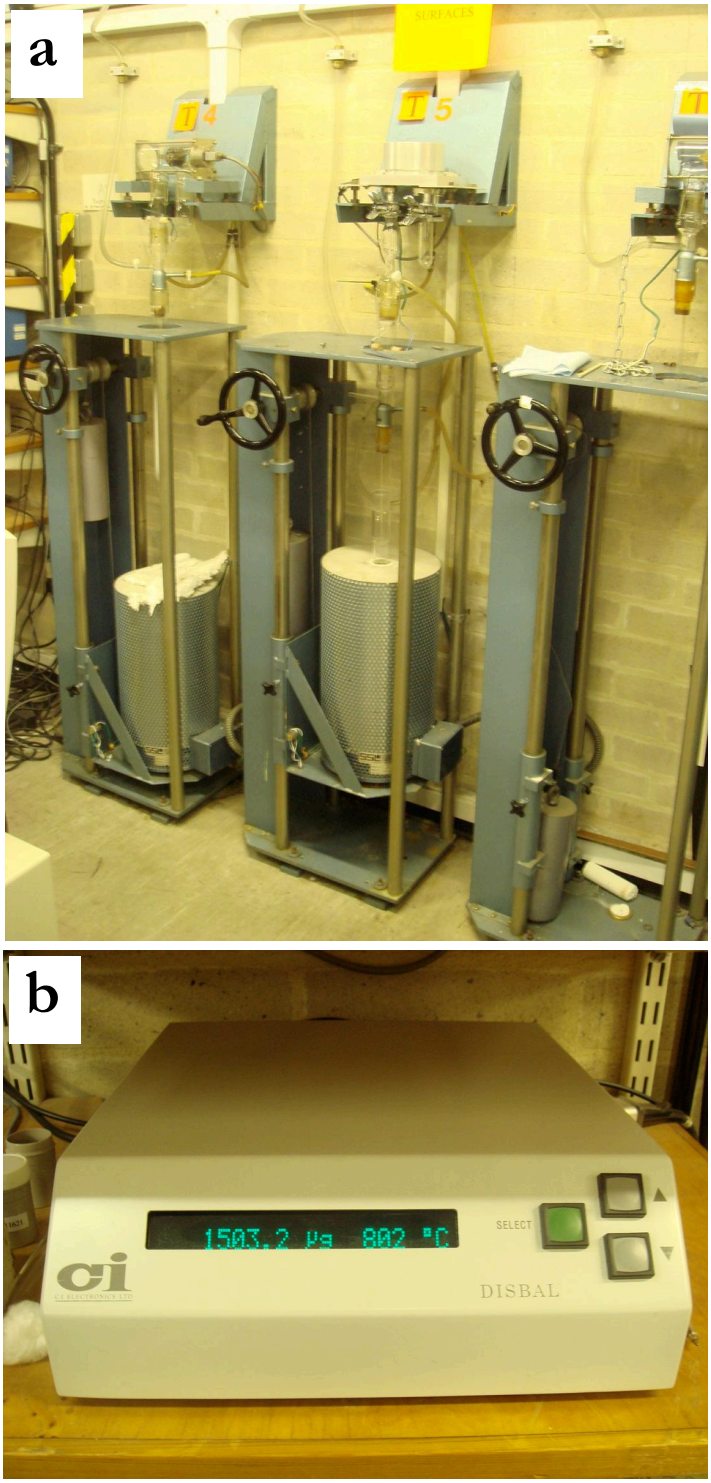


**Fig.2.5 (a) DISBAL control unit and (b) CI Electronics TGA rig at the University of Birmingham.**

## 2.2.5 Creep Testing

Specimens of 24.5 mm gauge length and 5 mm diameter (Fig.2.6) were machined from fully heat-treated single crystal bars. The orientations of specimens were within 10º from the <001> direction. Testing was carried out under constant load conditions at 750ºC/ 520MPa, 750ºC/455MPa, 850ºC/275MPa and 850ºC/235MPa, respectively.

## 2.2.6 Thermomechanical Fatigue Testing

Specimens of 22 mm gauge length and 6 mm diameter were used (Fig.2.7). Out-of-phase (OP) TMF tests were carried out using an MTS 810 servo-hydraulic testing machine (Fig. 2.8) under strain-control, with lower and upper temperatures of 100ºC to 950ºC respectively and with the mechanical strain range, $\Delta\varepsilon_{mech}$, set at values up to 0.9%. All tests were carried out with a strain ratio of $R = \varepsilon_{min}/\varepsilon_{max} = -\infty$. Note that in order to achieve a stabilized mean stress early in the tests, a 20 hour hold time was applied at the maximum temperature of the first cycle; however, 5 minutes hold time was applied in the later cycles (Fig.2.9). This combination of R-ratio and longer hold time in the first cycle was chosen since it is believed to represent better the service conditions experienced in the industrial gas turbine. Specimen was finally hot-mounted for microstructural observations.

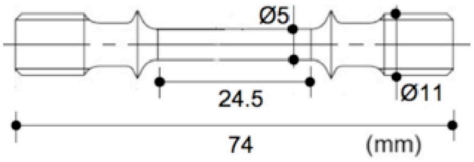


**Fig.2.6 Schematic illustration of specimen geometry for creep testing.**

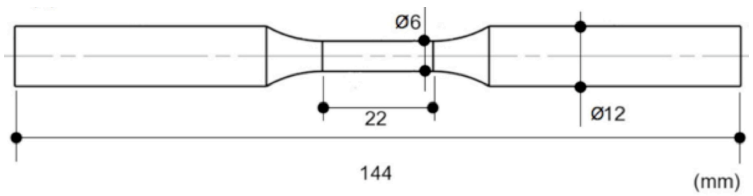


**Fig.2.7 Schematic illustration of specimen geometry for TMF testing.**

**Fig.2.8 MTS 810 servo-hydraulic testing machine in SIEMENS Industrial Turbomachinery AB in Sweden.**

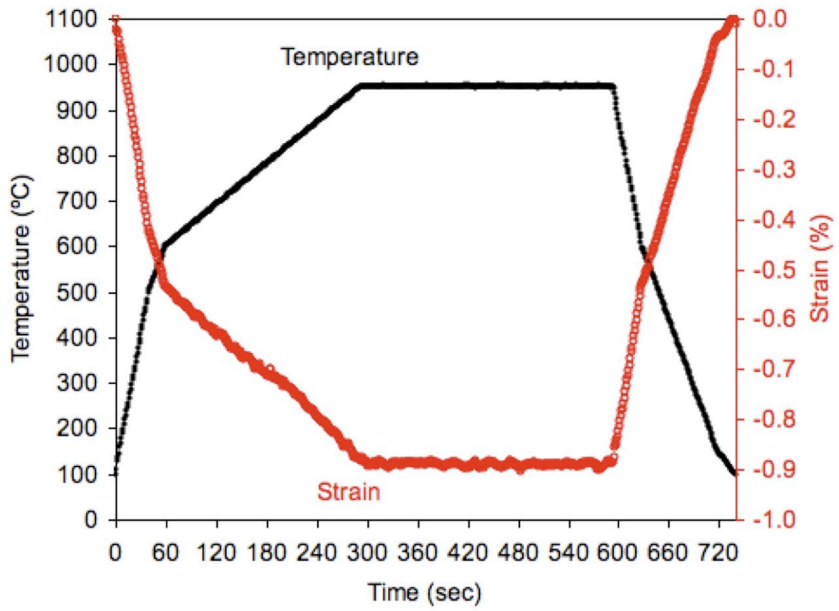


**Fig.2.9 The dependence of strain and temperature on time during TMF cycling, with a compressive hold time of 5 mins. Note that 20 mins hold time was applied in the first cycle.**

## 2.2.7 Hot Mounting Sample Preparation

Specimens were cut using 0.5 mm thickness SiC disc with Struers Acutom 5 (Fig.2.10a). The feed rate was <0.015 mm/sec with disc rotation speed of 3000 rpm. No oscillation was used. Hot mounting was carried out with conductive bakelite by ATM Opal400 (Fig. 2.10b) at less than 200ºC for 15 mins. Specimen was polished in the following way (see Table 2.6). Samples are finally cleaned thoroughly in an ultrasonic bath with ethanol.

**Table 2.6 Polishing condition used for hot-mounted specimens in this study.**

| | Paper/Buff | Suspension | Duration (mins) | Pressure (N) | Rotation speed (rpm) |
|---|---|---|---|---|---|
| 1 | 240grid SiC | water | Until plane | 5 | 250 |
| 2 | UltraPad* | 9μm diamond | 4 | 5 | 125 |
| 3 | TexMet1500* | 3μm diamond | 3 | 5 | 125 |
| 4 | MasterTex* | MasterPrep* (water in last 30 secs) | 2 | 5 | 125 |

* BUEHLER

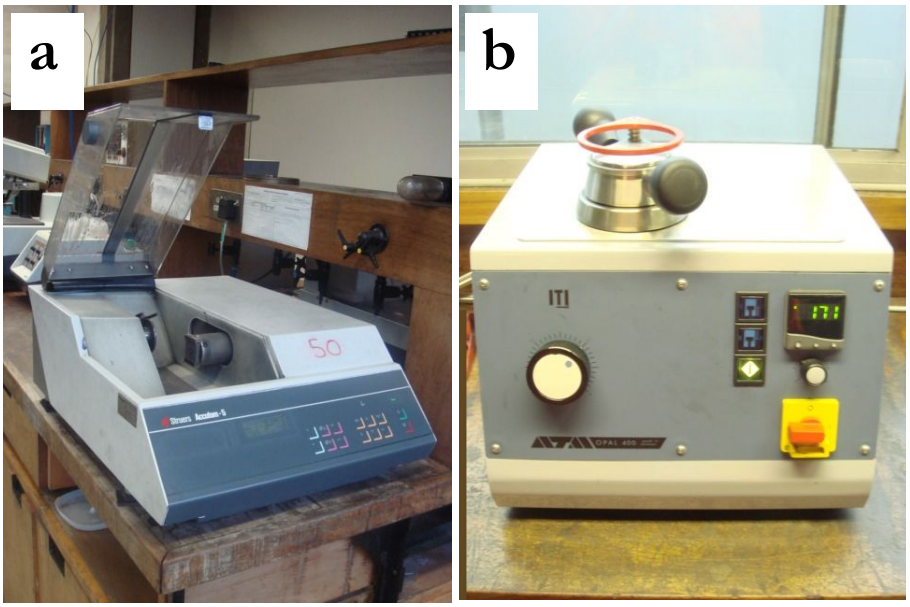


**Fig.2.10(a) fine cutter Struers Acutom 5, (b) automated mounting press ATM opal400 in University of Birmingham**

## 2.2.8 Cold Mounting Sample Preparation

In order to avoid cracks at the oxide/metal interface, oxidised specimens are implanted with epoxy resin (Struers Specifix20), and then ground at least 1 mm with 120 grid SiC paper. The polishing conditions are summarised in Table 2.7. The samples were hand-polished to reduce the polishing pressure. This is because the oxide/substrate has different hardness; thus it is more difficult to remove scratches from both at the same time. Samples were cleaned thoroughly in an ultrasonic bath with ethanol. Finally, specimens were carbon coated for subsequent SEM analysis.

**Table 2.7 Polishing condition used for cold-mounted specimens in this study.**

| | Paper/Buff | Suspension | Duration (mins) | Pressure (N) | Rotation speed (rpm) |
|---|---|---|---|---|---|
| 1 | 120grid SiC | water | Grind 1mm | hand | 250 |
| 2 | 240grid SiC | water | <2 | hand | 125 |
| 3 | 400grid SiC | water | <2 | hand | 125 |
| 4 | 800grid SiC | water | <2 | hand | 125 |
| 5 | 1200grid SiC | water | <1 | hand | 125 |
| 6 | 2500grid SiC | water | <1 | hand | 125 |
| 7 | MasterTex* | MasterPrep* (water in last 30 secs) | 2 | hand | 125 |

* BUEHLER

## 2.2.9 Scanning Electron Microscopy (SEM)

In this study, tungsten filament scanning electron microscopy (SEM), JEOL6060LV, or Field Emission Gun SEM, JEOL7000F, were used. Both were equipped with an Oxford Instruments INCA system for energy dispersive spectroscopy (EDX). For image analysis, in order to obtain clear threshold between matrix and precipitate, etching was performed. The optimal etching solution for SCA425+ was found to be as 200 mL HCl + 50mL $HNO_3$ + 300mL deionised water + 12.5 g CuCl + 12.5 g FeCl. Micrographs were then taken using an image processing software program, Scion image for Windows XP (developed at the U.S. National Institutes of Health), which is freely available from http:// www.scioncorp.com/frames/fr_download_now.htm, or on floppy disk from the National Technical Information Service, Springfield, Virginia, part number PB95-500195GEI.

## 2.2.10 Transmission Electron Microscopy (TEM)

Transmission electron microscopy (TEM) microanalysis was carried out as follows. For oxide/metal interface observation, thin foils were prepared on an FEI Quanta 3D-FEG FIB/SEM to a thickness of ~150 nm; they were cleaned with an 5 kV Ga ion beam at 48 pA. The samples were consequently analyzed on an FEI Tecnai F20 microscope using an Oxford Instrument X-max SDD detector of 80 $mm^2$. In the case of substrate observation, discs of diameter 3 mm were ground mechanically to ~150 μm thickness. A JEOL 200CX microscope at the University of Cambridge was used for this. They were then polished electrochemically by the twin jet method, using an $HClO_4$ + 80 vol.% ethanol solution at 0ºC, using 10-30 V direct current.

## 2.2.11 X-ray and Neutron Diffraction Analysis (XRD & ND)

A Philips X'Pert X-ray diffractometer (Fig.2.11a) with Cu Kα source at 40kV and 40mA, at a scan rate of 2.4° $min^{-1}$ over the 2θ range 0-100°, was used. Note that superlattice peak such as (100) cannot be found in X-ray analysis, but can be found by the neutron analysis (ND)[91]. In this way, the volume fraction of the γ' phase (along with the lattice parameters of the γ and γ' phases and the associated lattice misfit) was evaluated at temperatures of 800, 900 and 1000 °C using the Engin-X neutron diffractometer (ND) at the ISIS facility, Rutherford Appleton Laboratory, Oxfordshire, UK (see Fig.2.11b). Fully solutioned SCA425+ was used. This enabled the (100) superlattice peak from the γ' phase and (200) peaks from both γ and γ' phases to be obtained; the (100) superlattice peak was then fitted by a normal distribution, thus allowing the fitting of the composite peak from (200) by a two-peak gauss function since the position of the (200) superlattice contribution could be deduced. This procedure allowed the volume fraction of the γ' phase to be determined from the ratio $S_{(100)}/S_{(200)}$ of the integrated intensities of the two reflections.

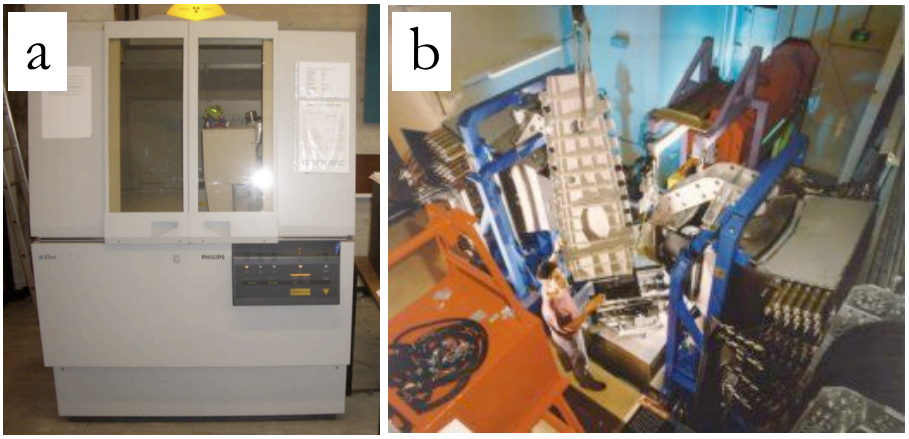


**Fig.2.11 (a) Philips X'Pert X-ray diffractometer at the University of Birmingham and (b) Engin-X neutron diffractometer at the ISIS facility, Oxfordshire, UK.**

# Chapter 3.
# On the Oxidation of Nickel-Based Single Crystal Superalloys for Industrial Gas Turbine Applications

## 3.1 Introduction

Oxidation of the nickel-based superalloys – particularly when used for hot section components such as turbine blades and guide vanes – is a possibility which must be anticipated prior to placing them in their operating environment. This is because the conditions experienced during service are very aggressive, with the temperature of the gas stream approaching 1750ºC for a typical gas turbine, for example; thus despite the use of sophisticated cooling arrangements and thermal barrier coatings [92], a metal temperature approaching 1000ºC or greater is typical for many applications. In fact, there are some combinations of engine design and mission characteristics for which oxidation is the predominant mode of damage, far exceeding the likelihood of excessive lengthening of the blade by creep [93]; oxidation can also be the pre-cursor to low-cycle fatigue damage [62, 94]. In these circumstances, failure in an engineering sense is by excessive oxidation since it necessitates the removal of the blade from service before the design life is reached.

The design of accurate models to allow the oxidation resistance of the nickel-based single crystal superalloys to be estimated as a function of their chemical composition is therefore a significant challenge, which unfortunately has yet to be achieved. A complicating factor is the chemical complexity of these alloys; it is not unusual for ten or more elements to be present, including quantities of Cr, Al, Ti, Ta, W – and potentially platinum group metals such as Re, Ru – so that many different products of the oxidation reaction are possible. These include $Cr_2O_3$, $Al_2O_3$, $TiO_2$, $Ta_2O_5$ and $WO_3$ as well as spinel phases such as $NiCr_2O_4$, $NiAl_2O_4$, $NiTa_2O_6$ and $NiWO_4$ amongst others [8, 95]. In practice, it usually found that alloys which form an alumina scale ($Al_2O_3$) exhibit the greatest resistance to oxidation, despite the thermodynamic driving force for the oxidation of aluminium being the amongst the largest of all the alloying elements added. Clearly, one is then relying upon kinetic effects to provide the oxidation resistance required; growth of $Al_2O_3$ is slow and it adheres to the substrate without spalling excessively. For this reason, many of the most widely employed superalloys – particularly those used for single crystal applications – are $Al_2O_3$ formers. Alloy designers have found from empirical studies that a concentration of about 5~6 wt.% of Al is often sufficient to maintain $Al_2O_3$ scales and thus to maintain adequate oxidation resistance [3, 96, 97]. However, the compositions of the nickel-based single crystal superalloys vary widely, and it is found that some compositions oxidise more readily than others, despite their being $Al_2O_3$ formers. Models which account for these effects would be tremendously useful; construction of them represents an important step towards quantifying the trade-off between oxidation resistance and other properties of interest, e.g. creep resistance.

In this chapter, the factors influencing the formation of an $Al_2O_3$ layer on the nickel-based superalloys are considered. The performance of three nickel-based single crystal superalloys are considered; these are prototypes which might find future application in the

IGTs used for electricity generation. Whilst these alloys are shown to be $Al_2O_3$ formers, they are marginally so and this has allowed the factors influencing $Al_2O_3$ formation to be studied in detail. In the later part of this work, a procedure for estimating whether any given superalloy will form a compact $Al_2O_3$ layer is described. This captures many of the critical physical phenomena which determine whether any given superalloy forms an $Al_2O_3$ scale or not. Its predictions are compared critically to experimental data reported here but also that available in the literature.

## 3.2 Background Theory

Since the concern in this work is the oxidation resistance of the nickel-based superalloys, the fundamentals governing this are briefly considered; these will be built upon in the later parts of this chapter.

The oxidation of an alloying element M from the superalloy can be represented by

$$\left(\frac{2x}{y}\right)\mathrm{M} + \mathrm{O_2} \rightarrow \left(\frac{2}{y}\right)\mathrm{M_xO_y} \tag{3.1}$$

so that a parabolic oxidation constant $k_t$ can be introduced consistent with Wagner's theory [11] as eq.1.11 (details in section 1.3.2). $\Delta G_f$ term in eq.1.11 is the Gibbs free energy of formation of the $\mathrm{M_xO_y}$ oxide and this can be expanded consistent with the Van't Hoff isotherm [8, 9] according to eq.1.1 (section 1.3.1). Eq.1.1 can also be used to calculate the partial pressure of oxygen by placing $\Delta G_f$ equal to zero [98]; for example, data for $\Delta G_0$ are available from several databases and $a_{\mathrm{M}}$ can be calculated using the Thermo-Calc software [9], so that the driving force of oxidation, i.e. $\Delta G_f$, can be estimated. Notice that eq.1.11 implies

$$k_t \propto \Delta G_f \tag{3.2}$$

Also, by combining eq.1.1 and eq.3.2 one has

$$k_t \propto \Delta G_f = \Delta G_0 + RT \ln\left(\frac{a_{\mathrm{MxOy}}^{2/y}}{a_{\mathrm{M}}^{2x/y} \cdot P_{\mathrm{O_2}}}\right) \tag{3.3}$$

Thus the oxidation rate is a function of $\Delta G_f$ which can be calculated from $a_{\mathrm{M}}$; this is dependent upon the chemistry of the superalloy.

The ability of a nickel-based superalloy to form an $Al_2O_3$ scale depends not just on thermodynamic driving forces but also on kinetic factors [99]; for example, the presence of impurities in the $Al_2O_3$ inherited from the superalloy has a profound influence on the oxidation kinetics [12]. For these applications $Al_2O_3$ is in practice an n-type oxide rather than p-type one [22], so that it is an electron conductor with $t_{el} \approx 1$; thus eq.1.11 can be rewritten as

$$k_t = -\frac{\sigma_t t_{ion}}{z_c^2 z_a^2 e^2} \Delta G_f \tag{3.4}$$

Moreover, different contributions to $t_{ion}$ from anions and cations can be acknowledged so that

$$k_t = -\frac{\sigma_t \left(t_a + t_c\right)}{z_c^2 z_a^2 e^2} \Delta G_f \tag{3.5}$$

where $t_a$ represents the transport number of the anions and $t_c$ is the equivalent quantity for the cations. In the case of an n-type conductor, one has $t_a >> t_c$ so that

$$k_t = -\frac{\sigma_t t_a}{z_c^2 z_a^2 e^2} \Delta G_f = -\frac{\sigma_a}{z_c^2 z_a^2 e^2} \Delta G_f \tag{3.6}$$

Here, the anion is the oxygen ion and with the use of Nernst-Einstein relation one can write

$$k_t = -\frac{\frac{c_o z_a^2 e^2}{kT} D_o}{z_c^2 z_a^2 e^2} \Delta G_f = -\frac{c_o D_o}{z_c^2 kT} \Delta G_f \tag{3.7}$$

where $c_o$ represents the concentration of oxygen in the oxide, $D_o$ represents the diffusion

doubly charged oxygen vacancy is the dominant defect in $Al_2O_3$ at high temperatures, one has

$$k_t = -\frac{c_{\mathrm{O}}\left(\frac{\mathrm{V}_{\ddot{\mathrm{O}}}}{c_{\mathrm{O}}}\right)D_{\mathrm{V}_{\ddot{\mathrm{O}}}}}{z_c^2 kT}\Delta G_f = \left(-\frac{D_{\mathrm{V}_{\ddot{\mathrm{O}}}}}{z_c^2 kT}\right)\mathrm{V}_{\ddot{\mathrm{O}}}\Delta G_f \tag{3.8}$$

where $D_{\mathrm{V}_{\ddot{\mathrm{O}}}}$ represents the diffusion coefficient of a doubly charged oxygen vacancy, and $\mathrm{V}_{\ddot{\mathrm{O}}}$ represents its concentration. At constant temperature, one has from eq.3.8

$$k_t \propto \mathrm{V}_{\ddot{\mathrm{O}}}\Delta G_f \tag{3.9}$$

so that the concentration of the dominant defect is one of the most important factors influencing the oxidation rate. Note that the Eq.3.9 above is the model equation to emphasize the importance of the concentration of the dominant defect. In practice [20] however, the concentration of the dominant defect is strongly influenced by the presence of impurities inherited from base metals cations such as $Ni^{2+}$. For example, suppose that the predominant impurity defect in $Al_2O_3$ is Ni; the defect reaction can then be written

$$se' + s\mathrm{NiO} + \frac{s}{4}\mathrm{O}_2 \leftrightarrow s\mathrm{Ni}_{\mathrm{Al}'} + \frac{3s}{2}\mathrm{O}_{\mathrm{O}} \tag{3.10}$$

so that *s* mol of electrons are reduced; in order to maintain charge neutrality, one or other of the following reactions must occur:

(a) when the doubly charged oxygen vacancy is the dominant defect, then

$$s\mathrm{NiO} + \frac{s}{4}\mathrm{O_2} \leftrightarrow s\mathrm{Ni_{Al'}} + \frac{3s}{2}\mathrm{O_O} + \frac{s}{2}\mathrm{V_{\ddot{O}}} \tag{3.11}$$

(b) or alternatively, when the singly charged oxygen vacancy is the dominant defect, then

$$s\mathrm{NiO} + \frac{s}{4}\mathrm{O_2} \leftrightarrow s\mathrm{Ni_{Al'}} + \frac{3s}{2}\mathrm{O_O} + s\mathrm{V_{\dot{O}}} \tag{3.12}$$

Further equations for the situations when the dominant defect is either a singly or doubly charged interstitial metal ion should also be acknowledged, but for the simplicity, these are ignored here. In the case of eq.3.11, one can see that $s$ mol of Ni are associated with $s/2$ mol of doubly charged oxygen vacancies, and in the case of eq.3.12, $s$ mol of Ni are associated with $s$ mol of singly charged oxygen vacancies. Thus, in general, one can summarise the situation as

$$\Delta e' \propto \mathrm{V_{\ddot{O}}} \text{ or } \mathrm{V_{\dot{O}}} \tag{3.13}$$

where $\Delta e'$ represents the net electron concentration change in the parent oxide. These ideas are elaborated upon later in this work.

# 3.3 Results

## 3.3.1 Isothermal Oxidation Testing

Fig.3.1 shows the weight changes recorded during the TGA analysis for alloys with and without Si at temperatures between 900ºC and 1000ºC. Note that alloys received the standard heat treated as stated in section 2.2.2. No significant spallation of oxide was observed. A first notable point is that – when Si is absent – the weight gain accumulated at 900ºC after 100 hours (Fig.3.1c) is significantly larger than that at 1000ºC (Fig.3.1a). When Si doping is introduced, the effect is negligible at 1000ºC (Fig.3.1a) but a beneficial effect is found at lower temperatures. Whilst the oxidation was not found to conform precisely to parabolic kinetics, it was possible to determine instantaneous values of the parabolic thickening constant $k_p$ from the experimental data, see Fig. 3.2. Our calculations indicate that the values of $k_p$ estimated for SCA425+ at 1000ºC at short times are higher than reported in the literature [100] for the growth of $Al_2O_3$ (in fact more consistent with the data for the formation of $Cr_2O_3$) but at later times the kinetics are consistent with it, see Fig. 3.2. Thus the low weight gain observed at 1000ºC in Fig.3.1a is due to the formation of a compact $Al_2O_3$ layer formation, see Fig.3.3a. At 900ºC, the values obtained were in the range reported for $Cr_2O_3$ [100]; the significant weight gain at this temperature is consistent with the lack of perfection of the $Al_2O_3$ layer, and internal oxidation.

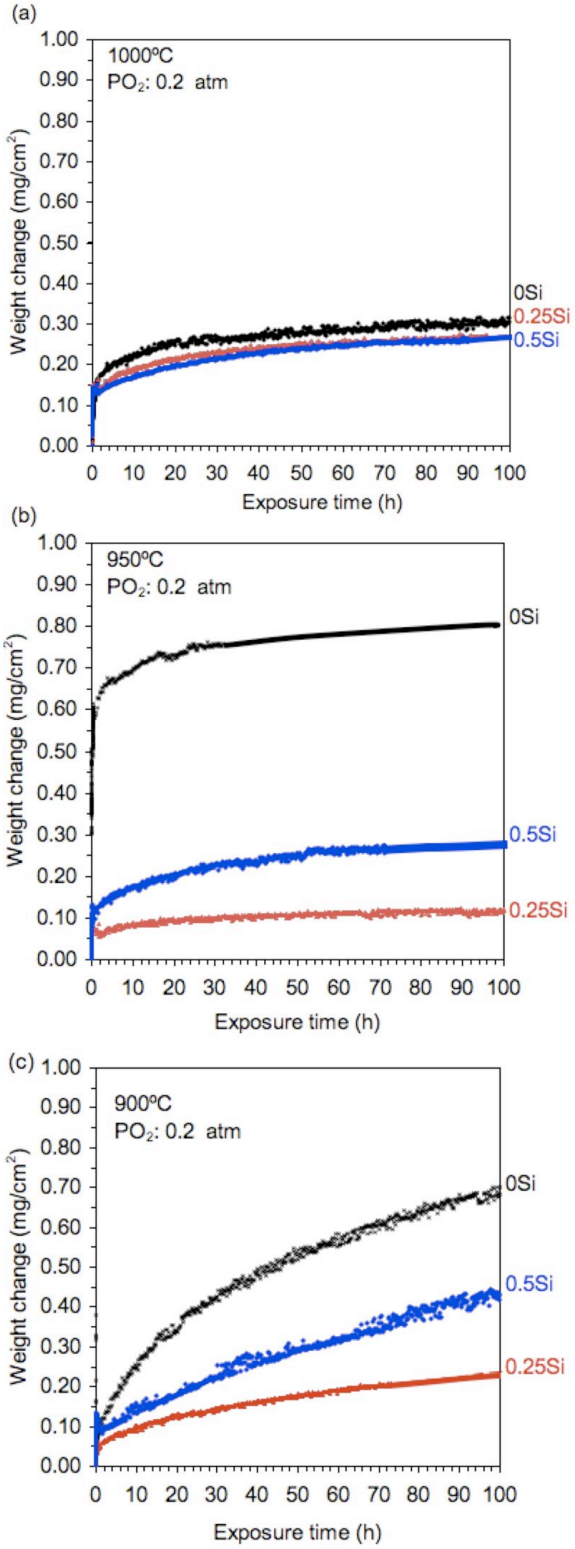


**Fig. 3.1 The weight changes observed in SCA425+ with and without Si during exposure at temperatures of (a) 1000ºC (b) 950ºC and (c) 900ºC.**

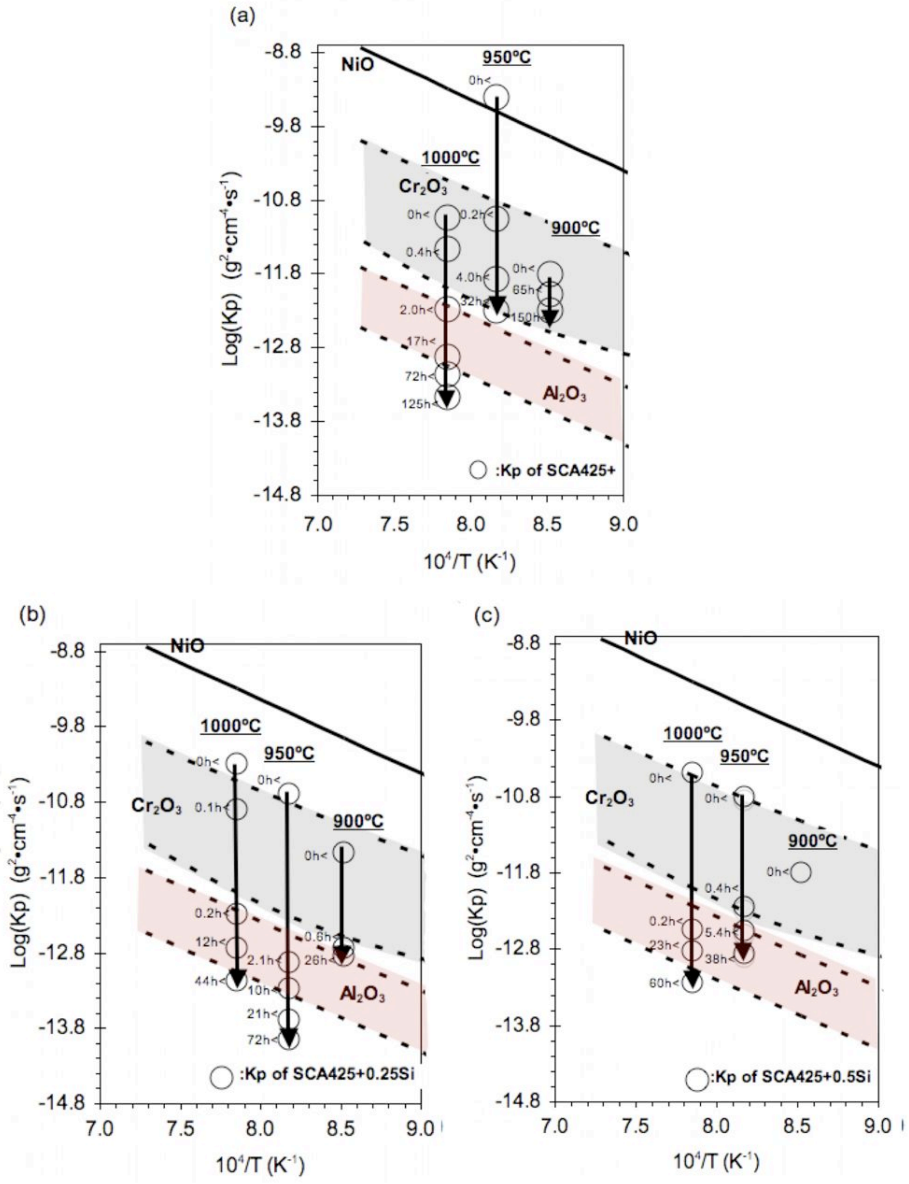


**Fig.3.2. Comparison of the parabolic oxidation constants $k_p$ of SCA425+ between 900ºC and 1000ºC, with the $k_p$ of pure oxides from the literature [100]: (a) SCA425+, (b) SCA425+0.25Si and (c) SCA425+0.5Si.**

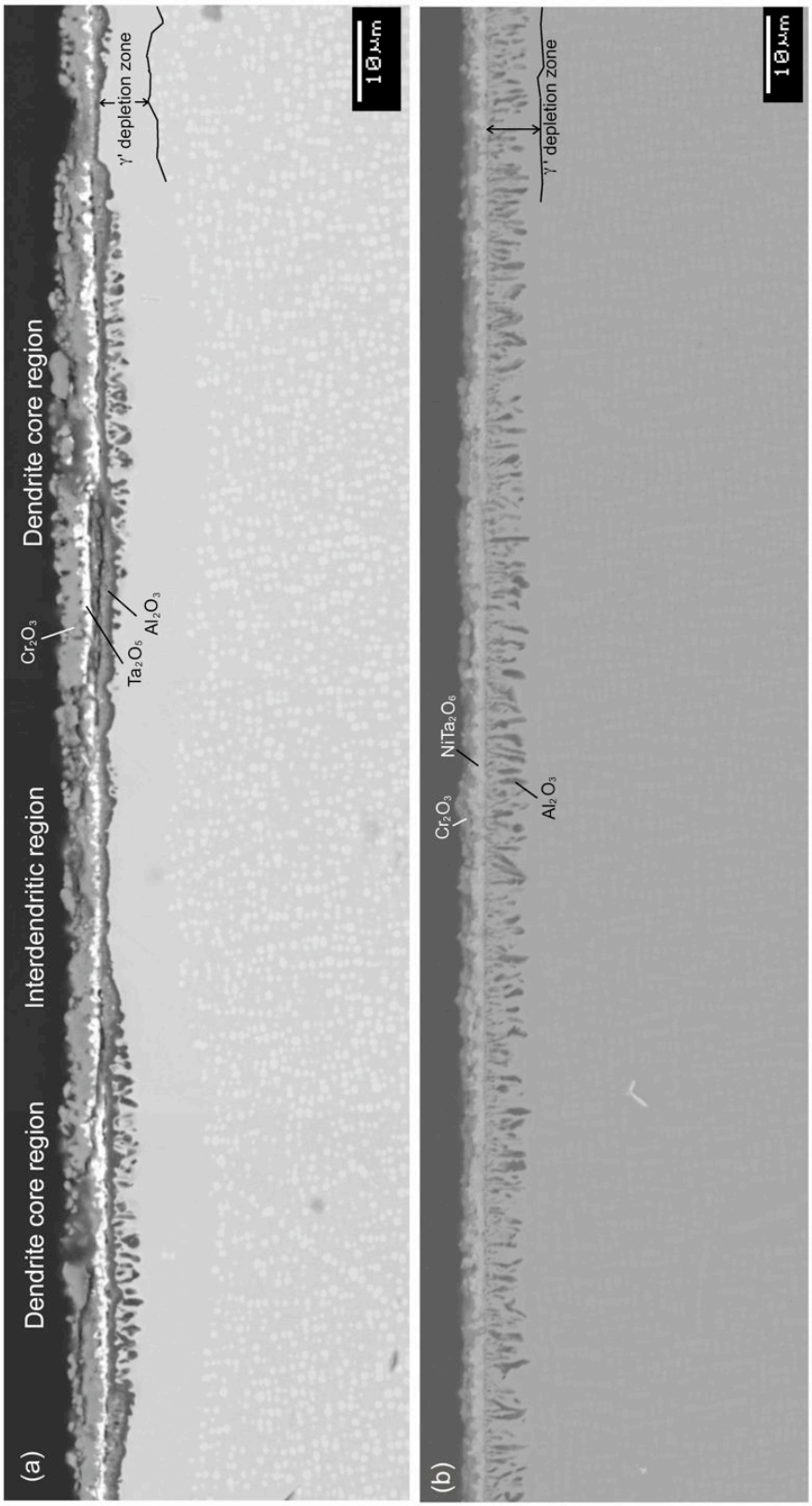


**Fig.3.3 Micrographs of SCA425+ after exposure at (a) 1000ºC 100 hours, and (b) 900ºC 100 hours. Note in (a) that the $Al_2O_3$ morphology is continuous in the interdendritic region by discontinuous in the dendritic regions.**

In Fig.3.4, SEM micrographs of the oxidized superalloys are shown after the exposure at temperatures of 900ºC, 950ºC and 1000ºC for 100 hours. The EDX analysis revealed that the darkest oxide layer in Fig.3.4 consisted mainly of aluminium and oxygen, consistent with $\alpha$-$Al_2O_3$; the presence of this phase was confirmed by XRD, see Fig.3.5. This finding was further confirmed by the TEM analysis, see Fig.3.6 and Fig.3.7. The chemical composition of $Al_2O_3$ was 39.6Al - 59.7O - 0.4W - 0.3Mo (in at.%); thus it is confirmed that $Al_2O_3$ can involve impurities at levels of ~0.5 at.% [101, 102]. One can see from Fig. 3.4 that there is a tendency for $\alpha$-$Al_2O_3$ to form a continuous layer only at higher Si contents and when the exposure temperature is higher; at lower temperatures and in the absence of Si, internal oxidation is prevalent. Additionally, the presence of $Ta_2O_5$/ $NiTa_2O_6$ and $Cr_2O_3$ were confirmed by both EDX and XRD. For example, in the images in Fig.3.4 $Ta_2O_5$ is the brightest oxide and $Cr_2O_3$ is the second brightest oxide for SCA425+ exposed to 1000ºC; $NiTa_2O_6$ is the brightest oxide and $Cr_2O_3$ is the second brightest oxide for the same alloy at 900ºC. Thus, as one moves outward across the scale towards the outer surface, one moves from $Al_2O_3$ -> $Ta_2O_5$/$NiTa_2O_6$ -> $Cr_2O_3$. The morphologies of $Al_2O_3$ observed after 100 hours exposure are summarised in Table 3.1.

**Table 3.1 The summary of the morphologies of $Al_2O_3$ observed after 100 hours exposure. The black circle, circle with cross and white circle indicates the continuous $Al_2O_3$ layer, partially continuous $Al_2O_3$ and discontinuous $Al_2O_3$ layer, respectively.**

| | SCA425+ | SCA425+ 0.25Si | SCA425+ 0.5Si |
|---|---|---|---|
| 1000ºC | ⊗ | ⊗ | ● |
| 950ºC | ⊗ | ⊗ | ● |
| 900ºC | ○ | ○ | ○ |

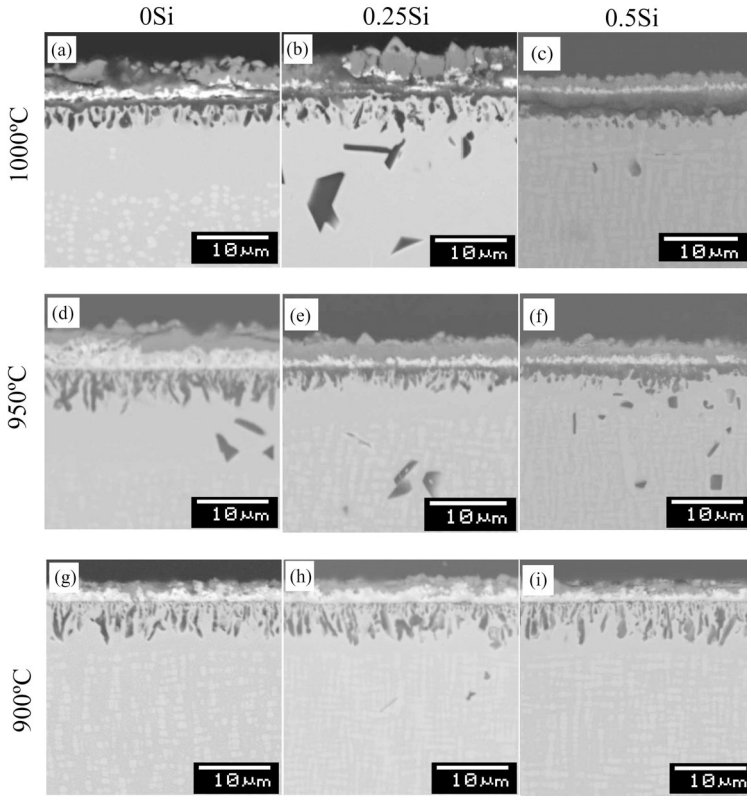


**Fig. 3.4 Micrographs of oxidized superalloys after 100 hours exposure in one atmosphere air: (a) SCA425+ exposed at 1000ºC, (b) SCA425+0.25Si exposed at 1000ºC, (c) SCA425+0.5Si exposed at 1000ºC, (d) SCA425+ exposed at 950ºC, (e) SCA425+0.25Si exposed at 950ºC, (f) SCA425+0.5Si exposed at 950ºC, (g) SCA425+ exposed at 900ºC, (h) SCA425+0.25Si exposed at 900ºC, (i) SCA425+0.5Si exposed at 900ºC. Note that all micrographs were obtained from the dendrite core region.**

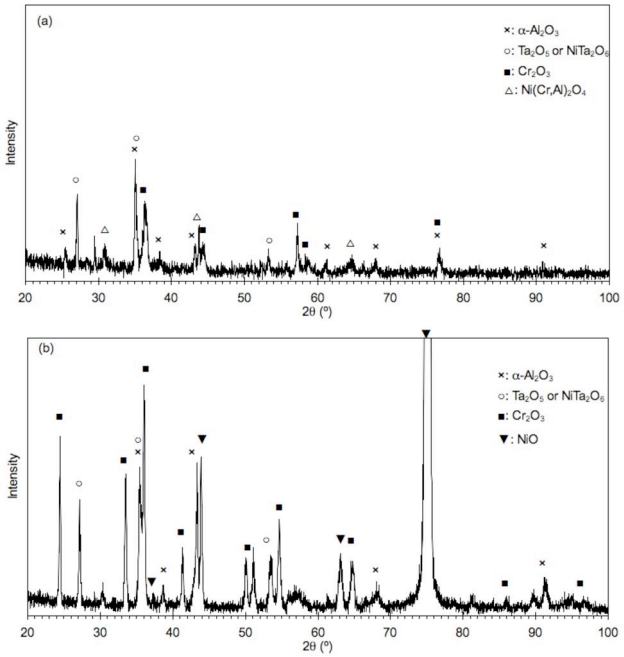


**Fig 3.5 X-ray diffraction patterns of oxide formed on SCA425+ after exposure at (a) 1000ºC for 300 hours and (b) 900ºC for 300 hours.**

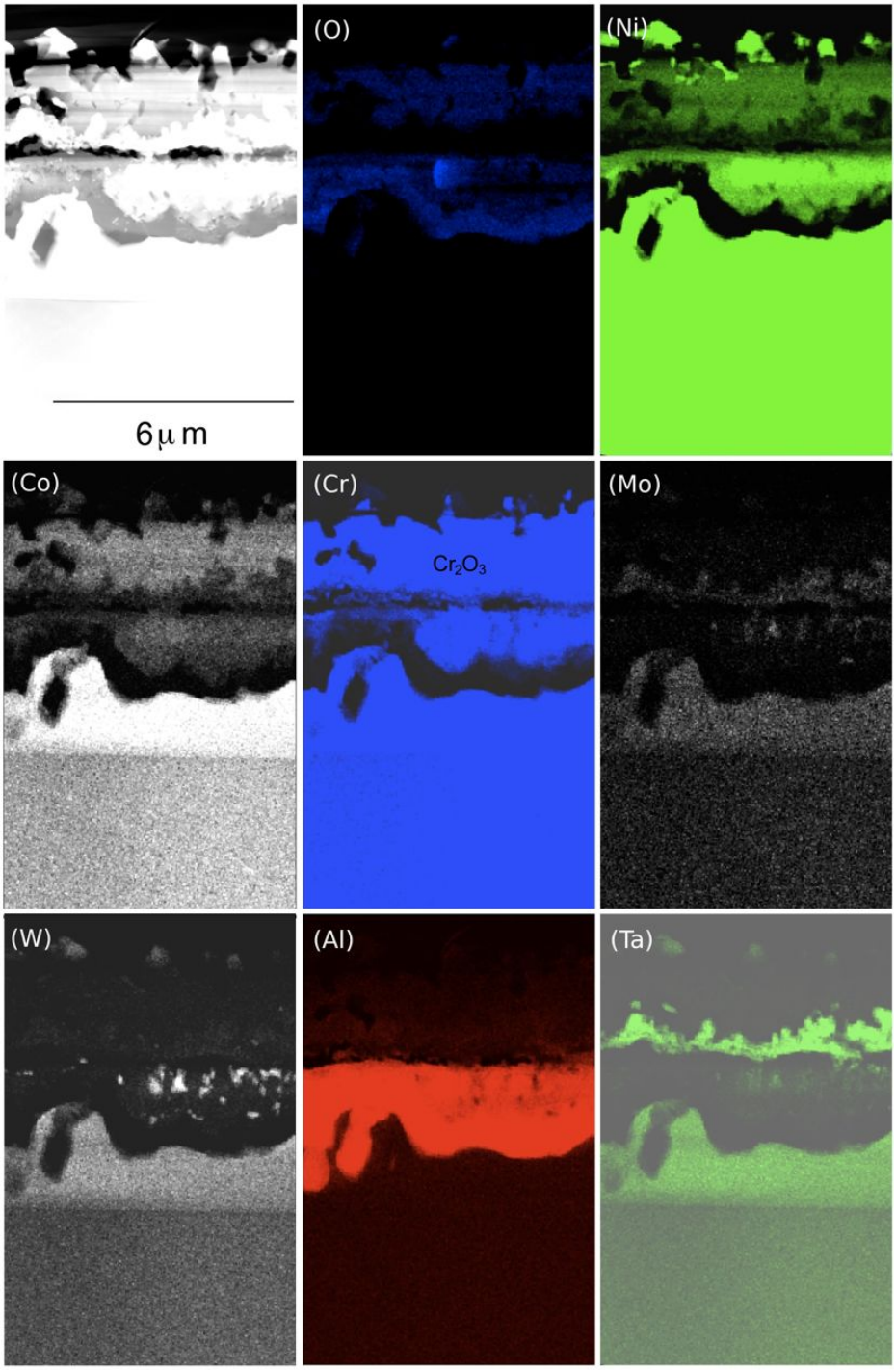


**Fig 3.6 Results from STEM-EDX mapping for SCA425+ exposed at 1000ºC for 100 hours.**

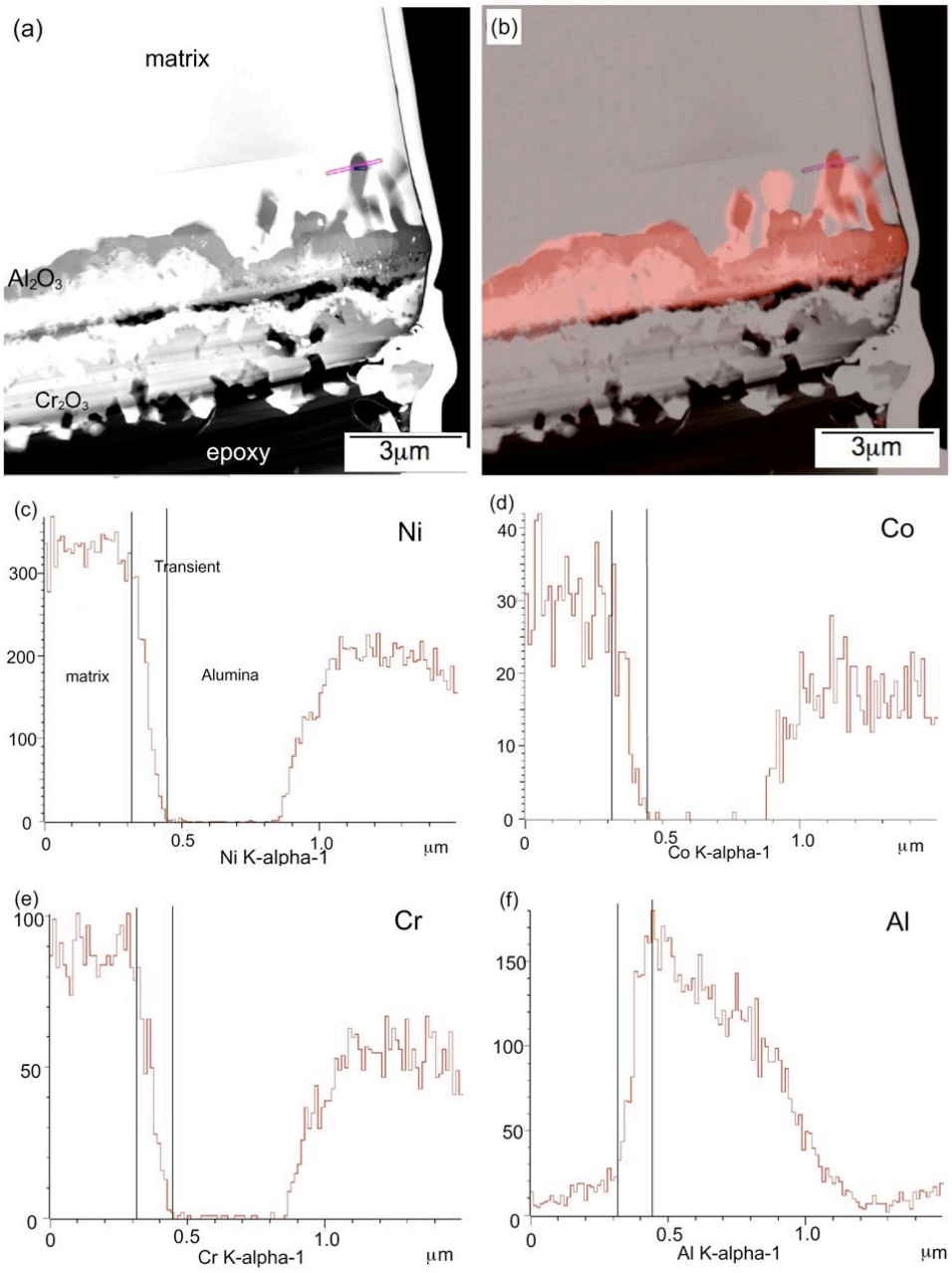


**Fig 3.7 STEM-EDX line scan analysis across part of $Al_2O_3$ layer: (a) illustration of the location of the line scan (b) bright field image (gray) + Al mapping result (red), and quantitative data for (c) Ni, (d) Co, (e) Cr and (d) Al.**

## 3.3.2 Microsegregation Analysis

In fact, further examination revealed that the morphology of the $Al_2O_3$ scale differed in the dendritic and interdendritic regions, due to variations in local composition arising from residual microsegregation inherited from the casting process. Continuous $Al_2O_3$ scale occurred preferentially at locations corresponding to the interdendritic regions – in part due to greater concentrations of Al there – and at higher oxidation temperatures, see Fig 3.3. These findings provide very strong evidence that the composition of SCA425+ is marginal with regard to the formation of a continuous $Al_2O_3$ scale.

This situation has allowed quantitative estimates to be made of the chemical compositions corresponding to marginal alumina scale formation; these are needed for the quantitative analysis presented in the final parts of the work. These estimates were made by identifying (i) locations at which the $Al_2O_3$ becomes continuous/discontinuous, and (ii) associated chemical compositions. The results are listed in Table 3.2. The chemical compositions of superalloys were analyzed by SEM-EDX at ~100 μm inwards from metal/oxide interface, to avoid any influence of the oxidation reaction. The chemical composition errors quoted in Table 3.2 were obtained by analyzing three different areas in each case. Each analysis area was about 100 $\mu m^2$; thus, the chemical compositions in Table 3.2 correspond to the average composition in 300 $\mu m^2$. The chemical compositions of matrix and the morphologies of $Al_2O_3$ analyzed in both SCA425+ exposed at 1000ºC for 300 hours and SCA425+0.5Si exposed at 900ºC for 300 hours are listed in Table 3.2. Interestingly, it can be noticed from Table 3.2 that the concentration of W correlates well with the morphologies of $Al_2O_3$.

**Table 3.2 Chemical compositions of matrix analyzed (wt.%, Ni-bal) and $Al_2O_3$ morphology (continuous or not) observed, together with the calculation result of $\Delta G_f$ and $\mathrm{Val}_t^{\mathrm{eff}}$. Note that $\mathrm{Val}_t^{\mathrm{eff}}$ shown are calculated with $c_i^{\gamma}$.**

| | Co | Cr | Mo | W | Al | Ta | Si | Conti-nuous? | $\Delta G_f$ (kJ/mol) | $\mathrm{Val}_f^{\mathrm{eff}}$ |
|---|---|---|---|---|---|---|---|---|---|---|
| SCA 425+ 1000ºC 300h | 4.86 ±0.02 | 15.12 ±0.08 | 1.01 ±0.04 | 3.85 ±0.07 | 4.64 ±0.02 | 8.49 ±0.11 | - | Yes | -591.64 ±0.26 | -0.5751 ±0.0016 |
| | 5.06 ±0.03 | 15.58 ±0.08 | 0.97 ±0.04 | 4.13 ±0.08 | 4.54 ±0.06 | 7.87 ±0.29 | - | Yes | -591.71 ±0.27 | -0.5760 ±0.0019 |
| | 5.06 ±0.04 | 15.46 ±0.11 | 0.97 ±0.07 | 4.18 ±0.10 | 4.55 ±0.05 | 7.58 ±0.30 | - | No | -591.33 ±0.27 | -0.5808 ±0.0027 |
| | 4.90 ±0.11 | 15.61 ±0.46 | 0.96 ±0.06 | 4.12 ±0.07 | 4.59 ±0.12 | 7.66 ±0.58 | - | Yes | -591.80 ±0.52 | -0.5777 ±0.0035 |
| | 4.93 ±0.15 | 15.54 ±0.62 | 1.14 ±0.45 | 3.94 ±0.19 | 4.60 ±0.10 | 8.04 ±0.49 | - | Yes | -592.14 ±1.08 | -0.5729 ±0.0063 |
| | 5.03 ±0.11 | 15.47 ±0.25 | 1.03 ±0.02 | 3.93 ±0.19 | 4.54 ±0.24 | 8.06 ±0.20 | - | Yes | -591.43 ±0.85 | -0.5775 ±0.0039 |
| | 5.05 ±0.06 | 15.53 ±0.07 | 0.97 ±0.01 | 4.01 ±0.12 | 4.50 ±0.07 | 8.09 ±0.13 | - | Yes | -591.25 ±0.28 | -0.5772 ±0.0023 |
| | 5.07 ±0.02 | 15.69 ±0.31 | 0.99 ±0.05 | 3.98 ±0.10 | 4.46 ±0.10 | 7.89 ±0.50 | - | Yes | -591.14 ±0.43 | -0.5789 ±0.0049 |
| | 5.03 ±0.12 | 15.50 ±0.13 | 0.95 ±0.12 | 3.86 ±0.12 | 4.51 ±0.12 | 8.30 ±0.15 | - | Yes | -591.20 ±0.46 | -0.5775 ±0.0025 |
| SCA 425+ 0.5Si 900ºC 300h | 4.92 ±0.03 | 15.50 ±0.29 | 1.05 ±0.04 | 3.82 ±0.06 | 4.54 ±0.10 | 8.18 ±0.44 | 0.69 ±0.06 | Yes | -627.14 ±0.96 | -0.5337 ±0.0055 |
| | 5.00 ±0.10 | 15.58 ±0.61 | 1.02 ±0.09 | 4.11 ±0.10 | 4.51 ±0.03 | 8.03 ±0.12 | 0.50 ±0.12 | No | -625.68 ±0.55 | -0.5408 ±0.0059 |
| | 5.02 ±0.02 | 15.47 ±0.24 | 0.99 ±0.02 | 4.08 ±0.08 | 4.62 ±0.05 | 7.98 ±0.25 | 0.23 ±0.23 | No | -623.91 ±0.77 | -0.5558 ±0.0090 |
| | 4.93 ±0.16 | 15.27 ±0.08 | 0.97 ±0.02 | 4.09 ±0.11 | 4.59 ±0.08 | 8.00 ±0.30 | 0.46 ±0.29 | Yes | -625.18 ±2.76 | -0.5471 ±0.0195 |
| | 4.94 ±0.08 | 15.39 ±0.16 | 0.95 ±0.02 | 4.23 ±0.10 | 4.56 ±0.06 | 7.89 ±0.28 | 0.43 ±0.06 | No | -624.99 ±0.55 | -0.5471 ±0.0056 |
| | 4.97 ±0.06 | 15.50 ±0.11 | 1.02 ±0.04 | 3.97 ±0.03 | 4.55 ±0.03 | 8.04 ±0.08 | 0.66 ±0.28 | Yes | -627.10 ±1.43 | -0.5344 ±0.0152 |
| | 5.05 ±0.10 | 15.64 ±0.41 | 1.01 ±0.03 | 4.01 ±0.23 | 4.52 ±0.01 | 8.00 ±0.42 | 0.36 ±0.27 | No | -624.57 ±2.41 | -0.5501 ±0.0137 |
| | 5.03 ±0.11 | 15.44 ±0.20 | 1.02 ±0.20 | 3.67 ±0.15 | 4.56 ±0.04 | 8.08 ±0.12 | 0.65 ±0.07 | Yes | -626.62 ±0.54 | -0.5413 ±0.0044 |

### 3.3.3 On the Transport Properties of Alumina

Before proceeding with the discussion and analysis, it is crucial to consider whether the experimental results confirm whether $Al_2O_3$ is n-type or p-type conductor, because the transport properties depend strongly upon this. Our arguments rest on the partial pressure of oxygen at the outer interface of $Al_2O_3$, consistent with the presence of other oxide species.

From a theoretical standpoint, the partial pressure of oxygen at the outer interface of $Al_2O_3$ is expected to be equal the dissociation pressure of the oxide which is continuous and lying in contact with the $Al_2O_3$. Fig.3.8 shows the Ellingham diagram of the SCA425+ alloy calculated with eq.1.1.

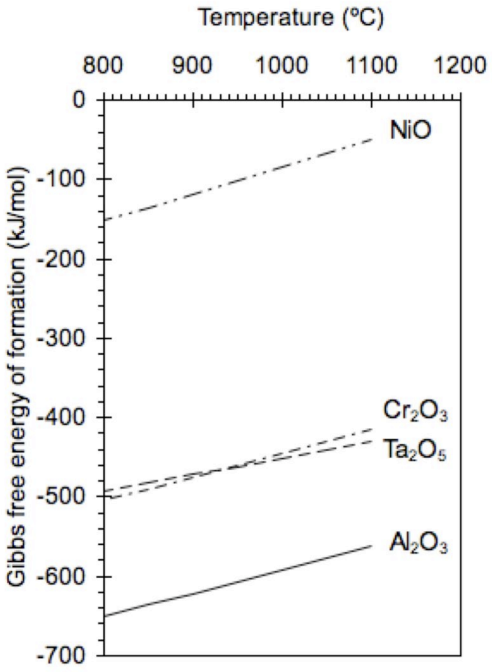


**Fig 3.8 Calculated Ellingham diagram for SCA425+.**

It indicates that $Al_2O_3$ is indeed the most stable oxide; moreover, the second and third most stable oxides at 1000ºC are predicted to be $Ta_2O_5$ and $Cr_2O_3$, respectively. Therefore, the order of oxides observed is expected to be $Al_2O_3$ -> $Ta_2O_5$ -> $Cr_2O_3$, which is consistent with the experimental results. Moreover, it is confirmed experimentally from Fig.3.3a that $Cr_2O_3$ appeared as a continuous layer. Since the dissociation pressures of $Cr_2O_3$ at 1000ºC is calculated to be $1.19\times10^{-19}$ atm (from eq.1.1), the partial pressure of oxygen at the outer interface of $Al_2O_3$ is likely to be much lower than $10^{-5}$ atm. It is known that $Al_2O_3$ is an n-type conductor at pressures less than $10^{-5}$ atm [12]. Thus, it can be assumed that $Al_2O_3$ is an n-type conductor under the conditions examined in this work. Use is made of this deduction in section 3.4.

## 3.4 Discussion and Analysis

Since SCA425+ is a marginal $Al_2O_3$ former, changes to the composition of the alloy might be contemplated to improve its oxidation performance. More generally, one would like to build analysis capability based upon sound physical principles, by which the chemical composition of nickel-based superalloys and oxidation performance are linked by a mathematical model. This could then be used to predict the changes required. What follows is a first attempt at this.

### 3.4.1 On the Free Energy for Alumina Layer Formation

Eq.3.2 indicates that the rate of oxidation depends upon the Gibbs free energy of formation $\Delta G_f$; therefore there might be a *threshold* value of this quantity which is relevant to $Al_2O_3$ layer formation.

To test this hypothesis, values of $\Delta G_f$ were determined for the compositions listed in Table 3.2, in the following way. First, estimates for $\Delta G_0$ were obtained from the literature [103]; the expressions used are given in Table 3.3. Second, activities of the elements present were calculated using the Thermo-Calc software operating on a database of thermodynamic parameters [104]. Finally, estimates for $\Delta G_f$ were made using eq.1.1, see Table 3.2. The calculated values of $\Delta G_f$ are found to lie very close to each other, which indicates that this quantity alone is insufficient for predicting $Al_2O_3$ layer performance. Thus, other factors need to be accounted for. These preliminary conclusions are supported by the more sophisticated calculations of section 3.5.

**Table 3.3 Parameters used for the calculations of $\Delta G_0$ per 1 mol $O_2$ from the literature [103].**

| | $\Delta G_0$ per 1 mol $O_2$ (kJ/mol) | Temperature range (K) | $R^2$ |
|---|---|---|---|
| $Al_2O_3$ | 0.2193*T*-1127.3137 | 1000 - 1400 | 1.00 |
| $Ta_2O_5$ | 0.1643*T*-806.6398 | 1000 - 1400 | 1.00 |
| $Cr_2O_3$ | 0.1684*T*-752.4631 | 1000 - 1400 | 1.00 |
| NiO | 0.1696*T*-468.0892 | 1000 - 1400 | 1.00 |

## 3.4.2 Determination of the Effective Valence of Alumina Scale

Previously in section 3.3.3, it is estimated that the semiconductivity of $Al_2O_3$ could be n-type on nickel-base superalloys. This means that the introduction of eq.3.5 to eq.3.7 is indeed reasonable assumption. In other words, the flux of $O^{2-}$ should be focused more than that of $Al^{3+}$, which later cases are commonly discussed in the literature. The following is the expansion of the eq.3.7 using eq.3.13 and Wagner-Hauffe theory [105]. The Wagner-Hauffe theory has further been extended so that it can be applied to a multicomponent system of the nickel-based superalloy type. According to the theory, when the valence of an impurity ion is greater than that of the parent cation $Al^{3+}$ in the oxide (as for $Ta^{5+}$, $W^{6+}$) the formation of $Al_2O_3$ is decelerated on electrochemical grounds since the dominant defect concentration (vacancies on the $O^{2-}$ lattice) is reduced. On the other hand, when the valence is lower (as for $Ni^{2+}$) the dominant defect concentration increases and the rate of formation of $Al_2O_3$ is enhanced. For the nickel-base superalloys, the possibility of a number of different impurities in the $Al_2O_3$ must be contemplated. For example, if *s* mol of NiO, *t*/2 mol of $Cr_2O_3$ and *u*/2 mol of $Ta_2O_5$ dissolve in $Al_2O_3$ (i.e. consistent with *s* mol of Ni, *t* mol of Cr and *u* mol of Ta), the appropriate dissolution reaction is

$$\begin{aligned} & s\mathrm{NiO} + \frac{t}{2}\mathrm{Cr_2O_3} + \frac{u}{2}\mathrm{Ta_2O_5} \\ & \leftrightarrow s\mathrm{Ni}_{\mathrm{Al}'} + t\mathrm{Cr}_{\mathrm{Al}} + u\mathrm{Ta}_{\mathrm{Al}''} + \underline{\left(-1\cdot s + 0\cdot t + 2\cdot u\right)e'} \\ & \quad + \frac{3\left(s+t+u\right)}{2}\mathrm{O}_{\mathrm{O}} + \left(-\frac{s}{4} + \frac{u}{2}\right)\mathrm{O}_2 \end{aligned} \tag{3.14}$$

where the underlined term indicates the equivalent opposite charges arising due to the need to maintain electroneutrality. Motivated in this way, one can define a total effective valence of the $Al_2O_3$, denoted $\mathrm{Val}_t^{\mathrm{eff}}$ and consistent with the underlined term above, as

$$\mathrm{Val}_t^{\mathrm{eff}} \equiv \sum_{n=i}\left(z_i - z_{\mathrm{Al}}\right)\overline{c}_i = \Delta e' \tag{3.15}$$

where $z_i$ is the effective valence of element $i$'s ion, and $z_{\mathrm{Al}}$ is the valence of Al ion; clearly one has $z_{\mathrm{Al}} = 3$. Here, $\overline{c}_i$ indicates the atomic fraction of element $i$ in the $Al_2O_3$ which is acting as an impurity. Since $Al_2O_3$ is an n-type conductor, as $\mathrm{Val}_t^{\mathrm{eff}}$ becomes more negative, the concentration of $O^{2-}$ anions increases so that the oxidation rate is expected to accelerate. Combination of eq.3.9, eq.3.13 and eq.3.15 leads to the following relationship

$$k_t \propto \mathrm{Val}_t^{\mathrm{eff}} \cdot \Delta G_f \tag{3.16}$$

One notes that eq.3.16 contains not just a thermodynamic factor ($\Delta G_f$) but also a term ($\mathrm{Val}_t^{\mathrm{eff}}$) which relates to the kinetics expected, owing to its proportionality to the concentration of the defects which control the transport properties through the oxide.

In the calculations which follow in section 3.5, the term $\mathrm{Val}_t^{\mathrm{eff}}$ has also been calculated according to

$$\mathrm{Val}_t^{\mathrm{eff}} \propto \sum_{n=i} \left(z_i - z_{Al}\right) c_i^{\gamma} \tag{3.17}$$

where $c_i^{\gamma}$ represents the atomic fraction of element $i$ in the γ phase at the oxidation temperature. Hence, eq.3.16 can be rewritten as

$$k_t \propto \sum_{n=i} \left(z_i - z_{Al}\right) c_i^{\gamma} \cdot \Delta G_f \tag{3.18}$$

Which of eq.3.15 or eq.3.17 exhibits the better predictive capability is tested in the following section.

To summarize, the proposed calculation method focuses on the oxidation rate expected for an $Al_2O_3$ particle growing into either the γ phase or the γ/γ' two phase mixture. Eventually, if the growth rate is sufficient, these $Al_2O_3$ particles will coalesce to form a continuous layer containing grain boundaries. Ideally, one should include the effect of the impurities factor on the grain boundary growth, as shown in Ref. [106] , since this has a major effect on the growth of $Al_2O_3$ layer. However, for the sake of simplicity, no assumptions are made here about whether the mass transport necessary occurs at the grain boundaries or within the bulk. No effect of nucleation of $Al_2O_3$ is include, which is a major assumption.

# 3.5 Oxidation Diagram for Nickel-Based Superalloys

## 3.5.1 Construction of Oxidation Diagrams

Inspired by the form of Eq.3.16, so-called oxidation diagrams can now be developed. As will be seen, these have some power for the prediction of oxidation performance and therefore are useful for alloy design purposes. Fig 3.9 illustrates the concept; on the x- and y-axes are plotted estimates of $\Delta G_f$ and $\mathrm{Val}_t^{\mathrm{eff}}$ respectively. The form of eq.3.16 indicates that isocontours of constant $k_t$ can be identified; the isocontours tend asymptotically to the two axes owing to its hyperbolic nature, but in practice it has been found that the curvature is rather gentle in the calculated regimes of interest. Alloys which form $Al_2O_3$ readily are expected to lie towards the bottom left of the diagrams (large negative $\Delta G_f$ and $\mathrm{Val}_t^{\mathrm{eff}}$ ); those for which a continuous $Al_2O_3$ scale is unlikely (small negative $\Delta G_f$ and $\mathrm{Val}_t^{\mathrm{eff}}$ ) towards the top right.

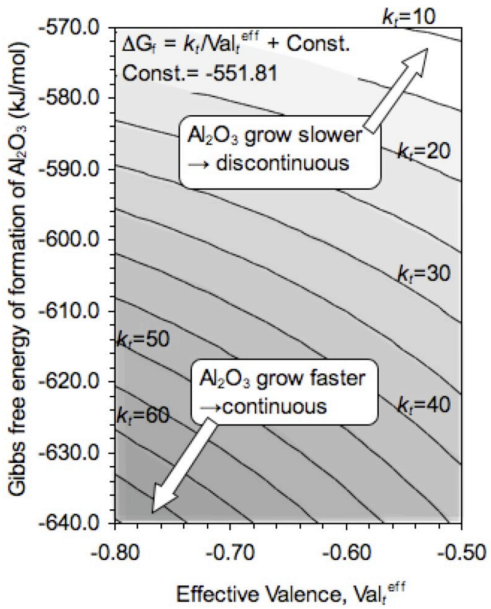


**Fig.3.9 Illustration of the oxidation diagram concept.**

Since the performance of SCA425+ has been shown to be marginal with regard to continuous $Al_2O_3$ scale formation, its composition can be used to calibrate eq.3.16 and thus to identify the location of a critical isocontour; this has been done for the temperatures 900ºC and 1000ºC on the diagrams given in Fig.3.10a and 3.10b respectively using the values of $\Delta G_f$ and $\mathrm{Val}_t^{\mathrm{eff}}$ listed in Table 3.2. Thus the calculated line which is plotted in each case passes through the point corresponding to SCA425+. Fig.3.10a & Fig. 3.10b also contains the calculated results of some well-known superalloys – chemical compositions are given in [3] – for which the oxide morphologies have been reported in the literature [3, 107-111]; the testing conditions reported are summarised in Table 3.4. Note that there is some subjectivity involved in deciding whether any given alloy does indeed form a continuous layer of $Al_2O_3$, owing to the different practices used in the oxidation testing and the details reported; however one can see that some correlation, with the alloys which perform adequately tending to lie below the calculated line, and those not performing well above it.

In fact, it has been found that the use of eq.3.17 (not eq.3.15) provides good predictive capability, *i.e.* when the calculations for $\mathrm{Val}_t^{\mathrm{eff}}$ are carried out with the atomic compositions of the $\gamma$ phase $c_i^{\gamma}$ rather than the mean compositions $\overline{c}_i$ ; Fig.3.10c and Fig.3.10d are the diagrams calculated in this way from eq.3.17. On Fig.3.10a and Fig.3.10b from eq.3.15, some results for the alloys forming continuous $Al_2O_3$ scales (points plotted with solid black circles) and discontinuous $Al_2O_3$-forming alloys (white circles) overlap. This means the result of eq.3.15 failed to predict the formation of $Al_2O_3$ layer. On the other hand, one can see from Fig.3.10c and Fig.3.10d that on the whole the black and white symbols are now well separated with each line passing through the point corresponding to SCA425+

separating the two distinct behaviours. In Fig.3.10c and Fig.3.10d, for example, IN738LC lies above the critical isocontour at both 900ºC and 1000ºC, consistent with the micrographs reported in [108, 111]. Additionally, CMSX-4, Rene'N5 and PWA1484 lie below the critical isocontour, consistent with these alloys forming an $Al_2O_3$ layer at both 900ºC and 1000ºC, and in agreement with the literature [3, 108, 109, 111]. The sole discrepancy found concerns the result for the TMS-75 alloy exposed at 900ºC for 100 hours [109], and reasons for this might be as follows. It is known that in the early (transient) stages of oxidation – before the steady-state is reached – a continuous layer of $Al_2O_3$ might not yet have become established. Furthermore, our attention has been restricted to the formation of n-type $Al_2O_3$, so that the cations are assumed to move more slowly than the anions. This is not necessarily the case for the transient theta-$Al_2O_3$ which can form in these systems at early stages [22] . The impurities effect (described with $\mathrm{Val}_t^{\mathrm{eff}}$) will be opposite when the semiconductivity changes from n-type to p-type; thus in order to avoid the risk of p-type $Al_2O_3$ in the alloy design, it is also suggested that to adhere to: $\mathrm{Val}_t^{\mathrm{eff}} \geq -0.6710$ (900ºC) and $\mathrm{Val}_t^{\mathrm{eff}} \geq -0.6439$ (1000ºC). To sum up, it can be concluded that using the atomic composition of the γ phase for the calculation of the effective valance $\mathrm{Val}_t^{\mathrm{eff}}$ provides the better predictive capability. This is consistent with the $Al_2O_3$ forming on nickel-base superalloys in contact with the γ phase (in the so-called γ' depletion zone), so that the local equilibrium $Al_2O_3/\gamma$ should be considered rather than the $Al_2O_3/(\gamma/\gamma')$ one [112].

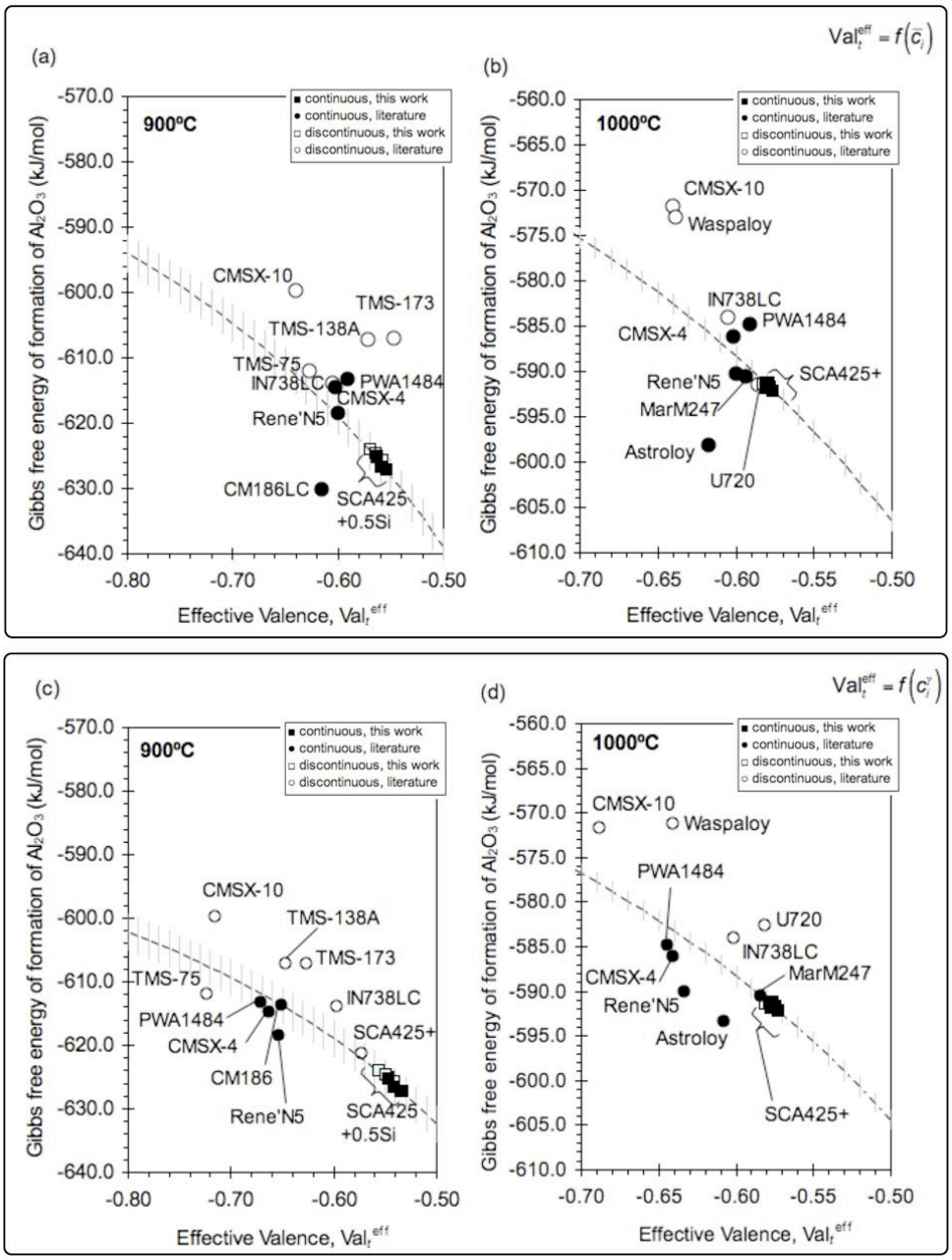


**Fig.3.10 Oxidation diagrams for SCA425+, on which the calculated Gibbs free energy for $Al_2O_3$ formation is plotted against the total effective valence for the $Al_2O_3$ scale. In (a) & (c) the calculations are carried out at 900ºC, and in (b) & (d) at 1000ºC. The total effective valence is calculated with $\overline{c}_i$ in (a) & (b) and with $c_i^{\gamma}$ in (c) & (d). Data on the diagrams are taken from this study and also those reported in [3, 107-111]. Note failure of $Al_2O_3$ layer prediction in (a) & (b); on the contrary, good agreement on the diagrams (c) & (d) which make use of $c_i^{\gamma}$ for the calculation of the total effective valence.**

**Table 3.4 Exposure conditions of superalloys in the literatures [3, 107-111, 113], and the $Al_2O_3$ morphologies observed in these studies.**

| | Exposure temperature (°C) | Exposure time (h) | Continuous $Al_2O_3$? | Ref | Note |
|---|---|---|---|---|---|
| IN738LC | 900 | 2520 | No | [108, 111] | Cyclic |
| | 1000 | 500 | No | [108] | Cyclic |
| Astroloy | 1000 | 100 | Yes | [110] | Isothermal |
| Waspaloy | 1000 | 100 | No | [110] | Isothermal |
| U720 | 1000 | 100 | No | [110] | Isothermal |
| CM186 | 900 | 3200 | Yes | [108, 111] | Cyclic |
| MarM247 | 1000 | 2500 | Yes | [108] | $P_{H2O}$=0.3 atm |
| CMSX-4 | 900 | 100 | Yes | [109] | Isothermal |
| | 1000 | 1000 | Yes | [107] | Isothermal |
| Rene'N5 | 900 | 3200 | Yes | [108] | Cyclic |
| | 1000 | 2500 | Yes | [108, 111] | Cyclic |
| PWA1484 | 900 | 100<br>3200 | Yes<br>Yes | [109]<br>[108] | Isothermal<br>Cyclic |
| | 1000 | 2500 | Yes | [108] | Cyclic |
| CMSX-10 | 900 | 100 | No | [3, 109, 113] | Isothermal |
| | 1000 | 100 | Yes, but $\beta$ -> $Al_2O_3$ | [3, 113] | Isothermal |
| TMS-75 | 900 | 100 | No | [109] | Isothermal |
| TMS-138A | 900 | 100 | No | [109] | Isothermal |
| TMS-173 | 900 | 100 | No | [109] | Isothermal |

## 3.5.2 On the Use of Oxidation Diagrams for Alloy Design

The model can be used to estimate the sensitivity of alumina scale formation to the chemical composition of any given superalloy in the following way. For example, starting with the baseline composition of SCA425+ consistent with the emphasis of this work, calculations for $\Delta G_f$ and $\mathrm{Val}_t^{\mathrm{eff}}$ can be made by systematically altering the mean chemical composition by 1at.% for each of the important alloying additions. The results can be depicted on the oxidation diagrams, with vectors identifying the changes in position of the alloy with respect to the critical isocontour for continuous $Al_2O_3$ formation. The calculated results are as follows, see Fig.3.11. First of all, as expected, additions of Al, Si, Cr are predicted to be beneficial with regard to $Al_2O_3$ formation; on the other hand, additions of W, Ta, Nb, Ru, Ti and Mo are detrimental. One can see from Fig.3.11 that either the addition of Al or removal of W or Ta is the best prescription for improving the oxidation resistance of SCA425+. Removal of W or Ta has a positive effect since the value of $\mathrm{Val}_t^{\mathrm{eff}}$ is decreased; this contrasts with effect of Al addition which is *via* a decrease in $\Delta G_f$. The oxidation diagrams allow these two competing effects to be quantified. Other suggestions arising from these quantitative calculations include (i) replacement of W and/ or Mo with Re; and (ii) substitution of Ni by Co. Note however that Co additions are reported to deteriorate $Al_2O_3$/metal bonding toughness [114]. Interestingly, the predicted influence of Si is only slight. As our experimental result in Fig.3.1 revealed that 0.25Si addition has the most beneficial for the oxidation, this calculation/experiment gap is likely to imply the additional beneficial effects of Si on the nucleation of $Al_2O_3$ formation [115], and this should be investigated furthermore, see chapter 4.

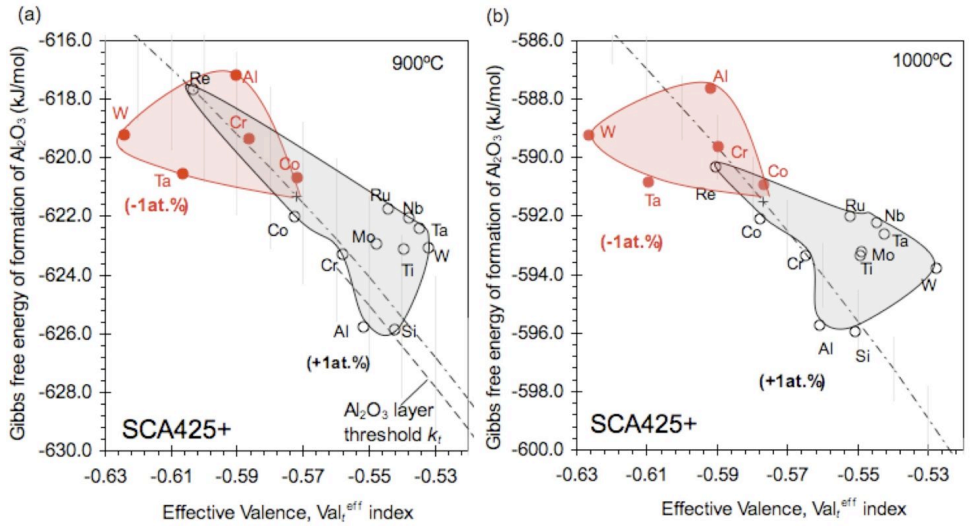


**Fig.3.11 Oxidation diagrams for SCA425+ at (a) 900ºC and (b) 1000ºC. The composition of SCA425+ is plotted as a cross; the critical isocontour passes through it. The black area is calculated by increasing the composition of SCA425+ by 1at% for each of its alloying elements; the red area by decreasing the composition by 1at%. Note that total effective valence is calculated with $c_i^{\gamma}$ .**

Finally, it should be pointed out that the calculations can be carried out for other single crystal superalloy compositions. Oxidation diagrams for the two common second generation SX superalloys PWA1484 and CMSX-4 are given in Fig.3.12 and Fig.3.13 respectively. One can see from Fig.3.12 that either the addition of Si or the addition of Re is predicted to improve the formation of $Al_2O_3$ on PWA1484. Our predictions for CMSX-4 indicate that the addition of Si is likely to be highly beneficial, see Fig.3.13. Obviously, the oxidation diagram concept contains many inherent assumptions and without doubt could be further improved upon, but we believe that it is a powerful way to link the alloy composition and oxidation performance. It has been used already to aid in the design of new alloys.

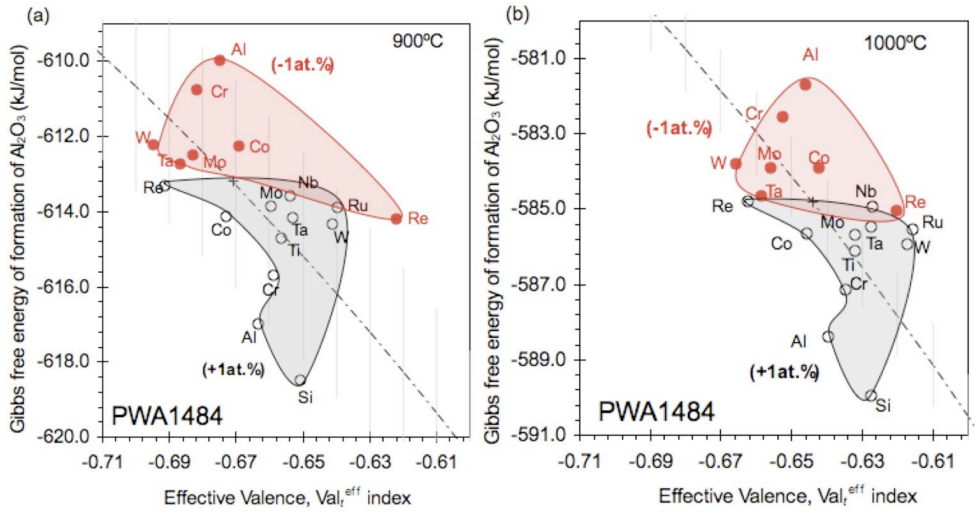


**Fig.3.12 The effect of altering alloying element concentrations on the oxidation diagram of PWA1484: (a) 900ºC and (b) 1000ºC. Note that total effective valence is calculated with $c_i^{\gamma}$ .**

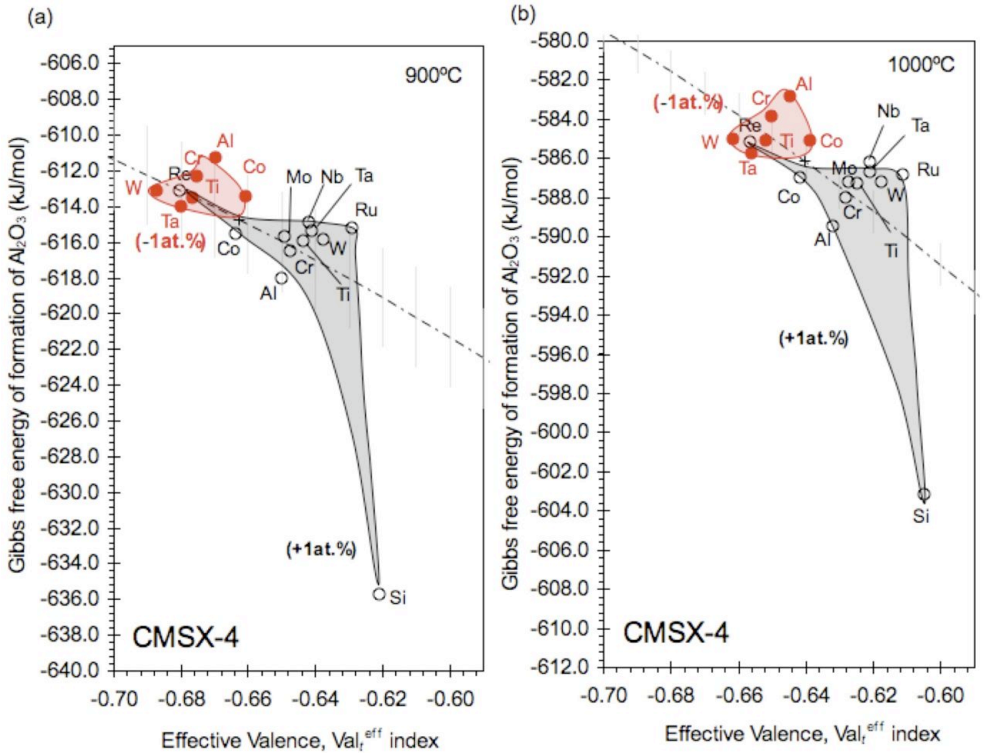


**Fig3.13 The effect of altering alloying element concentrations on the oxidation diagram of CMSX-4: (a) 900ºC and (b) 1000ºC. Note that total effective valence is calculated with $c_i^{\gamma}$ .**

## 3.6 Summary and Conclusions

The following conclusions can be drawn from this work:

(1) The SCA425+ single crystal superalloy is an alumina-former but only marginally so; higher oxidation temperatures and additions of Si promote the formation of a continuous layer of alumina.

(2) The appearance of the different oxide species in the scale formed on SCA425+ (i.e. $Al_2O_3$ –> $Ta_2O_5$/$NiTa_2O_6$–> $Cr_2O_3$ as one moves outward to the scale surface) is consistent with thermodynamic predictions and Ellingham diagram considerations.

(3) The use of an effective valance index denoted $Val_t^{eff}$ is proposed, which is dependent upon the impurities inherited during alumina formation.

(4) The composition of the $\gamma$ phase in these materials – and thus the elemental partitioning occurring – appears to play a crucial role in the formation of $Al_2O_3$.

(5) When estimates are made for $Val_t^{eff}$ and the thermodynamic driving force $\Delta G_f$ for the formation of $Al_2O_3$, the concept of an oxidation diagram can be used to predict whether any given alloy is likely to be an $\alpha$-$Al_2O_3$ former.

(6) It is demonstrated that the procedures are useful for the ranking of prototype single crystal superalloys, via alloys-by-design approaches.

# Chapter 4. Characterisation of Oxide Scale Formation on a New Single Crystal Superalloy for Power Generation Applications

## 4.1 Introduction

The oxidation behaviour of nickel-based superalloys is complicated by the number of alloying additions which are present – Al, Ti, Cr, W, Mo, Ta amongst others – so that a number of different oxide phases [8, 95, 116] are usually present in the scale. Only rarely do the scale growth kinetics conform exactly to the parabolic law, so that for many alloys the rate-controlling steps are likely to alter as the reaction proceeds. Generally, the alumina-forming superalloys exhibit excellent resistance to oxidation [14, 102, 106], and the composition of many alloys is chosen so that alumina scale formation occurs. Others are designed to form a chromia scale [13, 14] which can be beneficial when a corrosive environment is prevalent.

In this chapter, the oxidation behaviour of a prototype single crystal superalloy suitable for power generation applications is studied. Traditionally, such alloys have been designed for

use in aeroengines. However, new alloys of the type studied here are needed for industrial gas turbines, which operate in harsh environments particularly in the oil/gas and nuclear sectors [3]. The new alloy, known as SCA425+, has substantial Cr content and it is likely that its resistance to environmental degradation is superior to other alloys of comparable creep and fatigue strength [29, 117, 118]. But some important questions concerning the oxidation behaviour remain to be answered. For example, how is the phase evolution during the early stage of oxidation, before the steady-state is attained? What is the role of minor alloying additions such as Si? Application of high resolution analytical techniques is needed to address these outstanding issues.

Here, atom probe tomography (APT) and transmission electron microscopy (TEM) are used to study the formation of oxide scale in this alloy under conditions relevant to engine operating conditions. The APT method in particular has yet to be widely applied to the characterization of oxide scales in these materials and is likely to provide information complementary to that gleaned from TEM studies. We consider particularly the role played by Si [82-85] which has been added in small quantities to the alloy studied to determine whether scale formation and retention is improved.

In order to place the present work in context, one should consider the rationale used for the design of the SCA425+ alloy. Use was made of the concept of an oxidation diagram, built via analysis of thermodynamic and kinetic factors which govern alumina formation [119], see Figure 4.1. The composition of any given alloy is plotted as a point on the diagram, as determined by (i) the thermodynamic driving force for the alumina formation [8, 9, 11] and (ii) a kinetic parameter which captures the influence of impurities in the alumina scale [105] inherited from the superalloy substrate. Alloys which readily form alumina scales lie towards the bottom left of the diagram; those for which alumina scale

formation is more sluggish lie at the top right. Figure 4.2 illustrates results for the cyclic oxidation resistance of SCA425+ at 900ºC, for cycle time of 65 hr. One can see that the new alloy SCA425+ shows excellent resistance to cyclic oxidation.

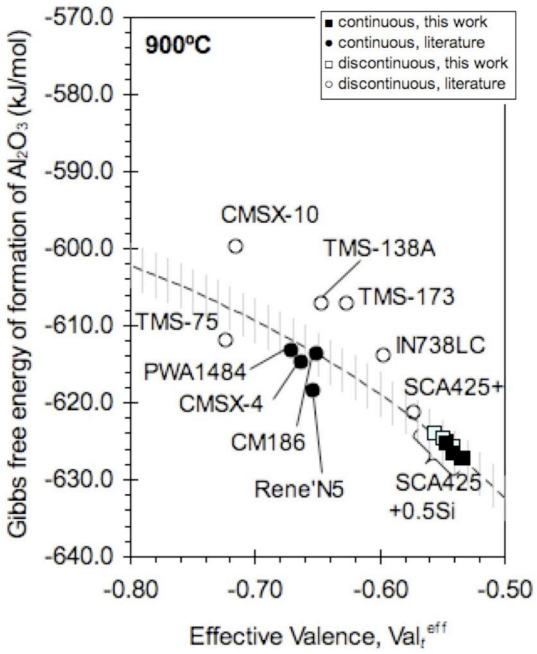


**Fig.4.1 Oxidation diagram for SCA425+, on which the calculated Gibbs free energy for $Al_2O_3$ formation is plotted against the total effective valence for the $Al_2O_3$ scale [119].**

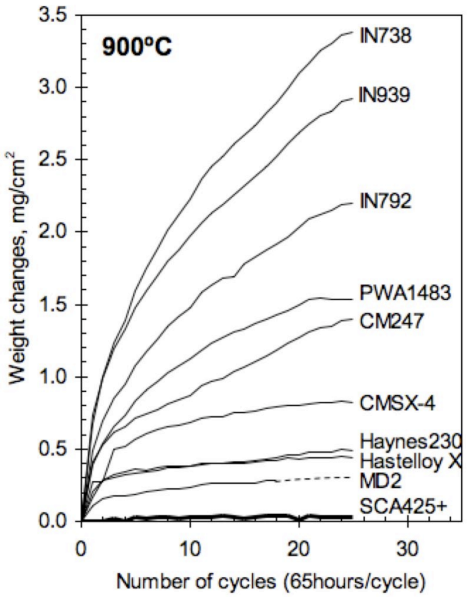


**Fig.4.2 Comparison of cyclic oxidation resistance of SCA425+ with other alloys, at 900ºC and with cycle time of 65 hours. All experimental data were obtained in this study.**

## 4.2 Experimental Details

The chemical composition of SCA425+ used in the present work is given in Table 4.1. Variants with 0 wt.%, 0.25 wt.% and 0.5 wt.% Si addition were studied. Single crystal testpieces in the form of 15 mm cylindrical bars were prepared in an industrial-scale investment casting furnace at the University of Birmingham, and then solution heat treated at 1260ºC for 1 hr, 1280ºC for 5 hour, followed by air cooling. The first and second ageing treatment used was 1120ºC for 24 hr and 850ºC for 20 hours respectively, followed by air cooling.

**Table 4.1 Nominal compositions (wt.%, Ni-bal) of superalloys investigated.**

| | Co | Cr | Mo | W | Al | Ta | Hf | Si |
|---|---|---|---|---|---|---|---|---|
| SCA425+ | 5.0 | 15.5 | 1.0 | 4.0 | 4.55 | 8.0 | 0.1 | - |
| SCA425+0.25Si | 5.0 | 15.5 | 1.0 | 4.0 | 4.55 | 8.0 | 0.1 | 0.25 |
| SCA425+0.5Si | 5.0 | 15.5 | 1.0 | 4.0 | 4.55 | 8.0 | 0.1 | 0.5 |

For thermogravimetric analysis (TGA), samples of 1 cm × 2 cm × 0.5 mm were prepared by standard grinding/polishing procedures [119] and thoroughly cleaned in an ultrasonic bath of ethanol prior to testing in a balance calibrated to better than ± 50 μg. To supplement the TGA analysis, 2 mm thick discs were taken from the heat treated material, polished, placed in an alumina boat and exposed isothermally at temperatures between 900 and 1000 ºC for various periods of time. The oxidized samples were subjected to X-ray diffraction (XRD) analysis using a standard diffractometer utilizing Cu $K_\alpha$ radiation.

Electron microscopy study was carried out in two ways. Firstly, cross-sections were analysed using back-scattered electron (BSE) imaging in a field emission gunned scanning electron microscope (FEG-SEM) equipped with energy dispersive X-ray spectroscopy (EDX). Secondly, transmission electron microscopy (TEM) foils were prepared on an FEI Quanta 3D-FEG FIB/SEM to a thickness of approximately 150 nm; they were then

cleaned with a 5 keV Ga ion beam of 48 pA. The samples were subsequently analysed on an FEI Tecnai F20 microscope using an Oxford Instruments X-max silicon drift detector. Because the energy peaks from Ta and Si lie close to each other, FEG-SEM and STEM cannot in practice distinguish between these two elements; thus, atom probe tomography was necessary.

Atom-probe tomography specimens containing the oxide scale were prepared from the alloy oxidized for 3 hrs using a standard focused ion beam milling lift-out approach [120]. While cooled to 50K, the specimens were analyzed using a LEAP 4000HR microscope operated in laser pulsing mode using UV wavelength, a pulse energy of 60 pJ, and a pulsing rate of 100kHz.

## 4.3 Results

Fig.4.3 illustrates the weight changes observed in the three SCA425+ alloys at 950ºC. Significant beneficial effect of silicon is observed. Alloying with 0.25wt.% Si gave the best oxidation resistance; further silicon addition from +0.25 to +0.5 wt.% increased the stabilized parabolic oxidation rate from $1.09\times10^{-14}$ to $1.39\times10^{-13}$ $g^2\ cm^{-4}\ sec^{-1}$. Fig.4.4 illustrates the cross-sections of oxide formed on the dendrite core regions of the three SCA425+ alloys after exposure at 950ºC for 100 hours. The black regions in the right hand sketches represent alumina scales. It is noted that alumina formed on all alloys, however, the silicon-free alloy does not form a continuous alumina layer. On the other hand, doping with silicon promotes the formation of a continuous layer of alumina (see Fig.4.4b and 4.4c).

Cross-sections of oxide scales formed at 950ºC after 0.1 hour are shown in Fig.4.5. One can see that a continuous oxide scale has already formed after 0.1 hour. This is consistent with the EDX mapping (see Fig.4.6a) which shows an outer layer of chromia with a continuous film of alumina beneath it, at this short time. Chromia is solely detected by XRD, see Fig.4.7a. Notable is the absence of any nickel oxide or spinel phases reported in the classical papers of Pettit and co-workers on ternary Ni-Al-Cr alloys [13, 14]. Analysis of our images and in particular the location of fiducial marks inherited from specimen polishing would suggest that both chromia and alumina at this stage are outward growing (see Fig.4.6a). After exposure to 3 hours, alumina has started to form internally in a finger-like morphology, see Fig.4.6b. Also, alpha-$Al_2O_3$ and chromia are detected by XRD, see Fig..4.7b. Furthermore, APT analysis (Fig. 4.8) indicates the presence of at least 2 different oxide phases. The Cr-rich oxide phase has a measured composition of 58.1%O-41.1Cr-0.7Al-0.1Si, which is consistent with $Cr_2O_3$. The measured composition of

the Al-rich phase is 53.0%O-44.3Al-1.1Cr-0.6Si-1Ta, suggesting a possible oxygen deficiency for $Al_2O_3$.

STEM was also used to analyse for any possible presence of $SiO_2$, since a thin amorphous $SiO_2$ layer (~40 nm) at the metal/oxide interface has been reported to decrease the oxidation rate [121, 122]. Such a continuous $SiO_2$ layer has not been observed in the SCA425+0.25Si, see Fig.4.6b. However, atom probe analysis revealed the presence of Si and Ta within the $Al_2O_3$ formed after 3 hours of oxidation, see Fig.4.8. Si and Ta were found clustered together in the range 15 to 70 nm from the metal/oxide interface. This clustering effect is discussed further in the following section.

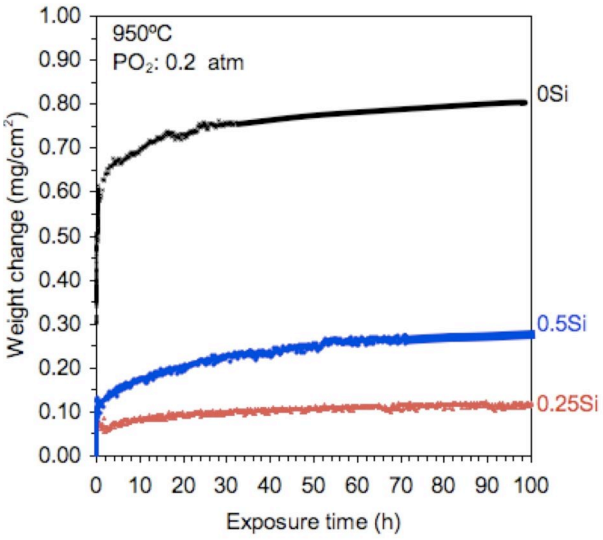


**Fig.4.3 Weight changes observed by thermal gravimetric analysis in SCA425+ with and without Si, during exposure at 950°C.**

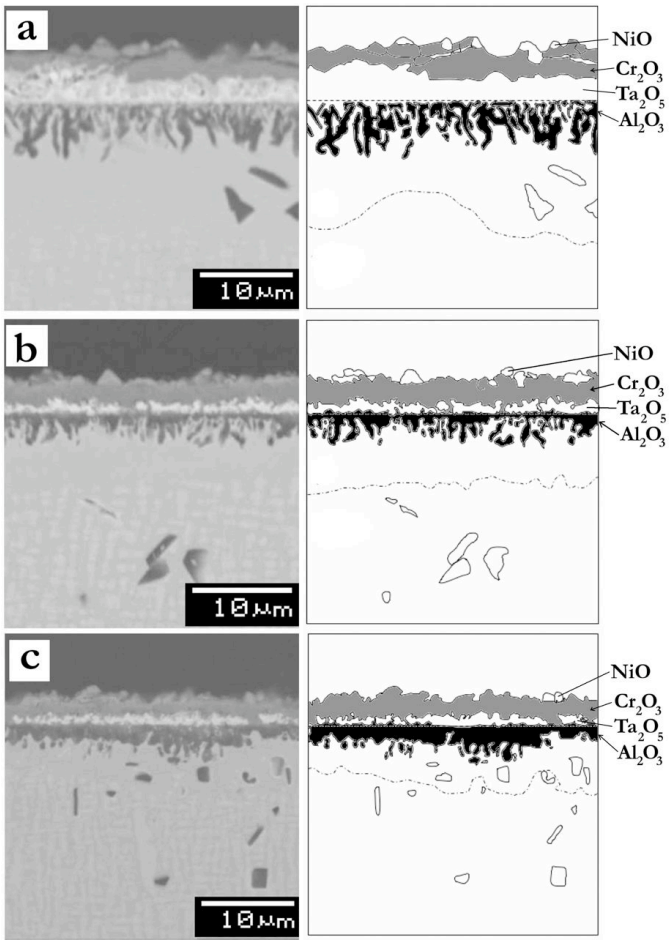


**Fig.4.4 SEM micrographs of (a) SCA425+, (b) +0.25wt.%Si and (c) +0.5wt.%Si exposed at 950ºC for 100 hours, respectively. Note that with increasing silicon alloying, there is a tendency to form a more continuous $Al_2O_3$ scale.**

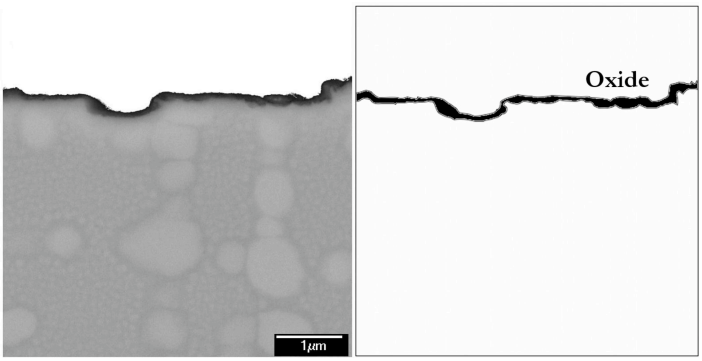


**Fig.4.5 FEG-SEM micrographs of SCA425+0.25Si exposed at 950ºC for 0.1 hour.**

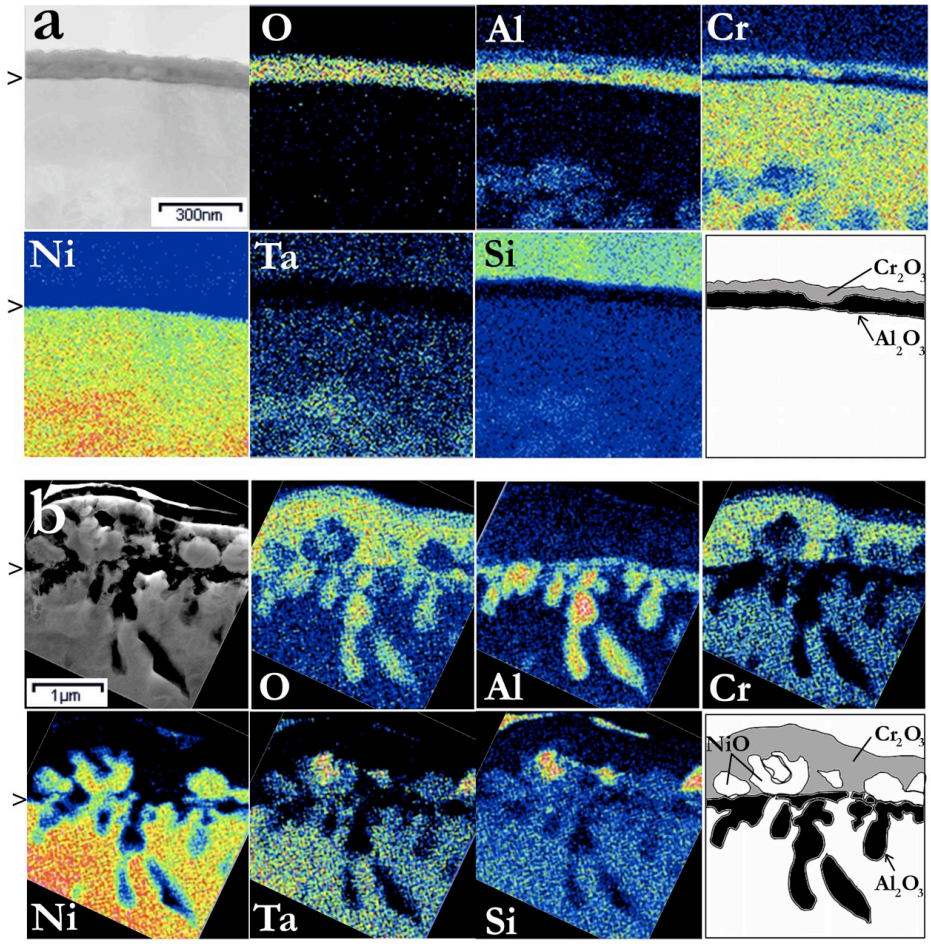


**Fig.4.6 STEM-EDX chemical mapping of SCA425+0.25Si exposed at 950ºC for (a) 0.1 hour and (b) 3 hours, respectively.**

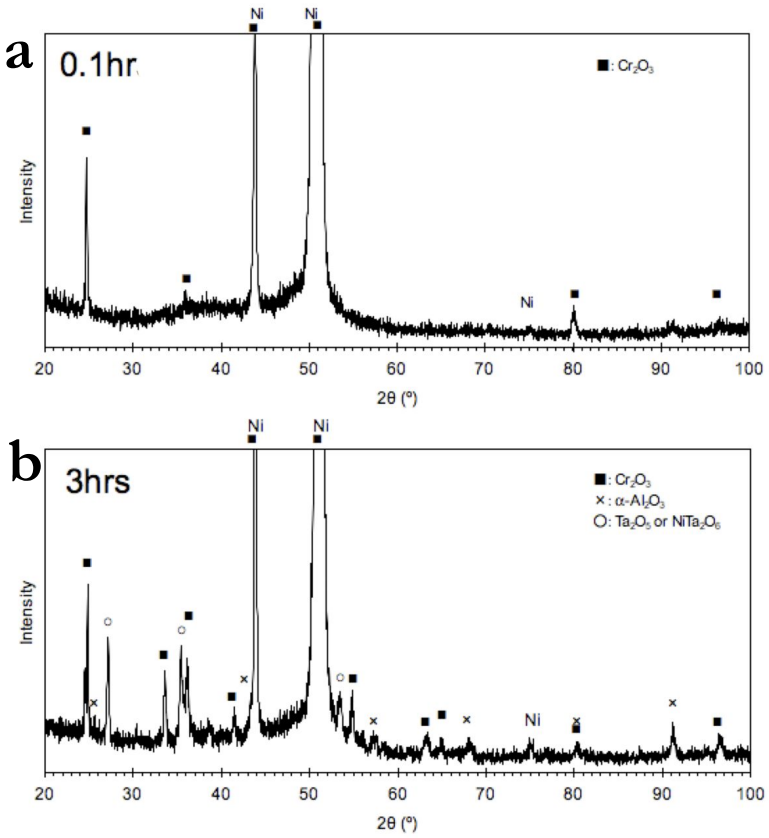


**Fig.4.7 X-ray diffraction patterns of oxide formed on SCA425+0.25Si after exposure at 950ºC for (a) 0.1 hour and (b) 3 hours, respectively.**

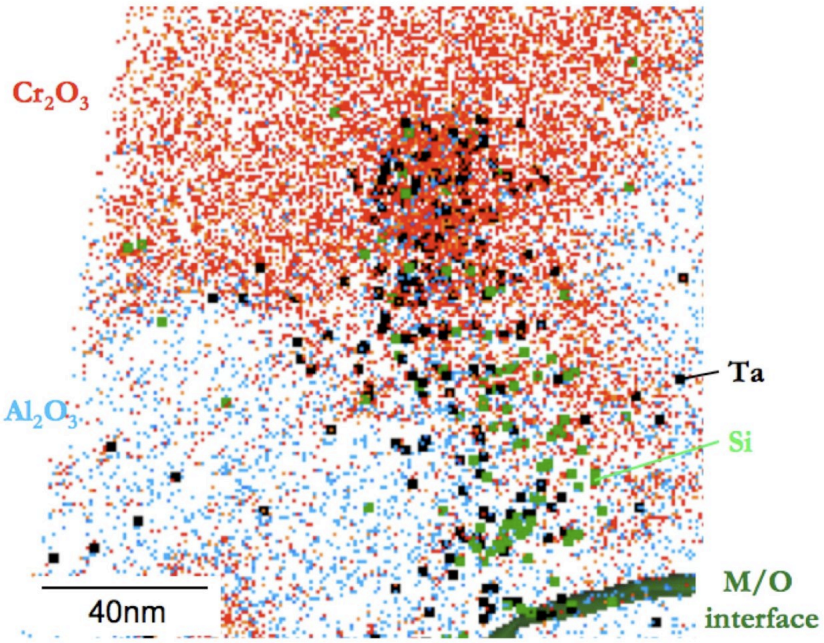


**Fig.4.8 Atom probe mapping result on SCA425+0.25Si exposed at 950ºC for 3 hours. Al, Cr, Si and Ta in $Cr_2O_3$ and $Al_2O_3$/matrix interface are shown.**

# 4.4 Discussion and Analysis

## 4.4.1 Oxidation Kinetics with and without Silicon

Our results indicate that oxidation of this high-Cr nickel-based superalloy is not governed by a simple parabolic thickening law. Thus the parabolic thickening constant varies with time, and to aid in our analysis values can be estimated from our raw data. Fig.4.9 summarises the variation of instantaneous parabolic oxidation constant $k_p$ measured for SCA425+ with and without Si. Also shown are values of $k_p$ representative of NiO, $Cr_2O_3$ and $\alpha$-$Al_2O_3$ which form on different Ni-based systems, taken from the literature [100]. One can see that in SCA425+ the early stage of oxidation rate corresponds to that of $Cr_2O_3$ or perhaps NiO, rather than $\alpha$-$Al_2O_3$. This implies that $\alpha$-$Al_2O_3$ is unlikely to be rate-controlling at the beginning of the reaction. The formation of well-defined layers of $Al_2O_3$ and $Cr_2O_3$ is thought to be a consequence of the gradient in oxygen partial pressure set up, rather than an effect of any miscibility gap in the $Al_2O_3$-$Cr_2O_3$ system [123]. One can also see from Fig.4.9 that the parabolic oxidation rate at 950ºC or above on Si-containing alloys decreases within a very short period of time. Fig.4.10 shows a time-temperature-transformation (TTT) diagram for the time for the parabolic thickening constant $k_p$ to be lowered to the value representative of $\alpha$-$Al_2O_3$ formation. The critical $k_p$ values at different temperatures were obtained from the literature [100], and the critical times were interpolated from the Arrhenius plots of Fig.4.9. One can see from Fig.4.10 that the addition of Si decreases the transformation time to reach $k_p$ values representative of $\alpha$-$Al_2O_3$ by an order of magnitude.

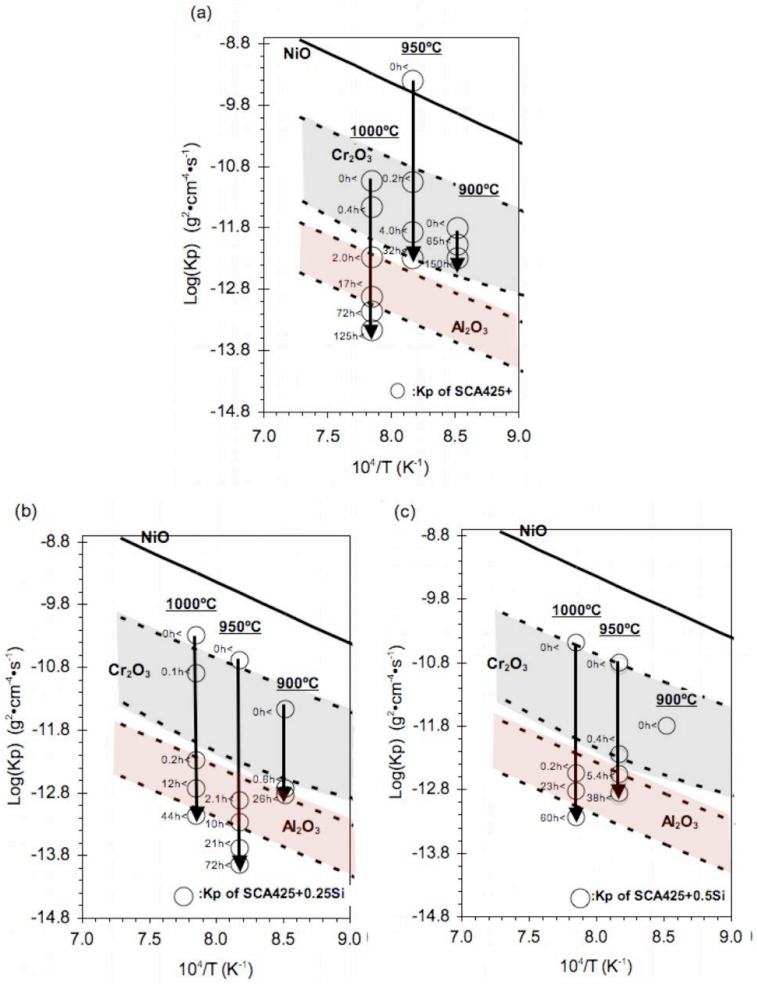


**Fig.4.9 Comparison of the parabolic oxidation constants $k_p$ of SCA425+ between 900ºC and 1000ºC, with the $k_p$ of pure oxides from the literature [100]: (a) SCA425+, (b) SCA425+0.25Si and (c) SCA425+0.5Si.**

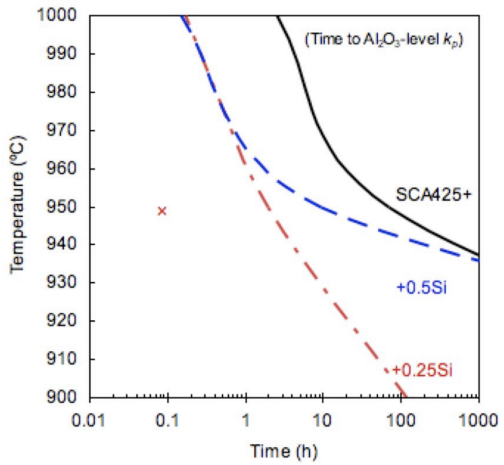


**Fig.4.10 TTT diagram for the parabolic thickening constant to be lowered to the value representative of alumina formation. At the point X, an outward growing transition alumina is already formed.**

## 4.4.2 General Transport Mechanism in Alumina

Before considering the effect of Si on the formation of alumina, one should consider first the mechanisms of transport which are recognised for alumina. The mechanism in $\alpha$-$Al_2O_3$ is known to depend upon the partial pressure of oxygen, it being an n-type conductor for partial pressures < $10^{-5}$ atm [12]. At partial pressures this low, inward diffusion of oxygen ions is thus rate-controlling; for example Rybicki et al confirmed that inward oxygen ion transport *via* grain boundary diffusion occurs in $\alpha$-$Al_2O_3$ scales with a columnar morphology [17]. However, $Al_2O_3$ is also known to exist in metastable $\gamma$- and $\theta$-forms which can transform later to $\alpha$-$Al_2O_3$ [15-17, 20, 22]. In general, parabolic oxidation rates $k_p$ of these different $Al_2O_3$ polymorphs are in the order $\gamma \approx \theta >> \alpha$ [15]; thus, $\alpha$-$Al_2O_3$ shows superior oxidation resistance. It has been concluded that $\theta$-$Al_2O_3$ grows primarily by the outward transport of Al [22, 124]. In this study, formation of alumina is already observed in the alloy containing 0.25 wt.% Si alloy after 0.1 hour exposure at 950°C, before the $k_p$ reaches a level representative of $\alpha$-$Al_2O_3$. This, together with our TEM observations, suggests that metastable alumina is forming in the early stages of oxidation.

### 4.4.3 Oxidation Diagram Theory for Silicon Addition

To attempt a first rationalisation of the beneficial effect of silicon, consider first the oxidation diagram concept proposed in [119]. The parabolic oxidation constant $k_t$ is expected to be of the form

$$k_t \propto \sum_{n=i} \left(z_i - z_{\mathrm{Al}}\right) c_i^{\gamma} \cdot \Delta G_f \tag{4.1}$$

where $\Delta G_f$ is the Gibbs free energy of formation of $Al_2O_3$ [8, 9], and $z_i$ is the effective valence of element $i$'s ion, $z_{\mathrm{Al}}$ is the valence of Al ion, and $c_i^{\gamma}$ is the atomic fraction of element $i$ in the matrix $\gamma$ phase at the oxidation temperature. Note that the matrix compositions are employed due to the formation of alumina in a region depleted of $\gamma'$, see Fig.4.4. The summation term in equation 4.1 is referred to as the total effective valence, $\mathrm{Val}_f^{\mathrm{eff}}$. Fig.4.1 illustrates the oxidation diagram with $\Delta G_f$ and $\mathrm{Val}_f^{\mathrm{eff}}$ plotted for various alloys. Alloys which form $Al_2O_3$ readily lie towards the bottom left of the diagrams (large negative $\Delta G_f$ and $\mathrm{Val}_f^{\mathrm{eff}}$). Considering SCA425+, one can see from Fig.4.1 that the addition of silicon is predicted to lie on the same isocontour line, so that Si is predicted to have – inconsistent with experience – no effect on the oxidation of SCA425+. Clearly, the theory of [119] fails to explain the beneficial effect of Si.

Nonetheless, our results confirm a beneficial effect of Si on alumina scale formation, and thus another explanation needs to be identified. We have detected clustering of both Si and Ta within the alumina formed at the early stage of growth after 3 hours, close to the scale/metal interface, see Fig.4.8. Segregation of Ta to the grain boundaries in $Al_2O_3$ is well known to occur [106]; since Si and Ta have been detected in close proximity, it seems possible that the Si clustering found here is associated with grain boundary segregation, see Fig.4.8.

A number of effects might then be occurring. First, Si might play in role in altering the oxidation rate *via* an effect on the rate of transformation of metastable alumina to its stable $\alpha$-$Al_2O_3$ form. Additions of $SiO_2$ to $\alpha$-$Al_2O_3$ have in fact been suggested to decrease the metastable -> stable $Al_2O_3$ transformation temperature, by increasing the number of nucleation sites for transformation [125]. Alternatively, Si may play a role in hindering the inward growth of $\alpha$-$Al_2O_3$ during the process of internal oxidation, via an effect on the rate of migration of oxide ions towards the metal. A significant amount of further experimental work is needed to identify more clearly the role played by Si.

## 4.5 Conclusions

The following conclusions can be drawn from this work:

(1) A continuous alumina scale forms on the superalloy SCA425+ during oxidation at 950ºC when it is alloyed with silicon; in the absence of silicon, internal oxidation is more prevalent.

(2) The optimum level of Si doping is about 0.25wt%; at a greater concentration, the oxidation resistance is impaired.

(3) STEM-EDX analysis indicated that an out-growing alumina scale formed in association with chromia in the early stages of oxidation.

(4) No continuous $SiO_2$ layer was detected in the oxide scale using STEM-EDX analysis.

(5) Atom probe tomography indicates that Si is present as clusters in the alumina; these may be associated with alumina grain boundaries. Further work is needed to confirm this.

# Chapter 5.
# On the Mechanical Behaviour of a New Single Crystal Superalloy for Industrial Gas Turbine Applications

## 5.1 Introduction

New nickel-based superalloys [1,2] are needed for hot section components – *e.g.* turbine blades and guide vanes – in the next-generation gas turbine engines required for power generation applications. Significant demands will be placed on these materials. For instance, excellent resistance to environmental attack is required, since the operating conditions and fuels used for these applications induce oxidation and corrosion; thus the superalloys used will be distinct from those currently employed for aeroengine applications. Moreover, they must withstand the large mechanical loads necessary for efficient extraction of mechanical energy from the hot gas stream. Hence creep [5, 31] and fatigue [62, 126] must be resisted. Recently, a new grade of single crystal superalloy has been developed for such applications, which displays a good balance of environmental and mechanical properties [119, 127]. Its Cr content (at 15 wt%) is substantially greater than for existing

single crystal superalloys, which improves significantly the resistance to oxidation and corrosion [128].

This work is concerned with the mechanical performance of this new single crystal superalloy. In common with most precipitation-hardened systems, the properties displayed will depend in a sensitive fashion upon the microstructure developed during heat treatment; for this class of material, hardening is by the gamma prime (γ') phase and thus conditioning of the microstructure at temperatures in and around the γ' solvus is expected to influence the mechanical properties displayed. Two distinct forms of mechanical response are studied as a function of the heat treatment applied. First, creep deformation which is important due to the centrifugal loading experienced by the turbine blades in the engine [5, 31]. Second, thermomechanical fatigue (TMF) which is relevant particularly for smaller (aeroderivative) industrial gas turbines (IGTs) on account of the interaction of thermal and mechanical strains arising from engine start up/cool down [51, 58]. As mission requirements become more demanding, it is becoming apparent that the performance of the material under TMF conditions can be life-limiting; however, historically very much more attention has been paid to the provision of creep resistance [3]. Probably this is due to the significant extra difficulty imposed by the constraints of TMF testing, but nonetheless this situation needs to be corrected. Here, it is demonstrated that significant differences exist between the underlying micromechanisms of creep and TMF in these materials. This situation has ramifications for the performance of these materials under service loading conditions.

Fig.5.1 illustrates the difficulty which has traditionally been faced by the designers of industrial gas turbines (IGTs). Existing of-the-shelf superalloys fall into one of two distinct classes: (a) those of high Al/Cr ratio, which exhibit good creep resistance but only

moderate corrosion resistance, due to their limited Cr content – examples are CMSX-4 and Rene'N5 which are used for aeroengine applications, and (b) those of lower Al/Cr ratio which have better corrosion resistance but only moderate high temperature strength – these tend to be polycrystalline alloys such as IN792. As Fig.5.1 indicates, a target design space exists for new corrosion-resistant IGT alloys of balanced Al and Cr contents. Also shown are isocontours of constant γ' fraction but of varying Ta/Al ratios which were used in the alloy design process for the new single crystal superalloy, denoted SCA425+. The higher Ta content is expected to improve the high temperature strength but also to improve its castability. The new alloy has been shown to exhibit excellent resistance to environmental degradation [119]; the purpose of the present work is to study its mechanical performance.

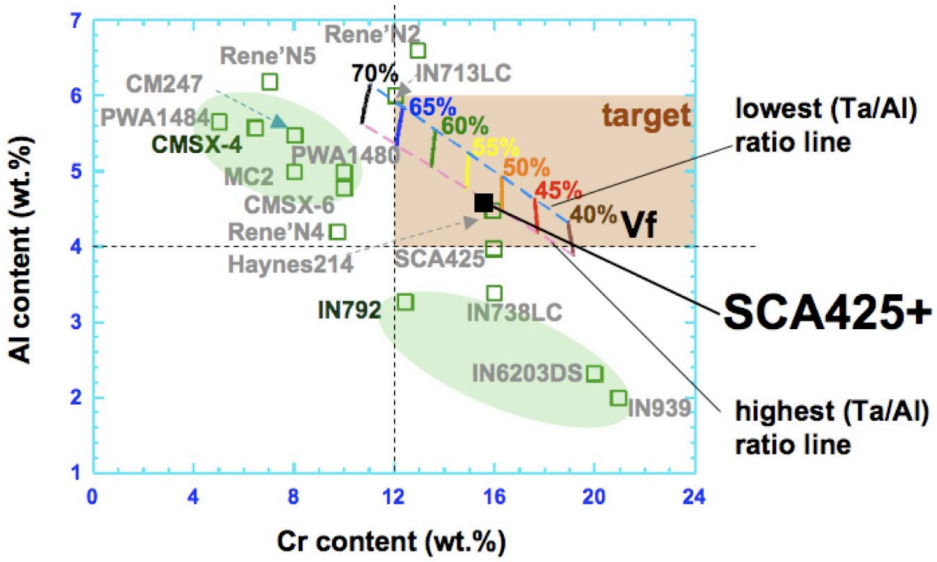


**Fig.5.1 Illustration of the locations of common nickel-based superalloys on a plot of Cr and Al contents, illustrating the location of the new SCA425+ alloy and the target design space.**

## 5.2 Results

### 5.2.1 Characterisation of Solvus Temperature and γ' Approach Curve

Optical micrographs of as-cast SCA425+ exposed at 1260ºC, 1280ºC, 1300ºC and 1320ºC for 2 hours are given in Fig.5.2. Note that the casting direction is vertical so that the difference in contrast is due to the scale of the dendritic structure inherited from casting; the microporosity resides in the interdendritic regions. Fig.5.2 indicates that exposure at 1320ºC caused incipient melting, but lower temperatures (Fig.5.2a, 5.2b and 5.2c) did not. Therefore, the solution treatment chosen for SCA425+ was: 1280ºC 1 hour -> 1300ºC 5 hours, followed by air-cooling. This was consistent with the results of the DSC calorimetry which indicated that the solidus temperature is 1318ºC, the liquidus 1364ºC and the solvus temperature 1196ºC, see Table 5.1.

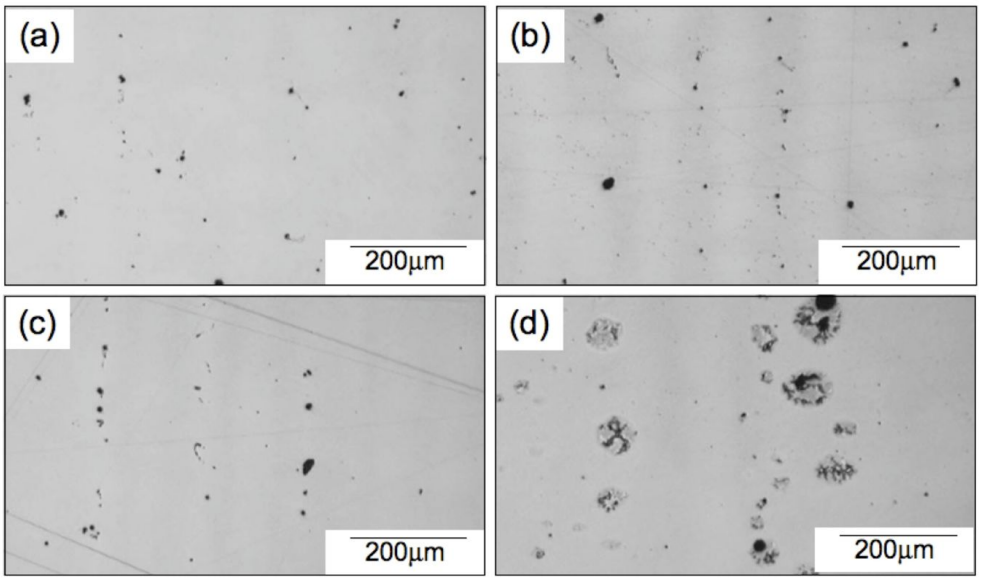


**Fig.5.2 Low magnification optical micrographs of solution treated SCA425+ exposed at (a) 1260ºC, (b) 1280ºC, (c) 1300ºC and (d) 1320ºC for 2 hours, respectively. Note in (d) the incipient melting at the interdendritic regions.**

**Table 5.1. The liquidus, solidus and solvus temperatures of the SCA425+ alloy measured by DSC and calculated using the Thermocalc software [104].**

| | Liquidus (ºC) | Solidus (ºC) | Solvus (ºC) |
|---|---|---|---|
| Experiment (DSC) | 1364 | 1318 | 1196 |
| Calculation (Thermocalc) | 1360.62 | 1315.88 | 1173.22 |

These estimates are consistent with those made using Thermo-calc and a thermodynamic databank [104]. Fig.5.3 illustrates how the volume fraction of the γ' phase varies with respect to temperature – this may be termed the γ' approach curve. Plotted are the data from the neutron diffractometry (i.e. $S_{(100)}/S_{(200)}$), but also data deduced from the DSC (at 1200ºC) and the metallography (at 850ºC). The DSC result indicates that the volume fraction of γ' in SCA425+ alloy reduces to zero at 1196ºC, the solvus temperature. The γ' approach curve aids in the design of the primary heat treatment schedules, see section 5.2.2. Neutron diffraction analysis confirmed the lattice misfit, see Fig.5.4: slightly negative, yet small; this should aid in the retention of mechanical properties during service.

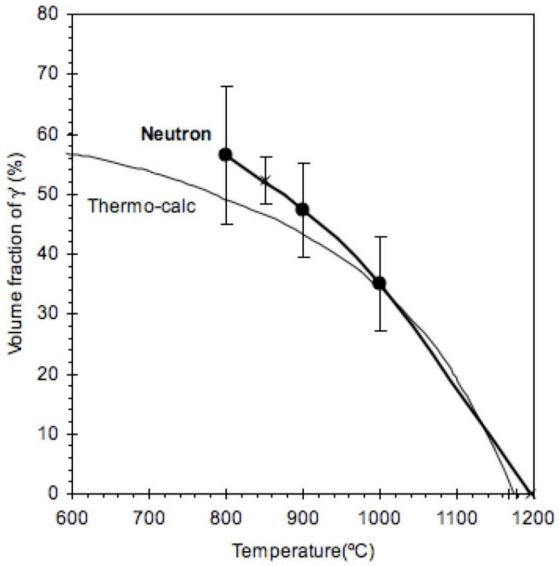


**Fig.5.3 Variation of the fraction of the γ' phase for SCA425+ with respect to temperature. Note that the dotted line represents the result from Thermo-Calc with Ni-database ver.6 [104].**

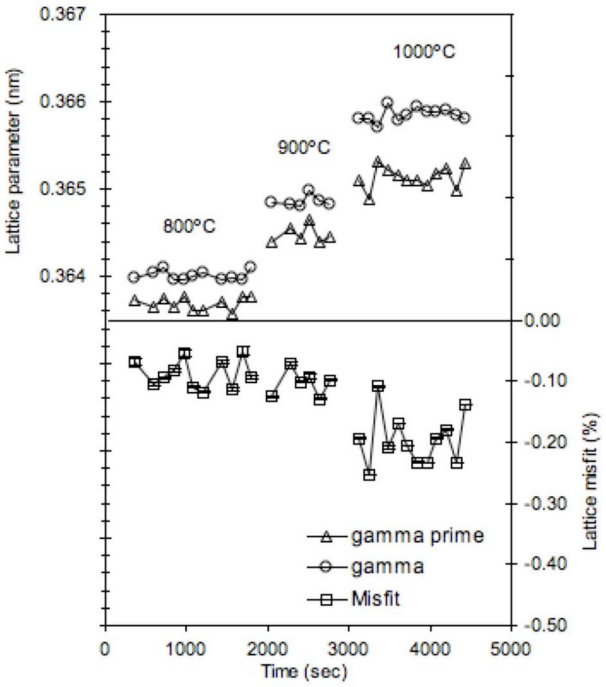


**Fig.5.4 The lattice parameters of the γ and γ' phases and the associated lattice misfit in SCA425+ analysed by in-situ neutron diffraction in this study. Experimental data were obtained at 800ºC, 900ºC and 1000ºC. Note that the first ageing condition was 1100ºC for 4 hours.**

## 5.2.2 Optimisation of Heat Treatment and Gamma Prime Microstructure

The effect of temperature and time on the γ' microstructure developed during primary ageing has been studied, since these need to be chosen carefully for optimised mechanical properties [129]. Fig.5.5 shows micrographs of fully heat-treated SCA425+ with different first ageing conditions.

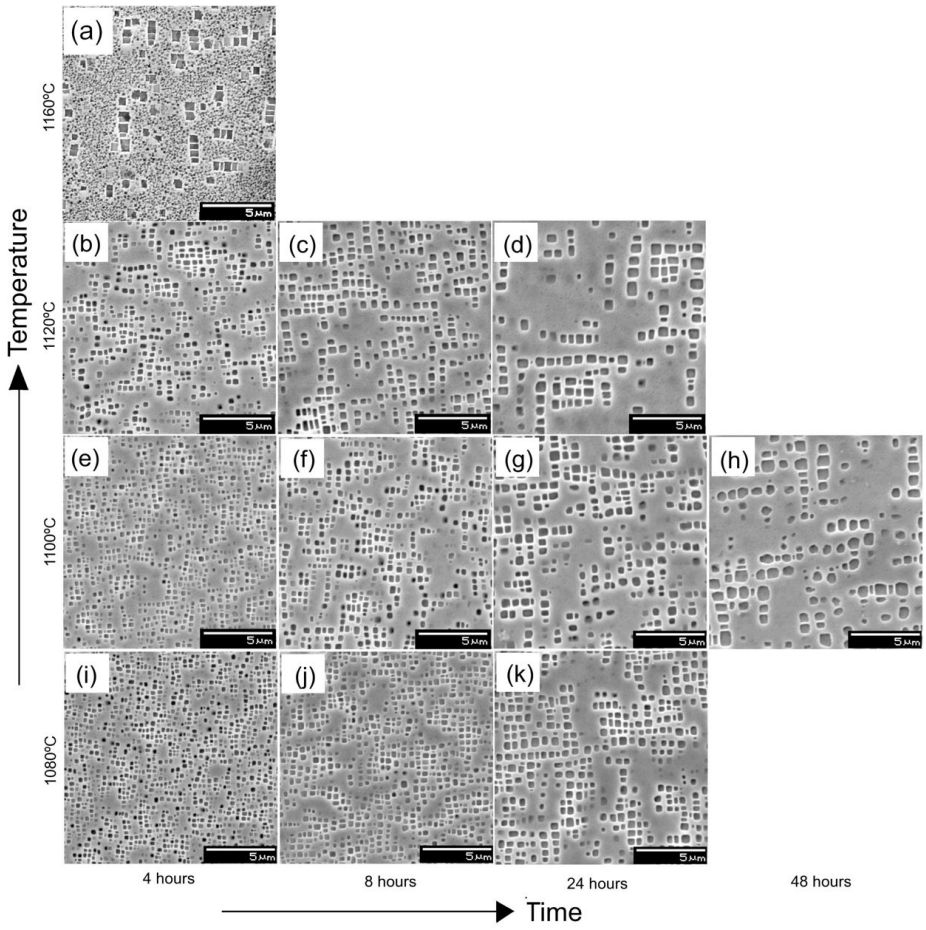


**Fig.5.5 Scanning electron micrographs of fully heat-treated SCA425+ with different first ageing conditions: (a) 1160ºC 4 hours, (b) 1120ºC 4 hours, (c) 1120ºC 8 hours, (d) 1120ºC 24 hours, (e) 1100ºC 4 hours, (f) 1100ºC 8 hours, (g) 1100ºC 24 hours, (h) 1100ºC 48 hours, (i) 1080ºC 4 hours, (j) 1080ºC 8 hours and (k) 1080ºC 24 hours, respectively. Note that solution treatments, second ageing conditions and cooling conditions are the same in all cases.**

The primary γ' particles coarsen with increasing temperature and time, consistent with well established theory [64, 65]. Moreover, the amount of primary γ' decreases with increasing ageing temperature, as this approaches the γ' solvus temperature of 1196ºC. The γ' morphologies of Fig.5.5 were further analyzed using image-processing methods, see Fig.5.6 and Table 5.2; based upon the LSW theory and associated constant from the literature [66-68, 130-132], the coarsening behaviour of Fig.5.5 was as expected. Fig.5.7 illustrates the microstructures whose mechanical properties are studied in the latter parts of the work. Microstructure 1 in Fig.5.7a exhibits a traditional uniform γ/γ' distribution; it was developed by ageing at 1100ºC for 6 hours, followed by air- cooling. Microstructures 2 and 3 were developed by ageing at 1120ºC for 24 hours and 1160ºC for 4 hours respectively, followed by air-cooling. Microstructures 2 and 3 were developed to be deliberately bimodal. The heat treatment conditions of SCA425+ investigated here are summarised in Table 5.3.

**Table 5.2. Summary of stereological data for the distribution of the γ' phase after different first ageing heat treatments. Note that the area constants $A$ below are to calibrate the height of each normal distribution (which is commonly number of particle $N$) to number of particles per unit area ($N$ μm$^{-2}$).**

| Temp. (ºC) | Time (h) | Area constant, $A$ | Average diameter of γ' (μm) | Standard deviation (μm) | $R^2$ |
|---|---|---|---|---|---|
| 1080 | 24 | 0.1511 | 0.5450 | 0.1122 | 0.89 |
| 1100 | 4 | 0.5085 | 0.3405 | 0.0726 | 0.82 |
| | 6 | 0.7107† | 0.3944 | 0.0829 | 0.82 |
| | 24 | 0.1866 | 0.5708 | 0.1372 | 0.88 |
| | 48 | 0.1088 | 0.7171 | 0.1676 | 0.92 |
| 1120 | 8 | 0.2293 | 0.4892 | 0.1128 | 0.86 |
| | 24 | 0.0996 | 0.6635 | 0.1626 | 0.90 |
| 1160 | 4 | 0.1357 | 0.6075 | 0.1764 | 0.91 |

**† different etching condition applied.**

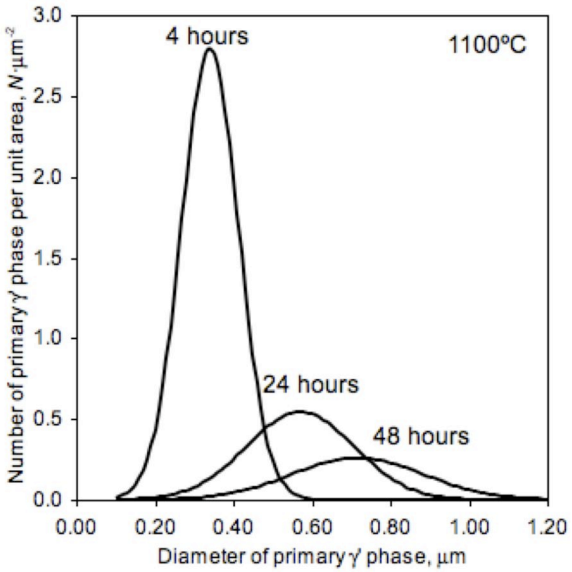


**Fig.5.6 Particle size distribution curves after ageing for 4, 24 and 48 hours at 1100ºC.**

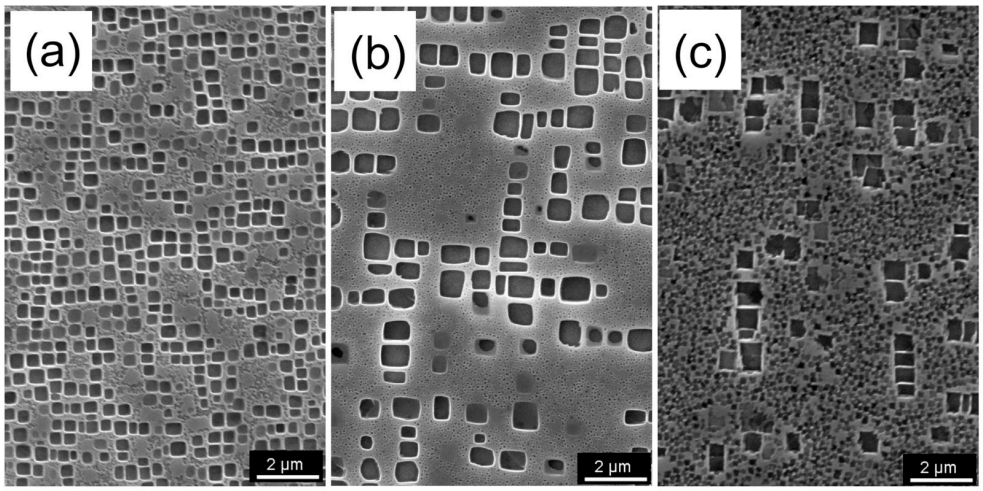


**Fig.5.7 Scanning electron micrographs of SCA425+ with different first ageing conditions of (a) 1100ºC 6 hours, (b) 1120ºC 24 hours, and (c) 1160ºC 4 hours, respectively. These are denoted (a): Microstructure 1, (b): Microstructure 2, and (c): Microstructure 3 in this work.**

**Table 5.3 Heat treatment conditions used for the SCA425+ superalloy.**
**(AC: Air cooling).**

| | Solution treatment | First ageing | Second ageing |
|---|---|---|---|
| Microstructure1 | 1280ºC 1hr -> 1300ºC 5hrs AC | 1100ºC 6hrs AC | 850ºC 20hrs AC |
| Microstructure2 | | 1120ºC 24hrs AC | |
| Microstructure3 | | 1160ºC 4hrs AC | |

### 5.2.3 Creep Behaviour

The creep curves measured for the three distinct heat treatment conditions are given in Fig. 5.8. It was found that Microstructure 1 (uniform) performed the best for each of the four creep conditions chosen. The associated creep strain rate vs. strain curves are given in Fig. 5.9; with regard to the minimum creep rate exhibited, one finds that (i) this is generally lower for Microstructure 1 and (ii) the effect of microstructural condition is greater at the lower temperature/higher stress regime. The creep results are summarised using a Larson-Miller plot (LMP) in Fig.5.10, using both the time to 1% strain but also the time to rupture. Once again, the time to 1% creep falls in the order: Microstructure 1 > Microstructure 2 > Microstructure 3. One can see that, whilst the creep performance falls short of the Re-containing alloy CMSX-4, the creep rupture performance approaches that of IN792 which was one of the goals of the SCA425+ alloy development project.

Fig.5.11 illustrates the microstructure of SCA425+ after creep rupture. No topologically closed packed (TCP) phases were observed, indicating that – despite the significant alloying with respect to Cr – the alloy is stable. No evidence of γ' cutting was observed, and γ' rafting was very limited being restricted to Microstructure 1 crept at 850ºC, see Fig.5.12. These findings were further confirmed by TEM. Fig.5.13 shows micrographs after creep rupture test at (a) 850ºC/275MPa and (b) 750ºC/520MPa for Microstructure 3, respectively. At 850ºC/275MPa, no dislocation activity was found within the γ' precipitates, see Fig.5.13a. Very high dislocation density at primary γ'/matrix interfaces was observed; in other words, dislocations at secondary γ'/matrix interface were rather dispersed. Only at the lowest temperature and highest stress condition of 750ºC/520MPa were any single dislocations seen within the primary γ'.

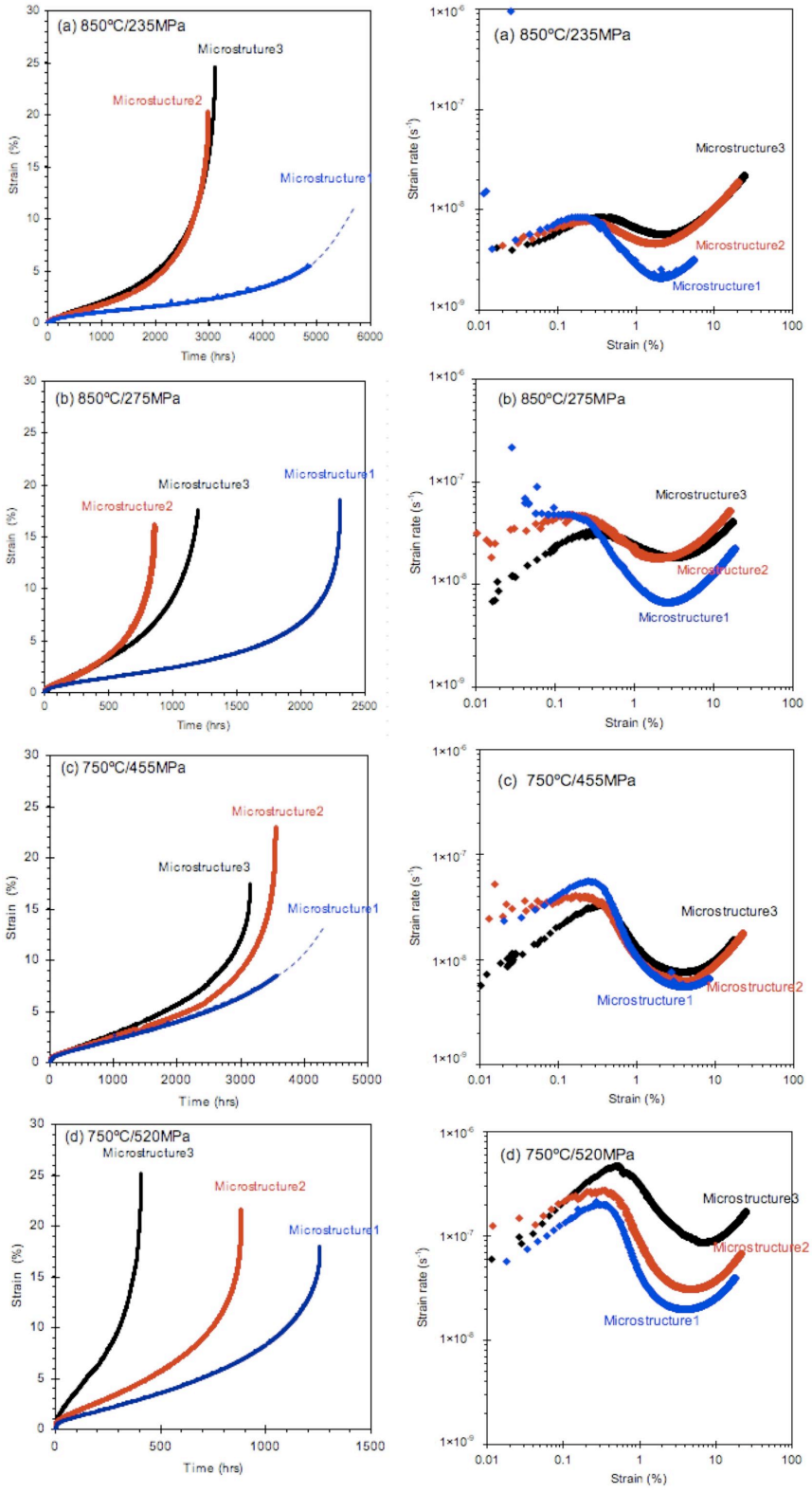


**Fig.5.8 Creep strain vs. times curves for SCA425+ at different creep conditions. (Left side)**
**Fig.5.9 Creep strain rate vs. strain curves of SCA425+ at different creep conditions. (Right side)**

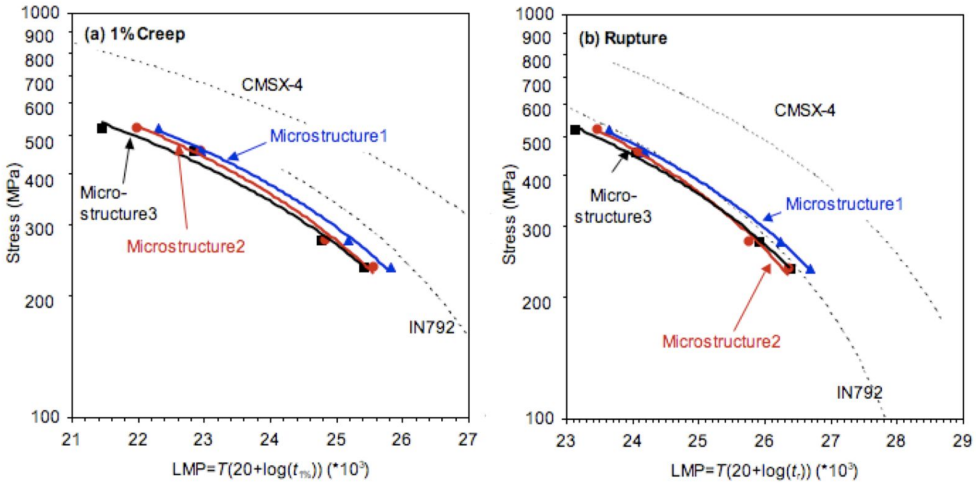


**Fig.5.10 Larson-Miller plots of SCA425+ with three different microstructures for (a) 1% creep times and (b) creep rupture times. For comparison the location of data for the IN792 polycrystalline alloy and the CMSX-4 single crystal superalloy are given.**

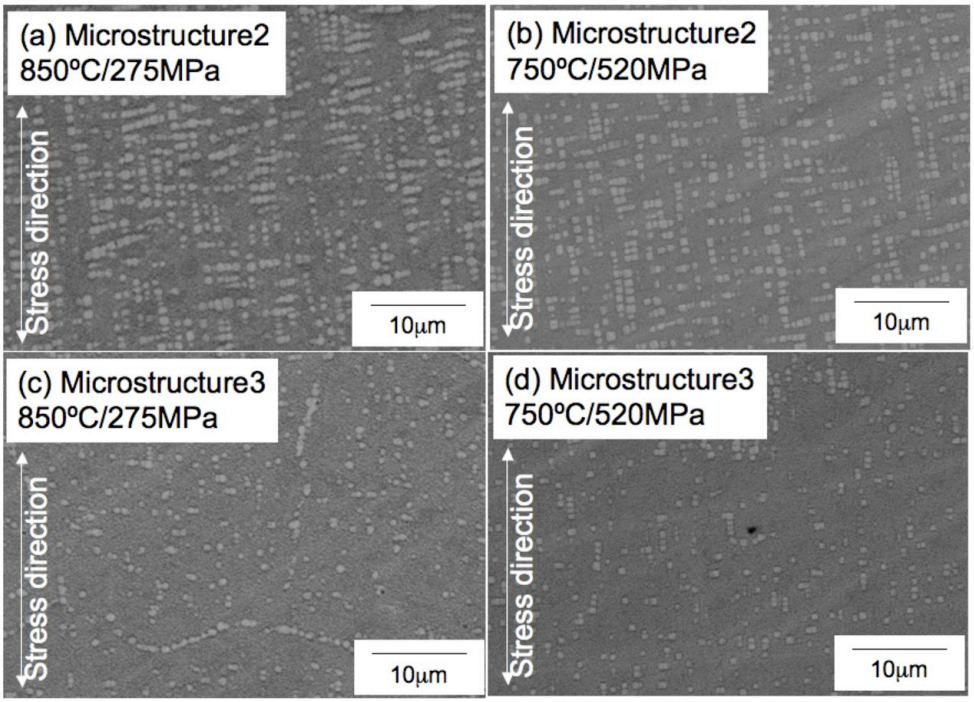


**Fig.5.11 Micrographs of SCA425+ after creep rupture testing at 850ºC/275MPa and 750ºC/520MPa. Note that all images were obtained at a distance 10 mm away from the rupture surface.**

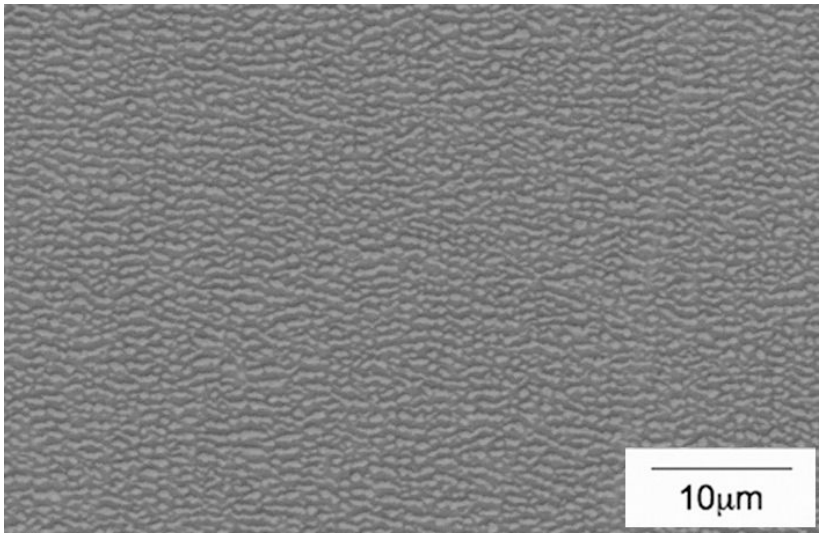


**Fig.5.12 SEM micrographs of Microstructure 1 after 850ºC/275MPa. A degree of rafting is present.**

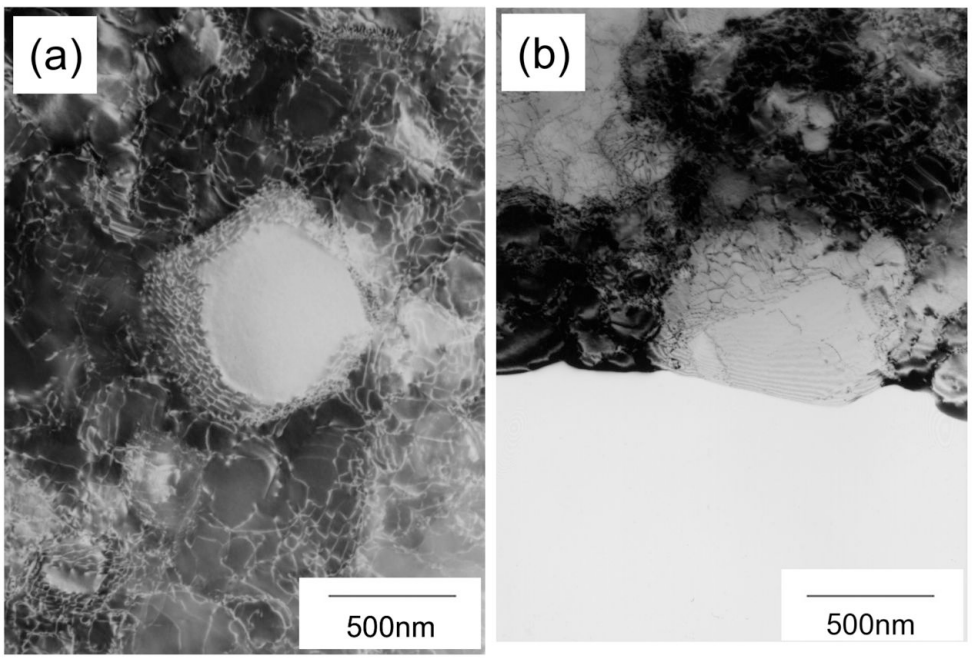


**Fig.5.13 TEM micrographs of SCA425+ (Microstructure 3) after creep rupture testing at (a) 850ºC/275MPa and (b)750ºC/520MPa.**

## 5.2.4 Thermomechanical Fatigue Behaviour

Although the creep performance of the new alloy is somewhat inferior to that of CMSX-4, the performance in TMF has been found to approach that of this alloy; this is significant and has ramifications for the gas turbine users. In Fig.5.14 the relationship between the mechanical strain range used during the OP-TMF tests and the number of cycles to failure are given. Also given are data from the literature [55, 60, 133] for CMSX-4 and IN792 acquired using identical testing methods. A number of important points emerge. First, consistent with its lower elastic modulus along the [001] testing direction, the TMF performance of SCA425+ is superior to that of the polycrystalline alloy IN792. Second, it is apparent that the TMF life is influenced by the microstructural state induced by heat treatment. In particular, bimodal microstructures are found to be superior to the uniform one; Microstructure 2 exhibits the best TMF performance with Microstructure 1 – best in creep – displaying the worst.

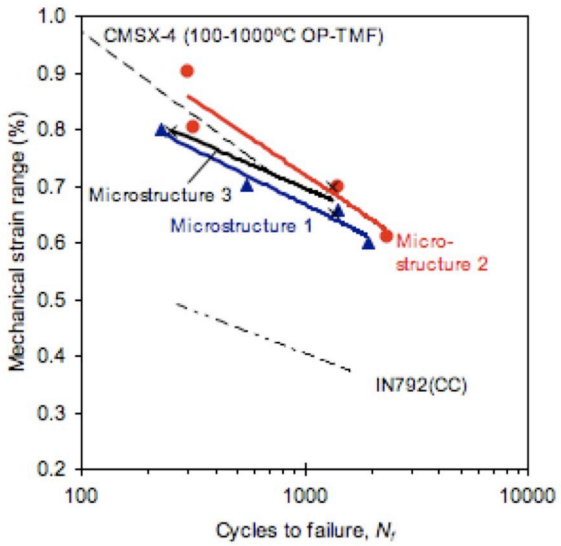


**Fig.5.14 TMF data for SCA425+, in which the number of cycles to failure is plotted against the mechanical strain range employed. Note the superior performance of the second microstructural condition.**

Hysteresis loop changes its shape during the early stage of testing, and reaches to the equilibrium condition [49] due to the balance between generation/annihilation of dislocation (stabilized). Fig.5.15 illustrates stabilized hysteresis loops at mid-lives for the three microstructures, in this case for the mechanical strain range of 0.8%. Note that the minimum stress in the stabilized loops is lowest for Microstructure 3 and greatest for Microstructure 1, in agreement with the static creep result which found that Microstructure 3 creeps the fastest and Microstructure 1 the slowest. This point is discussed further in section 5.3.

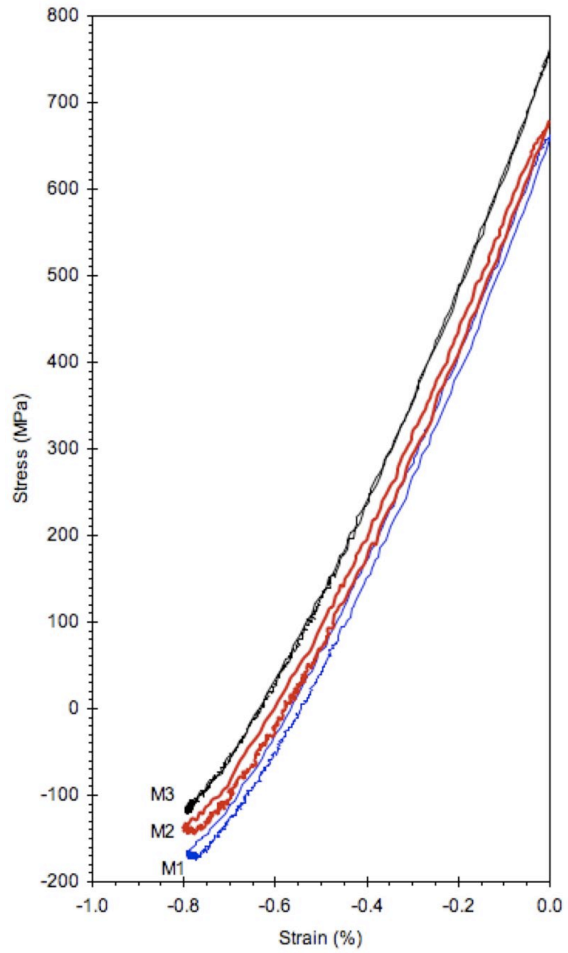


**Fig.5.15 Stabilised hysteresis loop at mid-life for SCA425+ with three different microstructures. (M1: Microstructure1, M2: Microstructure2 and M3: Microstructure3)**

Fig.5.16 illustrates the microstructure of SCA425+ after TMF testing. The fracture surface had a tendency to lie about 45º from the direction of applied stress. Furthermore, across the cross-section, significant numbers of slip-bands [134, 135] were observed with subsequent crack propagation occurring along these. Occasionally, recrystallisation was observed along the slip-band as well, see Fig.5.17. Additionally, there was strong evidence within the slip-band, see Fig.5.18, of the γ' rafts (orientated along the stress axis due to the compressive stress generated and consistent with the negative misfit determined in section 5.2.1) being sheared.

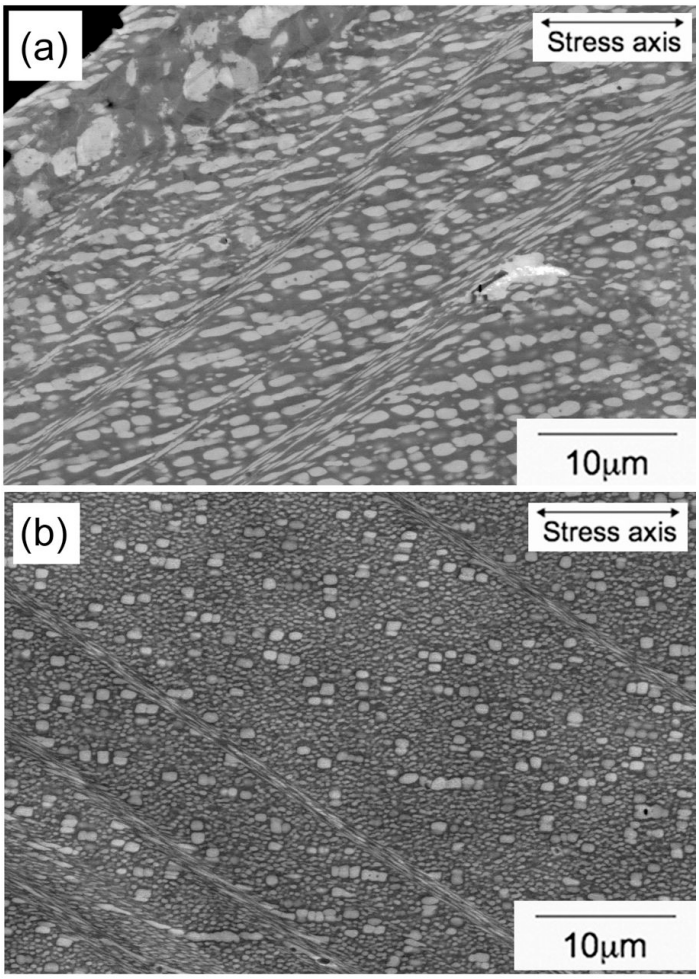


**Fig.5.16 Micrographs of SCA425+ after TMF testing: (a) Microstructure 2 with $\Delta\varepsilon_{mech}$ = 0.7%; (b) Microstructure 3 with $\Delta\varepsilon_{mech}$ = 0.8%. The stress axis is holizontal direction in both cases.**

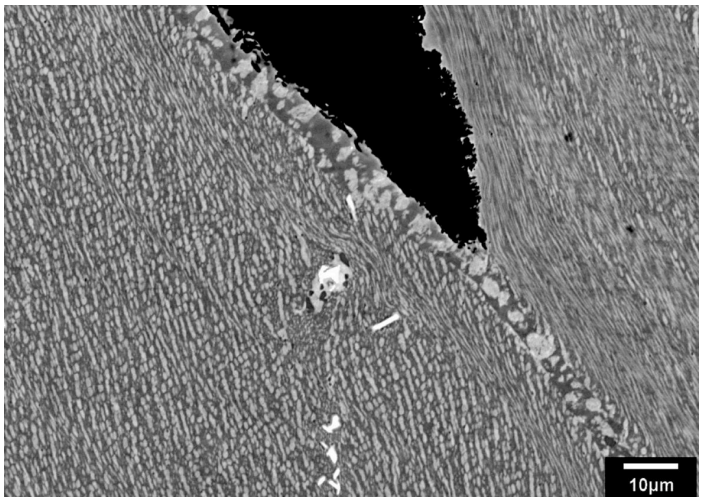


**Fig.5.17 TMF crack propagation along the recrystallised slip-band observed in Microstructure 2 with $\Delta\varepsilon_{mech}$ = 0.7%. Stress axis in vertical direction.**

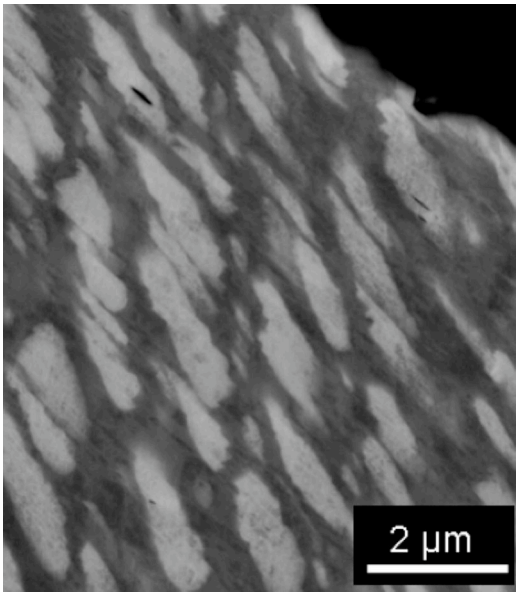


**Fig.5.18 Sheared γ/γ' observed in Microstructure 2 after TMF testing with $\Delta\varepsilon_{mech}$ = 0.7%. Stress axis in vertical direction.**

Finally, Fig.5.19 illustrates TEM micrographs of SCA425+ after TMF testing for Microstructure 2. Necessarily due to the specimen preparation technique employed, the TEM specimens were taken somewhat away from the fracture surfaces. No significant micro-mechanical deformation was observed, with the dislocation activity being much less than in the case of the crept microstructures. These observations suggest that TMF damage is more highly localised than for creep, and limited to the proximity of the fracture surface. Also, the secondary γ' has dissolved during TMF testing, see Fig.5.19.

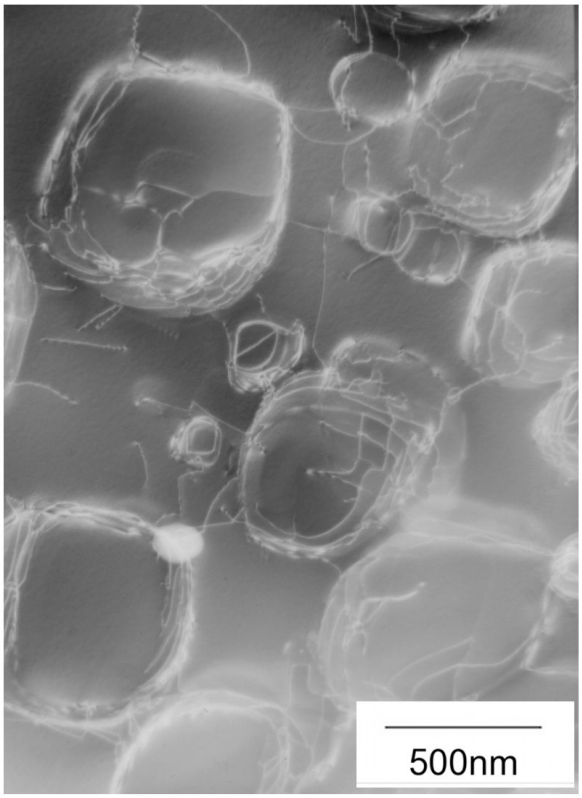


**Fig.5.19 TEM micrographs of SCA425+ after TMF testing in Microstructure 2 with $\Delta\varepsilon_{mech}$ = 0.7%.**

## 5.3 Discussion - On The Damage Mechanisms Occurring in TMF

The TMF results presented here are interesting because the damage mechanisms found are very different from those reported in the literature so far. Significant research has been reported on the TMF of Re-containing single crystal superalloys such as CMSX-4 [55, 136] and TMS-82+ [58]; in these papers, the prevalent damage mechanism during TMF is mechanical twinning. Instead, in SCA425+ – which does not have the benefit of the significant creep resistance of CMSX-4 – the dominant mode of damage is localised slip band formation, with associated γ' shearing in these bands. One should attempt to rationalise the factors influencing these differences in the deformation modes. Generally, it is known that the transition from slip to twinning occurs when the localised stress exceeds a threshold stress [137]; in this case it can be expected that the gamma prime precipitates are penetrated. Moreover, careful work [58] has revealed that it is the compressive stress when the number of accumulated TMF cycles is low which activates the twinning mode; our results support this view. In Fig.5.20 the hysteresis loops of the first TMF cycles observed in SCA425+ and CMSX-4 [55, 60] are compared, for the mechanical strain range of 0.8%. For SCA425+ one can see that the highest stress is ~550MPa; this is compressive in nature and occurs at ~860ºC during the heating cycle, i.e. ~40ºC below the maximum temperature to which the material is subjected. Note that CMSX-4 (which exhibits twinning rather than slip band formation) experiences a larger maximum compressive stress at a lower temperature, ~830ºC. Thus, it seems possible that the root cause of slip band formation in SCA425+ (and therefore a possible contribution to a TMF resistance which almost matches that of CMSX-4) is its rather moderate high temperature compressive creep strength.

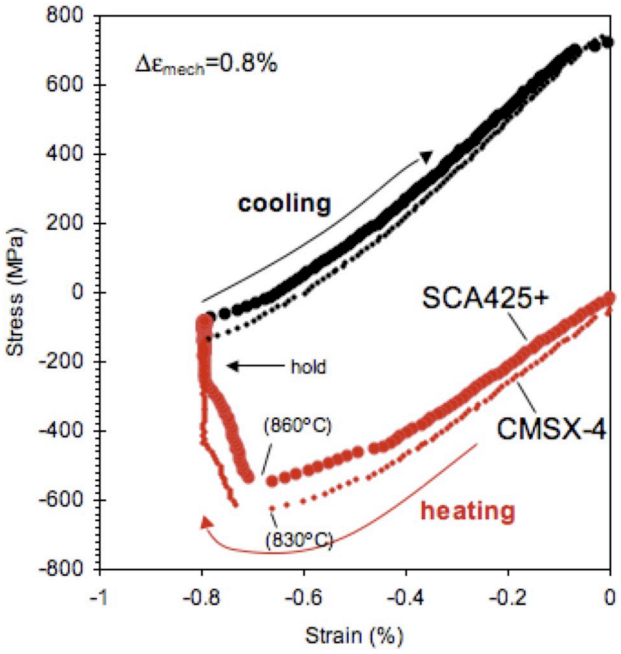


**Fig.5.20 Hysteresis loop from the first cycle of OP-TMF testing on SCA425+ with Microstructure 1 and CMSX-4 with mechanical strain range of 0.8%. Maximum compressive stresses of 550MPa (SCA425+) and 625MPa (CMSX-4) are identified at ~860ºC and ~830ºC respectively.**

The influence of different γ' morphologies on TMF performance should also be commented upon. The work here indicates that the resistance to shearing of the primary γ' particles is important in determining TMF resistance. Particle hardening theories [3, 46] indicate that the critical resolved shear stress for particle shearing is proportional to $\sqrt{(rf)}$ where $r$ is radius of primary γ', and $f$ is the volume fraction of γ', respectively. This enables a contour plot of critical resolved shear stress to be identified on which the fraction $f$ of the γ' phase is plotted against its particle radius $r$, see Fig.5.21. Provided that secondary γ' dissolved during TMF testing, the primary γ' size is solely plotted against the total volume fraction at highest temperature during TMF testing (42% at 950ºC).

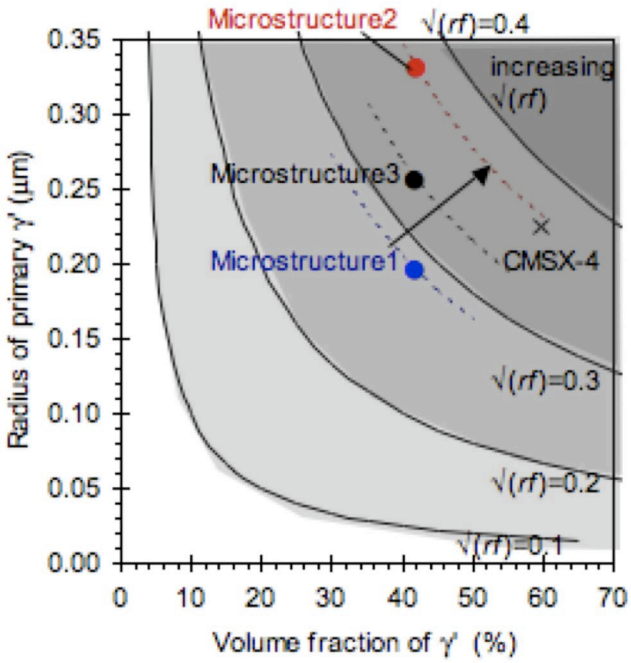


**Fig.5.21 Isocontour plot for the particle shearing mechanism in SCA425+. Reference data of CMSX-4 is also given. Note that the isocontours of $\sqrt{(rf)}$ are given as solid lines.**

The highest strength is expected in the top right corner of the diagram when both *f* and *r* are large. Also plotted are the locations of the Microstructures 1-3 studied here but also the values for $\sqrt{(rf)}$ reported for CMSX-4 [104, 138]. Note that $\sqrt{(rf)}$ is higher towards the top right of this diagram. One can see that Fig. 4.21 helps to rationalise the superior TMF performance of Microstructure 2 and the relatively poorer performance of Microstructure 1. Therefore it seems likely that the γ' shearing resistance, *i.e.* $\sqrt{(rf)}$, is a major factor influencing TMF resistance. Providing that the microtwinning mechanism prevalent in CMSX-4 can be avoided, this suggests that increasing the primary γ' size is beneficial.

Finally, the importance of γ' particle shearing in the mechanism of TMF explains why the optimum microstructure condition for creep was not the one that was optimum for TMF. At the creep conditions studied here, little or no γ' shearing occurs as confirmed by the TEM studies; dislocation activity is restricted to the matrix phase. Under these circumstances creep deformation is best limited by a uniform and regular precipitate structure [3, 32]. In fact, creep relaxation is occurring during the TMF testing as can be seen at the hot-end of the first TMF cycle for Microstructure 1, 2 and 3, see Fig.5.22. One can see that Microstructure 1 exhibits superior creep relaxation behaviour at both mechanical strain range conditions considered. The creep relaxation differences are small (<50MPa), but the TMF data are consistent with the static creep results which indicate that the Microstructure 1 shows slowest creep deformation to 1% creep strain.

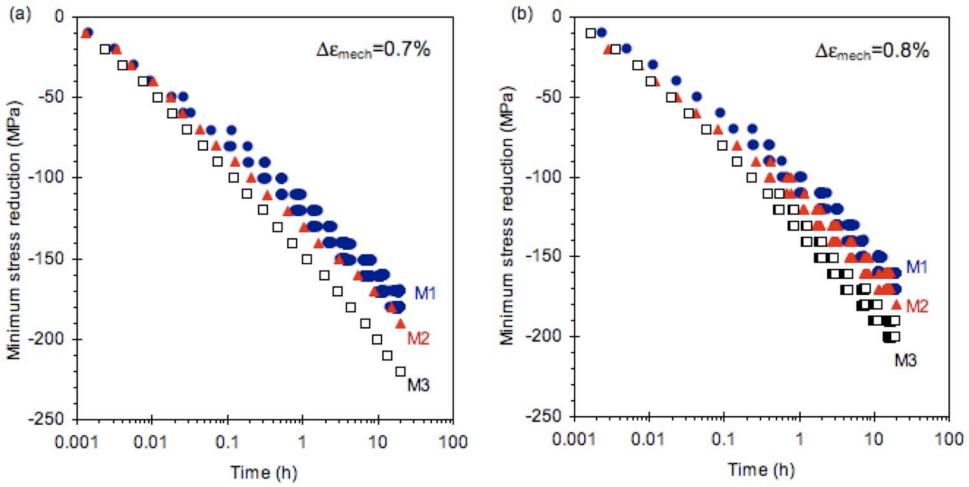


**Fig.5.22 Creep relaxation data observed in Microstructure 1, 2 and 3 during the holding period in the first cycle of TMF testing. (a) $\Delta\varepsilon_{mech}$=0.7% and (b) $\Delta\varepsilon_{mech}$=0.8%.**

## 5.4 On The Factors Controlling TMF Resistance in Single Crystal Superalloys

This work provides important insights into the factors controlling the TMF performance of single crystal superalloys, which are not well understood at present. These can be summarised as follows. A first point is that the best performance in TMF and creep do not necessarily go hand in hand; thus for resistance to TMF an alloy does not need the very best creep resistance. Thus it has been demonstrated that a Re-free alloy (SCA425+) can perform just as well in TMF as a Re-containing one (CMSX-4) despite the creep resistance being markedly inferior.

A second point relates to the difference in damage modes which are prevalent. In SCA425+, one sees slip bands and then recrystallisation within these bands followed by fatigue cracking along them. Some shearing occurs of the rafts of γ', which for out-of-phase TMF and a negatively misfitting alloy are elongated along the direction of applied load. In CMSX-4 on the other hand, deformation is more localised and the micro-twinning mode is more prevalent [55, 60]. Recrystallisation and precipitation of topologically close-packed phases (TCPs) along the twins can occur, and this is again the preferred direction of crack propagation. Once again, these differences underline the important influence of alloy chemistry on TMF resistance.

A third point relates to the optimum microstructure for TMF. At least for the SCA425+-type compositions which are free of Re, optimum TMF resistance is conferred when the resistance to γ' shearing is greatest. Consistent with a critical resolved shear stress proportional to $\sqrt{(rf)}$ where $r$ is radius of primary γ' and $f$ is the volume fraction of γ' respectively, TMF performance is improved at large $r$ and presumably if $f$ is increased,

although this last point is not tested here. Whether this is also true for the Re-containing alloys which are prone to microtwinning needs to be tested *via* further experimentation, and is the subject of ongoing research.

In the case of SCA425+, its suitability for gas turbine applications rests on – in conjunction with its superior environmental performance [119, 127] – its rather good TMF performance which in turn is conferred by its resistance to precipitate shearing. It has a wide solutioning window and can be heat treated readily to yield a microstructure which confers the necessary mechanical performance.

## 5.5 Conclusions

The following conclusions can be drawn from this work;

(1) A prototype high Cr-containing nickel-based single crystal superalloy SCA425+ has been assessed to determine the factors influencing the mechanical performance in creep and out-of-phase (OP) thermomechanical fatigue (TMF).

(2) Neutron diffraction studies confirmed that SCA425+ has a gamma prime fraction of approx 42% at 950ºC, increasing to approx 56% at 800ºC. The lattice misfit is small, ranging from -0.09% at 800ºC to -0.20% at 1000ºC.

(3) The TMF response of the new alloy SCA425+ is comparable to that of the commonly employed single crystal superalloy CMSX-4; this is despite the fact that the constant load (static) creep performance is inferior to it and in fact more broadly consistent with the polycrystalline superalloy IN792.

(4) The factors controlling TMF resistance are distinct from those determining creep; in particular for best TMF performance, resistance to dislocation shearing of the gamma prime phase is required – consistent with a large flow stress and ultimate tensile strength. On the other hand – at least for low stresses – creep resistance is determined by dislocation activity in the gamma matrix phase.

(5) The influence of primary gamma prime size was investigated. The TMF resistance increases with increasing primary gamma prime size; in creep, the finer primary gamma prime microstructure gave better performance particularly in the high temperature regime due to rafting.

(6) Consistent with the lower elastic moduli, the TMF performance of SCA425+ is superior to that of the polycrystalline alloy IN792 when the mechanical strain range is considered. The data for the mechanical strain range is sensitive to the microstructual state, with the data indicating that a bimodal microstructure with large gamma prime particles performs best.

# Chapter 6. On the Oxidation Behaviour of Nickel-Based Superalloys for High Temperature Applications

## 6.1 Introduction

New grades of single crystal nickel-based superalloy are needed for critical components in electricity-generating industrial gas turbines [3, 139]. For such applications, existing alloys – most of which are used in aeroengine applications – do not possess sufficient resistance to environmental degradation at the temperature of operation [97, 140], which can be as high as 1000ºC or beyond. At these conditions, oxidation is a possibility which should be anticipated prior to use of any new alloy in its operating environment. Ideally, one would like to have predictive methods which would allow estimates to be made about the anticipated oxidation performance of any new alloy system; unfortunately, this goal has yet to be achieved.

Recently, the authors have studied the oxidation behaviour of a novel single-crystal superalloy which possesses significantly greater Cr content than found in existing alloys [141]. Processing of it into single crystal form has been successfully demonstrated [119],

and the oxidation resistance has been shown to be very good – in fact better than alloys such as IN792, IN939 and IN738 which are commonly used for industrial gas applications, see Fig.6.1. The superior oxidation resistance would appear to be due to the scale which consists of an outer layer of $Cr_2O_3$, and a sub-scale of $Al_2O_3$ which lies in contact with bare metal. Minor additions of Si [83] have been found to improve the oxidation resistance, if added in the correct quantities, with the $Al_2O_3$ sub-scale becoming more planar and compact [142].

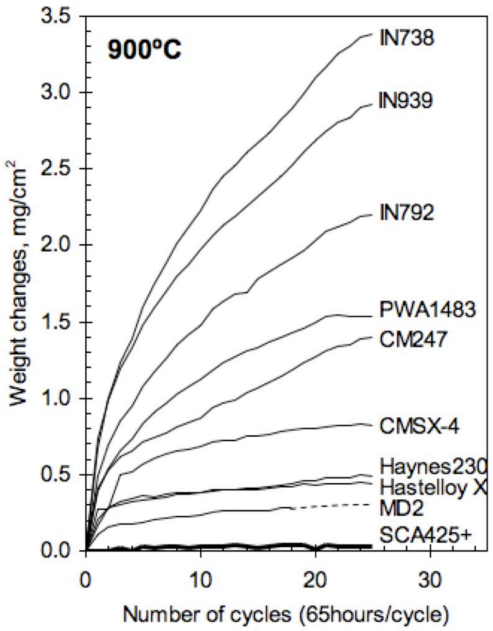


**Fig.6.1 Comparison of cyclic oxidation resistance of SCA425+ with other alloys used for industrial gas turbine (IGT) applications, at 900°C and with cycle time of 65 hours.**

In rationalising the oxidation performance of the new alloy, the authors have considered in quantitative terms (i) the driving force for alumina formation and its dependence on the activity of aluminium in the alloy and (ii) the transport of $O^{2-}$ ions through the alumina, and its perturbation caused by uptake of alloying elements from the bare alloy [8, 12]. Whilst there exist a number of assumptions which need to be further tested, the model developed has been shown already to have some predictive power [119]. One prediction from it is that oxidation should be improved by substitution of W by Re [119], which is

contradicts existing thinking (e.g. [143]) that Re-containing superalloys (such as third- and fourth-generation single crystal superalloys) are necessarily oxidation prone. Here, we set out to test this prediction.

## 6.2 Background Theory

Since the arguments which follow relate to the kinetics of alumina formation, it is appropriate here to consider accepted oxidation theory and thus Wagner's model for parabolic oxidation [8, 12]. The number of molecules of $Al_2O_3$ formed per square cm per second is given by eq.1.10 (section 1.3.2). The parabolic oxidation rate $k_t$ (molecules $cm^{-1}$ $sec^{-1}$) can further be estimated by eq.1.11 [12]. In the case of alumina which is an n-type conductor ($t_{el} \approx 1$, $t_a >> t_c$) [20], one has eq.3.7 (section 3.2) [119]. Furthermore, by accounting for the so-called impurities effect (also known as Wagner-Hauffe theory [105]), eq.3.7 can be re-written as [119]

$$k_t \propto \left( -\frac{D_{V^{\text{eff}}}}{z_c^2 kT} \right) \cdot \sum_i \left( z_i - z_{\text{Al}} \right) c_i^{\gamma} \cdot \Delta G_f \tag{6.1}$$

where $D_{V^{\text{eff}}}$ represents the effective diffusion coefficient of dominant defects, and the summation term represents its concentration – sometimes referred to as the total effective valence $\text{Val}_t^{\text{eff}}$, see eq.3.17 (section 3.4.2). Note that the effect on the impurities factor of grain boundary diffusion [20, 106] or alumina phase transformation [15, 20, 22] are not considered, which are major assumptions. Furthermore, $\Delta G_f$ can be expanded consistent with the Van't Hoff isotherm [8] according to eq.1.1 (section 1.1). Inspired by eq.6.1, the concept of an oxidation diagram has been proposed [119] in which the total effective valence $\text{Val}_t^{\text{eff}}$ and Gibbs free energy $\Delta G_f$ for alumina formation are plotted on the x- and y- axes, see Fig.6.2 for an example. At constant temperature, alloys which form $Al_2O_3$ readily are expected to lie towards the bottom left of it (large negative $\Delta G_f$, and $\text{Val}_t^{\text{eff}}$), see Fig.6.2a. Isocontours of constant parabolic rate constant can be plotted on the diagram, with a critical value distinguishing continuous alumina-forming superalloys (solid symbols) and discontinuous alumina-former (open symbols) in Fig.6.2b. Since any given chemical

composition of a superalloy plots to a point on the oxidation diagram, the oxidation resistance can be judged in principle from its point relative to the critical isocontour. This idea is used in the present work.

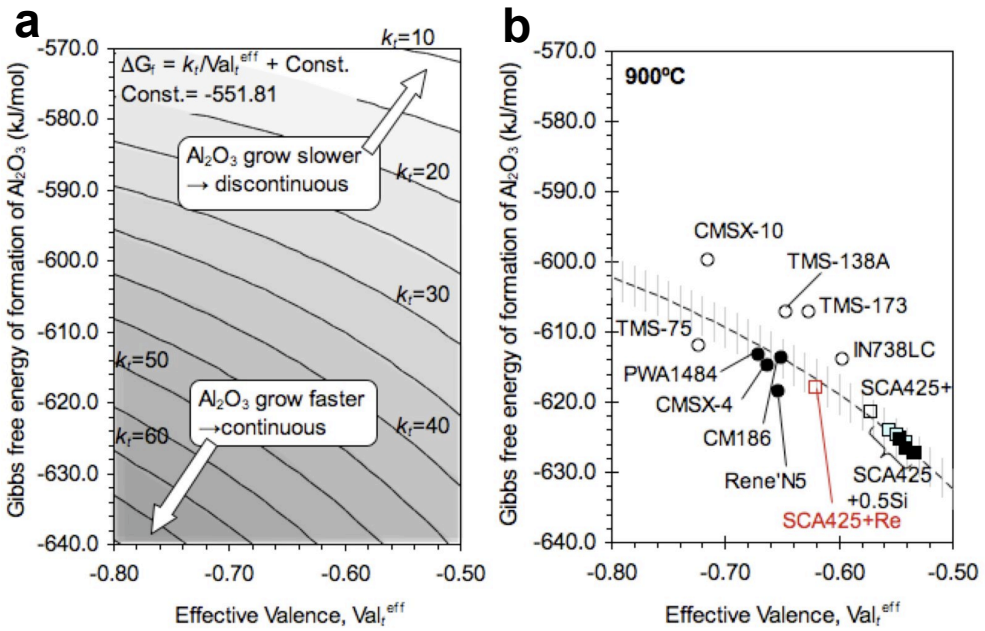


**Fig.6.2 (a) Illustration of the oxidation diagram concept, and (b) oxidation diagrams of nickel based superalloys at 900ºC, modified from [119]. Note that continuous alumina forming alloys (solid symbol) lie towards the bottom left of the diagram and are distinct from and those in which alumina formation is discontinuous. The SCA425+Re alloy considered here is predicted to perform better in oxidation.**

## 6.3 Experimental Details

The nickel-based single crystal superalloy SCA425+ [119, 144] was used as the base alloy. SCA425+ contains 4wt.% W to aid creep strengthening [145], but our calculations have indicated that W is detrimental to the oxidation resistance. In this study, 0.65 at.% of the total content of W has been substituted by the equivalent quantity of Re – the new alloy being denoted SCA425+Re. According to the oxidation diagram proposed, SCA425+Re kinetics of alumina formation are then enhanced, see Fig.6.2. The nominal compositions of the two alloys investigated are given in Table 6.1.

**Table 6.1 Nominal compositions (wt.%, Ni-bal) of superalloys investigated.**

| | Co | Cr | Mo | W | Al | Ta | Hf | Re |
|---|---|---|---|---|---|---|---|---|
| SCA425+ | 5.0 | 15.5 | 1.0 | 4.0 | 4.55 | 8.0 | 0.1 | - |
| SCA425+Re | 5.0 | 15.5 | 1.0 | 2.0 | 4.55 | 8.0 | 0.1 | 2.0 |

An industrial-scale investment casting facility at the University of Birmingham was used to prepare single crystal castings in the form of 15 mm diameter rods of length 150 mm. Typically, three rods were cast in each run with a withdrawal speed of ~200 mm per hour; the anticipated temperature gradient was 75ºC/cm. Ceramic moulds were prepared from alumina, silica and zircon in the usual way; the final mould thickness was ~6 mm. The casting stock was melted by Ross & Catherall in Sheffield, UK to industry-leading standards. The solution treatment chosen was 1280ºC/5 hours, followed by air-cooling. The first and second ageing treatments were 1100°C/6 hours and 850°C/20 hours followed by air-cooling, respectively. Fig.6.3 illustrates the microstructure of fully heat-treated (a) SCA425+ and (b) SCA425+Re, respectively. The average primary γ' particles size in SCA425+ and SCA425+Re were found to be 0.39 and 0.31 μm, respectively.

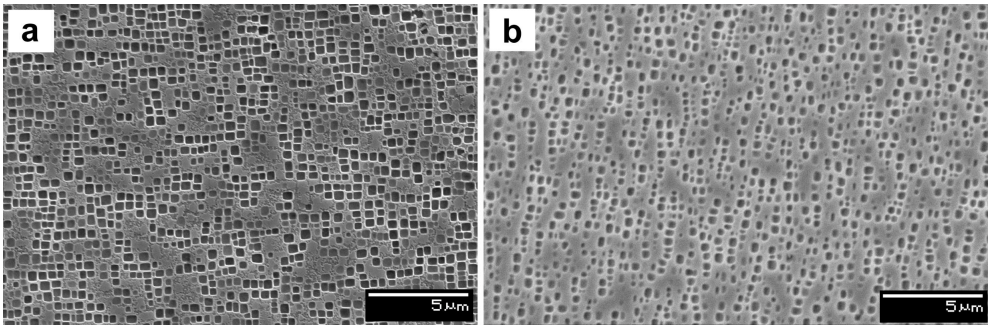


**Fig.6.3 Scanning electron micrographs of (a) SCA425+ and (b) SCA425+Re after heat treatment.**

The oxidation performance of the two alloys was compared in various ways. For thermogravimetric analysis (TGA), 1 cm × 2 cm × 0.5 mm specimens were prepared; surfaces were polished to 1200 grit and cleaned thoroughly in an ultrasonic bath, before analysis in a TGA calibrated to better than ~50 μg. The temperature of 900ºC was used, with tests lasting up to 300 hours. To supplement the TGA analysis, 2 mm thick discs were sliced from the heat-treated castings, polished and cleaned as before, and then placed in an $Al_2O_3$ boat before being exposed isothermally at 900ºC for 100 hours. Cross-sections of these samples were analyzed using back-scattered electron (BSE) in a field emission gunned scanning electron microscope (FEG-SEM) equipped with energy dispersive X-ray spectroscopy (EDX).

## 6.4 Results

The weight changes measured during isothermal oxidation testing at 900ºC are given in Fig. 6.4. A first notable point is that the weight gain accumulated by SCA425+ is significantly altered by the substitution of W by Re. The observed instantaneous parabolic constants are depicted on an Arrhenius plot, together with the values accepted [100] for alumina and chromia formation, see Fig.6.5. It is found that (after an initial rapid transient) the parabolic oxidation rate of SCA425+Re decreases to a value representative of that expected for $Al_2O_3$ (Fig.6.5b); this is not the case for SCA425+ (Fig.6.5a). The stabilised parabolic thickening rate at 900ºC decreased by W -> Re substitution from $4.87\times10^{-13}$ to $8.31\times10^{-14}$ $g^2$ $cm^{-4}$ $sec^{-1}$.

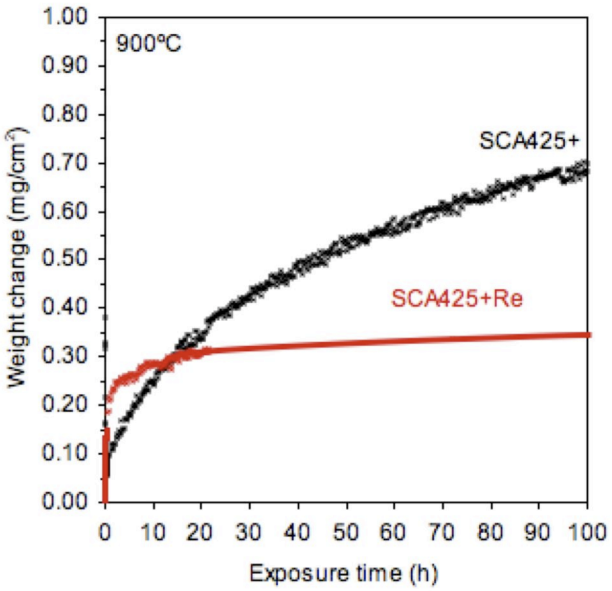


**Fig.6.4 Weight change observed in SCA425+ and SCA425+Re during exposure at a temperature of 900ºC.**

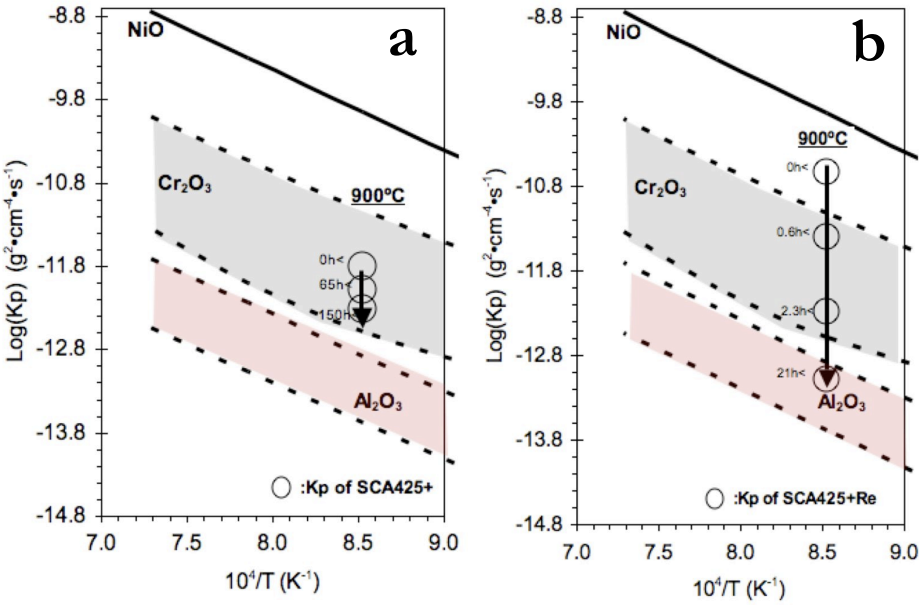


**Fig.6.5 Comparison of the instantaneous parabolic oxidation constants $k_p$ of (a) SCA425+ and (b) SCA425+Re during the exposure at 900°C, with the $k_p$ which are typical for chromia and alumina forming alloys [100].**

Fig.6.6 illustrates the cross-sections of (a) SCA425+ and (b) SCA425+Re after exposure at 900°C for 100 hours, respectively. Backscatter electron images in the SEM indicate the presence of three different oxide species; these are identified as $Cr_2O_3$, $Ta_2O_5$ (or perhaps $NiTa_2O_6$) and $Al_2O_3$. Internal oxidation is prevalent in both SCA425+ and SCA425+Re, see Fig.6.6. Moreover, higher resolution observations confirm the formation of the sub-scale alumina on SCA425+ (Fig.6.7a and 6.7b); for SCA425+Re, there is prevalent alumina internal oxidation but this phase forms a thin layer which is virtually continuous, beneath the external scale, see Fig.6.7c and 6.7d, so that it is on the verge of being protective. Fig. 6.8 shows the chemical mapping result of SCA425+ exposed at 900°C for 100 hours; likewise, that of SCA425+Re is shown in Fig.6.9. Re signals were detected within the Ta oxide. To summarise, although further interpretation is required, the microstructural observations indicate that substitution of W with the equivalent amount of Re promotes the formation of a more planar alumina layer, which is more likely to be protective, consistent with the TGA data.

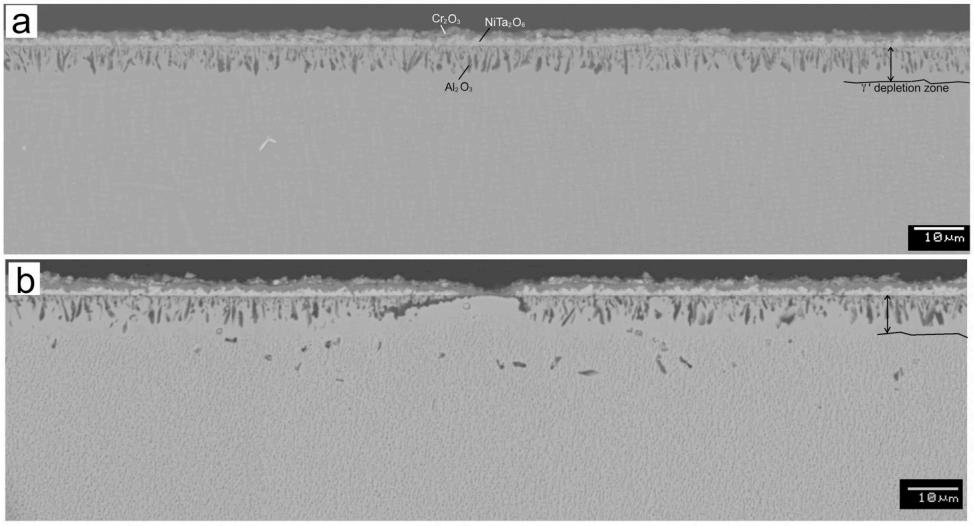


**Fig.6.6 SEM micrographs of (a) SCA425+ and (b) SCA425+Re exposed at 900ºC for 100 hours, respectively. In the SCA425+Re alloy, isolated regions without internal alumina formation can be found.**

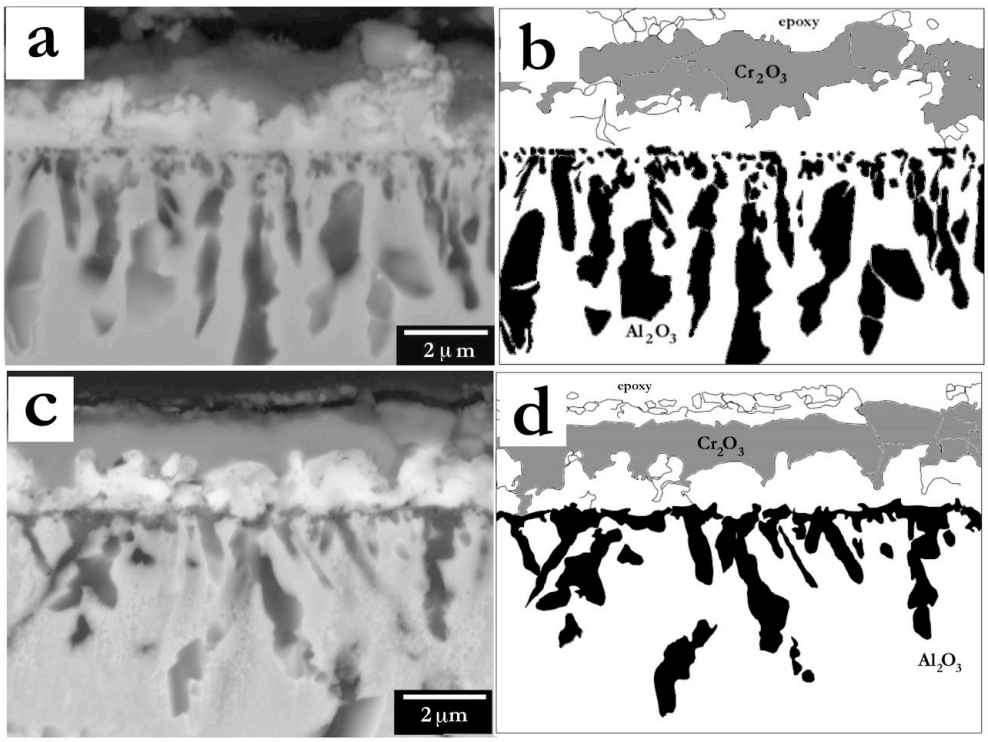


**Fig.6.7 FEG-SEM micrographs of (a) SCA425+ and (c) SCA425+Re exposed at 900ºC for 100 hours, at dendrite core region. Note that (b)&(d) are the sketches of (a)&(c), respectively. For emphasis, the $Al_2O_3$ is shaded black and $Cr_2O_3$ gray in (b)&(d).**

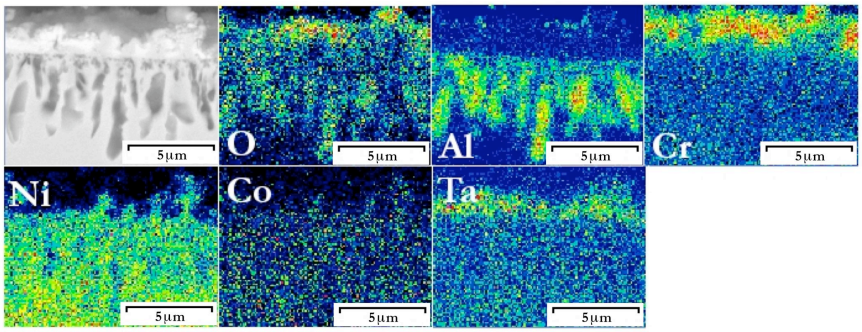


**Fig.6.8 FEG-SEM chemical map of oxide scale on SCA425+ exposed at 900ºC for 100 hours.**

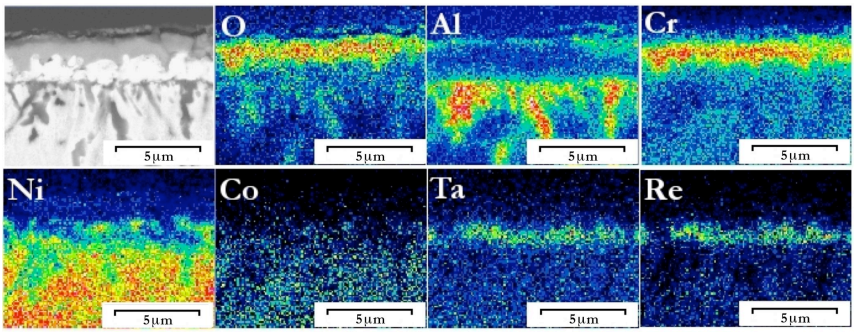


**Fig.6.9 FEG-SEM chemical map of oxide scale SCA425+Re exposed at 900ºC for 100 hours.**

# 6.5 Discussion and Analysis

## 6.5.1 Rationalisation of the Effect of W Substitution by Re

Our findings can be rationalised using the oxidation diagram concept. It can be seen from Fig.6.2 that the W -> Re substitution (taking SCA425+ to SCA425+Re) pushes its position on the diagram towards alloys such as Rene'N5 and CMSX-4 which are known to exhibit excellent oxidation resistance due to their being good alumina formers. Fig.6.10 shows the oxidation diagram with the composition of SCA425+ plotted as the reference. Note that the black area is calculated by increasing the composition of SCA425+ systematically by 1at.% for each of its alloying elements; the red area by decreasing the composition by 1at.%. It can be seen that -1at.% W is highly beneficial for oxidation, and +1at.% Re is neutral. This vector implying the difference in performance indicates that oxidation is improved by changes in the total effective valence, $Val_f^{eff}$ (x-axis), rather than the Gibbs free energy of formation (y-axis).

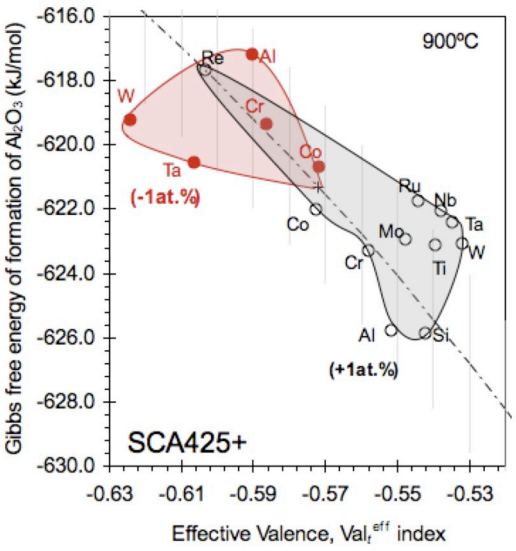


**Fig.6.10 Oxidation diagram plotted relative to the composition of SCA425+. Note that the black area is calculated by *increasing* the composition of SCA425+ by 1at% for each of its alloying elements; the red area by *decreasing* the composition by 1at%. Note that total effective valence is calculated with the matrix composition.**

The effect of W -> Re substitution on the total effective valence should thus be considered in more detail. The phases $WO_3$ and $ReO_2$ (the most stable oxides of W and Re at 900ºC, respectively) have cation valences of 6+ and 4+, respectively; therefore, the substitution of W by a equivalent amount of Re results in a decrease of electron concentration within alumina, i.e. -2e', should Re be taken up by it. However, for electroneutrality reasons [12], this must be compensated for by an increase in the concentration of positive defects such as electron holes, which exacerbate the growth of the n-type alumina scale (Wagner-Haffe theory). The valences of each element *i* in the stable *i*-based oxide are summarised in Table 6.2. The observed effect of W substitution by Re is consistent with this thinking.

**Table 6.2 Valence of cation *i* in *i*-based stable oxide at 900ºC and its effective valence in mother oxide $Al_2O_3$.**

| cation valence, $z_i$ | +2 | +3 | +4 | +5 | +6 |
|---|---|---|---|---|---|
| Stable oxide of element *i* at 900ºC | NiO<br>CoO | $Al_2O_3$<br>$Cr_2O_3$ | $MoO_2$<br>$TiO_2$<br>$ReO_2$<br>$RuO_2$ | $Ta_2O_5$ | $WO_3$ |
| Effective valence in $Al_2O_3$ ($z_{Al} = 3$) | -1 | 0 | +1 | +2 | +3 |
| Oxidation rate for n-type $Al_2O_3$ (Wagner-Hauffe theory) | <-<br>faster | - | -><br>slower | ->-><br>slower | ->->-><br>slower |

## 6.5.2 Prediction of Parabolic Oxidation Rate

To build further on our findings, an additional attempt is now made to rationalise our observations particularly with respect to the wide range of data which are available in the literature. Quantitative estimates of parabolic rate constants might then be made. One needs to be careful with units. After a change to parabolic oxidation rate $k_p$ (units now in $g^2$ $cm^{-4}$ $sec^{-1}$) one has

$$\begin{aligned} k_p^{calc} &= \left(\frac{V_m^{OX}}{N_A}\right)\left(\frac{M_O b \rho_{OX}}{M_{OX}}\right)^2 k_t = \left(\frac{M_O^2 b^2 \rho_{OX}}{N_A M_{OX}}\right) k_t \\ &\propto \left(\frac{M_O^2 b^2 \rho_{OX}}{N_A M_{OX}}\right)\left(-\frac{D_{V^{\text{eff}}}}{z_c^2 kT}\right)\left|\sum_i \left(z_i - z_{\text{Al}}\right) c_i^{\gamma}\right| \cdot \Delta G_f \\ &\propto \left(-\frac{M_O^2 \rho_{OX} D_{V^{\text{eff}}}}{M_{OX} RT}\right)\left|\sum_i \left(z_i - z_{\text{Al}}\right) c_i^{\gamma}\right| \cdot \Delta G_f \end{aligned} \tag{6.2}$$

where $V_m^{OX}$ is the molar volume of the oxide (g $mol^{-1}$), $N_A$ is the Avogadro constant, $M_o$ is the atomic number of oxygen, $b$ is the moles of oxygen in 1 mol of oxide (this can be $b \approx z_i$ if stoichiometric), $\rho_{OX}$ is the density of the oxide and $M_{OX}$ is the molar number of oxide, respectively. Diffusion of dominant defects controls the growth of oxide, so that $D_V^{\text{eff}} \approx D_O$ [12, 146], where $D_O$ is the diffusion rate of the oxide ion.

Fig.6.11a plots the experimentally-observed parabolic oxidation constants $k_p^{\text{exp}}$ ($g^2$ $cm^{-4}$ $sec^{-1}$) reported in the literature [7, 109, 119, 147, 148] (x-axis) plotted against the calculated oxidation rate $k_p^{\text{calc}}$ from eq.6.2 (y-axis). The comparison is made at both 900ºC and 1000ºC. One can see from Fig.6.11a that the observed parabolic oxidation rate decreases when the $k_p^{\text{calc}}$ increases; in other words, there is a negative relationship between these, which is somewhat counter-intuitive. We believe this to be because a large predicted parabolic rate of growth of alumina is in fact consistent with low rates of oxidation, due to

the possibility (for some alloy compositions) of the faster-growing nickel- and chromia-oxides. This point is considered further in the following two sections.

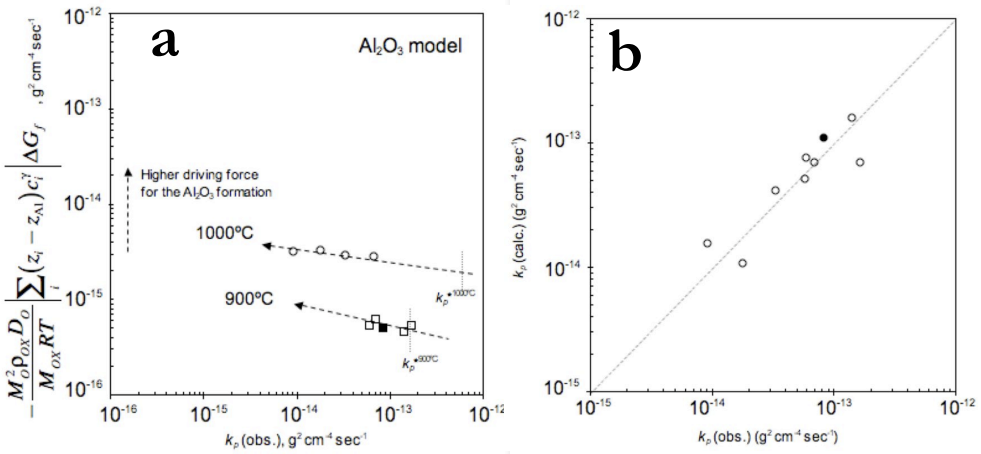


**Fig.6.11 Parabolic oxidation constant of superalloys from literature in x-axis plotted against the calculated oxidation rate $k_p$ in y-axis at 900ºC and 1000ºC. (b) calculated parabolic oxidation constant vs. stabilised parabolic oxidation constant in literature. (For 900ºC: CMSX-4 & PWA-1484 [109], SCA425+0.25Si [119], Rene'N5 (909ºC) [7], for 1000ºC: CMSX-4 [147], DD32 [148], SCA425+ & SCA425+0.25Si [119]). Note that SCA425+Re (this work) are also shown, solid symbols.**

By incorporating this relationship for predictive purposes, one can calculate the parabolic oxidation rate $k_p$ with a linear relationship, according to (for 900ºC): $k_p = -1059.02\ k_p^{calc} + 6.42\times10^{-13}$, and (for 1000ºC): $k_p = -90.61\ k_p^{calc} + 3.02\times10^{-13}$. It should be noted here that the $k_p$ calculated in this way will be used as the calculated parabolic oxidation rate in what follows. Fig.6.11b compares the calculated $k_p$ on the y-axis and against the observed $k_p$ from the literature [7, 109, 119, 147-149] on the x-axis – good agreement between the expression and the experimental data is found. Our studies have confirmed good predictability. For example, the model can predict the weight gains to within an accuracy of $\pm 8\ \mu g \cdot cm^{-2}$ per unit hour; it is more accurate than one based purely upon regression analysis ($\pm 130\ \mu g \cdot cm^{-2}$ , see [150]).

### 6.5.3 Rationalisation of the Oxidation Performance of Nickel-Based Superalloys

Our ideas can be adapted to rationalise the composition-dependence of the oxidation behaviour of the nickel-based superalloys using a rather more powerful type of oxidation diagram. However, as will be seen, the possibility of chromia (rather than alumina) formation also needs to be accounted for. Hence the factors influencing chromia formation are now briefly considered.

The oxidation of pure Cr has been reported to be influenced by the presence of impurities [12]; however, the total effective valence theory used for alumina is not considered to be necessary for the estimation of driving force of $Cr_2O_3$ formation for the following reasons. First, the semiconductivity of $Cr_2O_3$ is known to be p-type, contrasting with $\alpha$-$Al_2O_3$ which is n-type. Thus, $Cr_2O_3$ growth will occur at the gas/oxide interface, contrasting with $Al_2O_3$ at the oxide/matrix interface. Therefore, while $Al_2O_3$ growth will be influenced by impurities inherited from the superalloy substrate on which it grows, this effect will occur to a lesser extent for $Cr_2O_3$ growth. To support this assumption, a recent atom probe topography analysis identified that the concentration of impurities within $Cr_2O_3$ which formed during the early stage of oxidation at 950ºC had no relationship with the matrix composition [142]. Therefore, for simplicity any such effect is ignored in this study. Instead, we concentrate upon accounting for the Gibbs free energy of formation for $Cr_2O_3$ alone, determined using

$$\Delta G_f = \Delta G_0 + RT \ln\left(\frac{1}{a_{\mathrm{Cr}}^{4/3} \cdot P_{\mathrm{O}_2}}\right) \tag{6.3}$$

where $\Delta G_0$ is the standard free energy of oxide formation per 1 mol of oxygen ($Cr_2O_3$: $0.1684T$ - 752.4631 kJ·mol$^{-1}$ [103, 119]) and $a_{Cr}$ is the activity of Cr in the nickel-based superalloy which is subject to oxidation. The influence of alloy composition therefore arises through the activity of Cr alone.

The new oxidation diagram is plotted in Fig.6.12. The temperature is taken to be 900ºC. The calculated parabolic oxidation rate $k_p$ is plotted on the x-axis and Gibbs free energy of formation of $Cr_2O_3$ on the y-axis. On the diagram, the locations of a large number of commercially available nickel-based superalloys are plotted. To aid in the interpretation, a $k_p$ level representative of $Al_2O_3$-controlled kinetics is also marked by a dotted line parallel to the y-axis. Since it has been reported [148] that the 3rd generation nickel-based superalloy DD32 is an alumina former at 900ºC, a critical Gibbs free energy of $Cr_2O_3$ of ~459 kJ mol$^{-1}$ is also plotted for delineation purposes. Some very interesting trends emerge. First (exemplar CMSX-3), second (exemplar Rene'N5), third (exemplar TMS-75) and fourth (exemplar TMS-138A) generation alloys lie towards the bottom right, middle-left, top-left and top-middle, respectively. Fig.6.13 is a schematic interpretation of Fig.6.12. Since the new oxidation diagram can identify protective $Al_2O_3$ forming alloys for any given chemistry, the new diagram is again useful for alloy design purposes. This is expanded upon further in section 6.5.4.

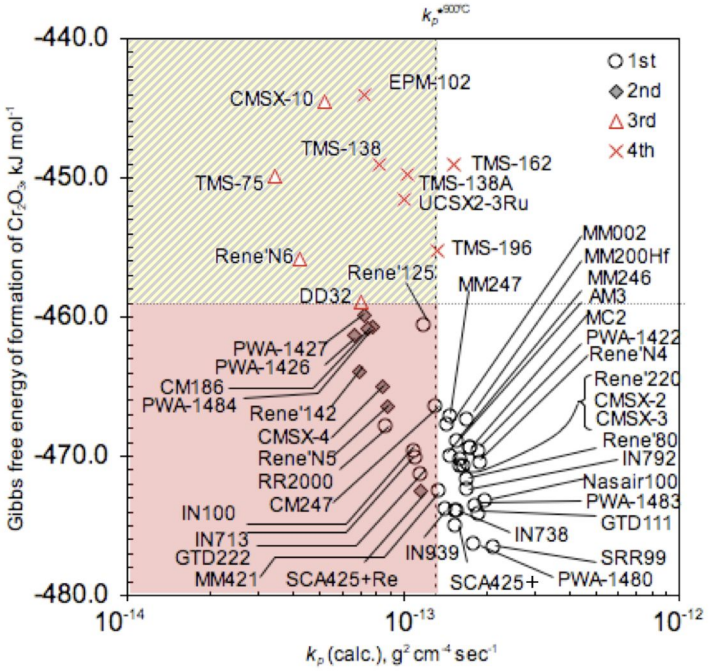


**Fig.6.12 Predicted stabilised parabolic oxidation rate $k_p$ for various generations of nickel-based superalloys at 900ºC, determined using alumina rate-controlling model, plotted on the x-axis, against the Gibbs free energy of formation of chromia in y-axis. The bottom (left hand) red region is the region in which $Al_2O_3$ formation is rate-controlling.**

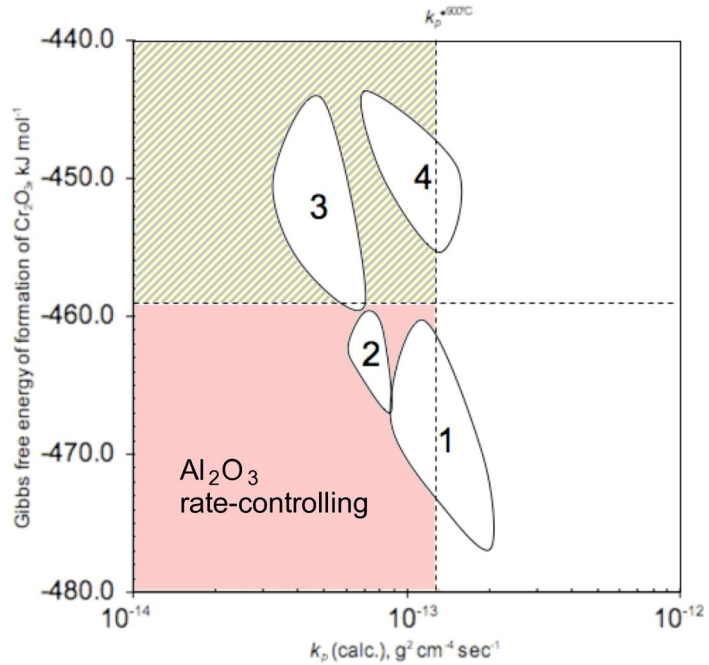


**Fig.6.13 Schematic interpretation of Fig.6.12. Note that first, second, third and fourth generation alloys lie towards the bottom right, middle-left, top-left and top-middle, respectively.**

A final point concerns the top left hand corner of Fig.12, where third and fourth generation alloys such as TMS-75 and CMSX-10 lie. Here, the Gibbs free energy of formation of $Cr_2O_3$ is considered to be a significant influencing factor for the following reason. Fig.6.12 indicates that TMS-75 and CMSX-10 are less than $k_p^*$ (x-axis), but with low $|\Delta G_f|$ of chromia (y-axis). These alloys were reported to form an extensive NiO scale readily [3, 109]; this implies that it is necessary to have high $|\Delta G_f|$ of $Cr_2O_3$ to form a continuous alumina layer. This may be because of the rapid formation of a chromia + alumina continuous layer. This concept is supported not only by Ref. [14] but also by a recent STEM-EDX observation of a continuous chromia + alumina layer formed after the exposure at 950ºC for 0.1 hour [142].

### 6.5.4 Critique of Oxidation Performance for Alloy Design Purposes

The modelling methods proposed can be used to predict the sensitivity of oxidation kinetics to superalloy composition; moreover they are useful for the purposes of alloy design. A typical procedure might be as follows. Starting with a baseline superalloy composition of interest, calculations for $k_p$ based upon the $Al_2O_3$ rate-controlling model and also for $\Delta G_f$ for chromia formation can be made by systematically altering the chemical composition by 1 at.%, for each of the alloying elements present. The calculated result can be shown on the new oxidation diagram, with vectors identifying the changes in position of the alloy on the diagram, as was done in Fig.6.10. Consistent with the emphasis of this paper, the high-Cr containing first generation nickel-based superalloy SCA425+ is chosen to illustrate concepts, see Fig.6.14a. It can be seen from Fig.6.14a that the removal W is predicted to be the most efficient way for SCA425+ to move towards the domain of $Al_2O_3$ rate-controlling kinetics. This further rationalises the experimental observations of section 6.4.

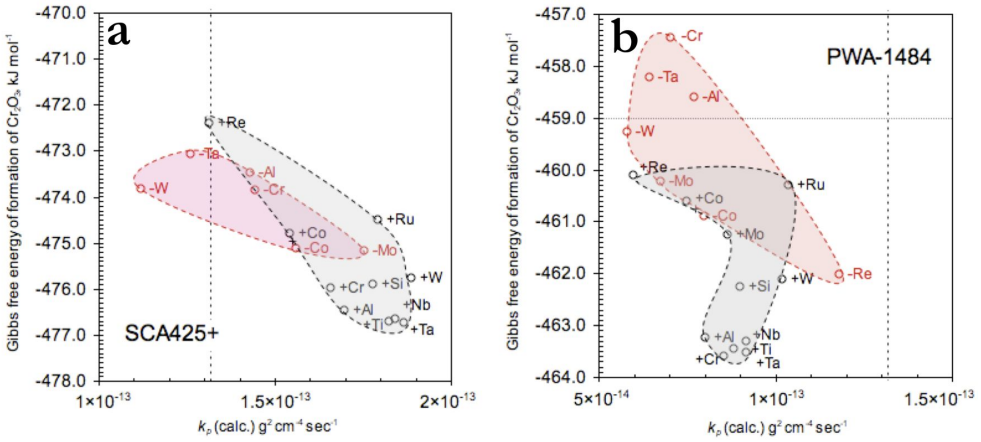


**Fig.6.14 The effect of altering alloying element concentrations on the oxidation diagram at 900ºC for (a) SCA425+ and (b) PWA-1484. The black solid line is calculated by increasing the composition of base alloy by 1 at.% for each of its alloying elements, and the red solid line by decreasing the composition by 1 at.%. The horizontal and vertical lines correspond to the critical values plotted on Fig.6.12.**

An analysis can also be made of the evolutionary trends that have occurred in superalloy compositions in recent years. For example, it is well known that there has been a trend to reduce the Cr contents of single crystal superalloys, *e.g.* from the 2nd to 3rd generation superalloys [3]; what are the implications of this? Consider the second generation superalloy PWA-1484 which contains 5 wt.% Cr, see Fig.6.14b. Further addition of 1at.% Re to PWA-1484 (*i.e.* an alloy then containing 5.9 wt.% rather than 3.0wt.%Re) is insufficient to take the alloy away from the alumina rate-controlling region. Thus Re in these quantities is not predicted to be detrimental. On the other hand, it can be seen from Fig.6.14b that a reduction of 1at.% Cr causes a very substantial shift upwards along the y-axis. Thus, our analysis indicates that it is the reduction in Cr which is the cause of the inferior oxidation resistance found for 3rd generation superalloys [3, 109] rather than the enhanced alloying with Re. It is also clear from comparing Fig.6.14a with 6.14b that any reduction of Cr is rather less effective in a high-Cr superalloy such as the SCA425+ alloy considered here.

## 6.6 Summary and Conclusions

The following conclusions can be withdrawn from this work:

(1) The weight gain accumulated by SCA425+ at 900ºC is influenced by substitution of W by Re. The stabilised parabolic oxidation rate decreased from $4.87\times10^{-13}$ to $8.31\times10^{-14}$ $g^2\ cm^{-4}\ sec^{-1}$ at this temperature.

(2) This observation is at odds with the common belief that Re-alloying is detrimental to oxidation; it is however consistent with the oxidation diagram concept which has recently been proposed.

(3) The model is further extended into the $Cr_2O_3$ rate-controlling criteria, and the stabilised parabolic oxidation rate in the literature could be rationalised with this extended model.

(4) The oxidation behaviours of various generations of nickel-based superalloys have been analysed. The beneficial effect of W to Re substitution is shown to be one major contributory factor in the superior oxidation resistance of the commercially-available second generation superalloys.

(5) Our analysis confirms that it is the lack of Cr which is the main causes of the poor oxidation performance of the 3rd generation superalloys.

# Chapter 7. Summary, Conclusions and Future Work

## 7.1 Summary of Conclusions

In chapter 1, the literature concerning the high temperature oxidation and deformation of nickel-based single crystal superalloys was reviewed. In order to estimate the extent of high temperature oxidation, the chemical kinetics were rationalised using thermodynamics & kinetic theory based upon Wagner's theory of parabolic oxidation. Additionally, consistent with the Wagner-Haffe theory, the effect of the foreign cations on the mother oxide growth was considered. The chemical kinetics of oxide growth may be influenced by (i) the Gibbs free energy of formation and (ii) the presence of impurities (foreign cations); this idea was further expanded upon in chapter 3. Secondly, the effect of transformation of oxide on chemical kinetics was reviewed. The transformation of $Al_2O_3$ from the metastable states ($\gamma$, $\theta$) to the stable state ($\alpha$) occurs during the early stage of oxidation, and can decelerate its chemical kinetics by more than an order of magnitude. This effect of transformation of the oxide was further investigated in chapter 4. Finally, the high temperature deformation of nickel-based superalloys was classified with emphasis on the microstructure factors influencing the behaviour. In the temperature range between 0.5-0.9$T_M$, creep deformation can occur. The creep strain rate can be modelled according

to a hyperbolic function of gamma prime particles interspacing, in the absence of particle shearing. Between 0.3-0.5$T_M$, creep becomes unimportant; instead, fatigue deformation should be considered. Since fatigue deformation initiates from the formation of persistent slip bands together with the particle shearing within each band, it was also concluded from the shearing theory that the shearing resistance is proportional to the square root of the gamma prime particle size. These ideas were tested in chapter 5.

In chapter 2, methods for designing, producing and optimizing the candidate were described. A high Cr-containing nickel-based superalloy SCA425+ was designed based upon the IN738LC-based SCA425 alloy, with better predicted properties particularly in oxidation. The oxidation resistance of SCA425+ with and without Si was evaluated in chapter 3 and 4. The mechanical properties of SCA425+ were investigated in chapter 5. Three different microstructures were prepared for SCA425+, so that the microstructural factors influencing both creep and thermomechanical fatigue would be understood. Finally, consistent with the result in chapter 3, a further derivative of SCA425+ containing 2 wt.% Re was prepared and its oxidation performance was evaluated in chapter 6.

In chapter 3, the oxidation resistance of SCA425+ with and without Si was studied. All alloys were found to be marginal $Al_2O_3$-formers, with the performance being better at 1000ºC rather than 900ºC and when Si was added. To explain the results, the two factors known to influence the rate of $Al_2O_3$ scale formation were considered: (i) the Gibbs free energy of formation of $Al_2O_3$, and (ii) the impurities factor (denoted as $Val_I^{eff}$). A model was developed to predict whether or not any given alloy composition will form a continuous $Al_2O_3$ scale. This was used to rationalise the dependence of $Al_2O_3$ scale formation on alloy composition in these systems. The model predicted that the additions of Al, Si, Cr were predicted to be beneficial with regard to $Al_2O_3$ formation; on the other

hand, the additions of W, Ta, Nb, Ru, Ti and Mo were detrimental. In order to improve the oxidation resistance of nickel-based superalloys, other suggestions arising from these quantitative calculations include (i) replacement of W and/or Mo with Re, and (ii) substitution of Ni by Co. Note however that Co additions were reported to deteriorate $Al_2O_3$/metal bonding toughness [114]; thus this was not recommended. However, the replacement of W with Re was further tested in chapter 6. Note that the predicted influence of Si was only slight, and this calculation/experiment gap was likely to imply the additional beneficial effects of Si on the nucleation of $Al_2O_3$ formation, and this was investigated furthermore in chapter 4.

In chapter 4, the oxidation behaviour of SCA425+ at 950ºC was further studied, with and without silicon alloying. It was demonstrated that the alloy is a marginal alumina former, with further alloying by Si promoting the formation of a continuous, protective alumina scale. The addition of Si decreased the transformation time to reach $k_p$ values representative of $\alpha$-$Al_2O_3$ by an order of magnitude, and the reason for this was considered to be as follows. First, the formation of alumina was already observed in the alloy containing 0.25 wt.% Si alloy after 0.1 hour exposure at 950ºC, before the $k_p$ reaches a level representative of $\alpha$-$Al_2O_3$. Here, XRD could not detect the presence of the stable $\alpha$-$Al_2O_3$ peaks. This, together with our TEM observations, suggested that metastable alumina was forming in the early stages of oxidation. On the other hand, $\alpha$-$Al_2O_3$ peaks were detected after 3 hours exposure at 950ºC; moreover, the presence of silicon clusters within the alumina was observed using atom probe tomography. Therefore, Si might play in role in altering the oxidation rate *via* an effect on the rate of transformation of metastable alumina to its stable $\alpha$-$Al_2O_3$ form. Note that the additions of $SiO_2$ to $\alpha$-$Al_2O_3$ have in fact been suggested to decrease the metastable -> stable $Al_2O_3$ transformation

temperature, by increasing the heterogeneous nucleation sites for its transformation [125]; however further microstructural confirmation will be required for this. The amount of silicon doping was found to be optimal at around 0.25wt.%.

In chapter 5, the mechanical behaviour of SCA425+ was studied under creep and out-of-phase thermomechanical fatigue (OP-TMF) conditions. Neutron diffraction methods and thermodynamic modelling were used to quantify the variation of the gamma prime (γ') strengthening phase around the γ' solvus temperature. These aided the design of primary ageing heat treatments to develop either uniform or bimodal microstructures of the γ' phase. Note that three different microstructures were prepared for each form of testing. Firstly, under creep conditions in the temperature range 750ºC-850ºC with stresses between 235-520MPa, the dislocation activity was mostly restricted to the matrix phase, and the creep performance was best with a finer and uniform γ' microstructure (i.e. shortest particle interspacing). The creep rupture performance approaches that of IN792 which was one of the goals of the SCA425+ alloy development project. Secondly, thermomechanical fatigue caused localised shear banding with the γ' phase penetrated by dislocations; moreover, the out-of-phase TMF performance improved when the γ' precipitate size was larger. Also, it was found that the creep relaxation damage was small. Thus the micro-mechanical degradation mechanisms occurring during creep and TMF were distinct.

In chapter 6, the oxidation behaviour of a prototype nickel-based single crystal superalloy containing ~15 wt.% Cr was studied at 900ºC, with and without W -> Re replacement. It was demonstrated that the alloy is a marginal alumina former, with further substitution of W with Re promoting the formation of a more protective alumina scale. Theoretical

considerations – including the recently developed oxidation diagram concept – were used to rationalise the results. The analysis methods were extended to consider the oxidation performance of commercially-available nickel-based superalloys as a function of their alloy chemistry. It was demonstrated that broad composition/performance relationships could be identified.

## 7.2 Future Work

Based upon the research work presented here, the following suggestions are made. First, the beneficial effect of silicon during the early stage of oxidation is not well understood as yet. Si might play a role in becoming a heterogeneous nucleation sites for $\alpha$-$Al_2O_3$. Or alternatively, Si may play a role in hindering the inward growth of $\alpha$-$Al_2O_3$ during the process of internal oxidation. Further TEM work for the silicon containing alloy is necessary to identify the crystal structure of $Al_2O_3$ in the early stage of oxidation. Furthermore, $O^{16}/O^{18}$ isotope oxidation testing with and without Si alloying is required to understand whether or not silicon at the grain boundaries influences the diffusion of oxygen.

Secondly, it was found from chapter 5 that TMF resistance can be explained by the particle shearing resistance. This implies that higher volume fraction of gamma prime particles may also be beneficial for TMF resistance. To test this hypothesis, nickel-based superalloys with high volume fraction of gamma prime, together with larger gamma prime particles distribution, should be evaluated by TMF testing.

Finally, it was found at the end of chapter 6 that the Gibbs free energy of formation of $Cr_2O_3$ is likely to be the factor controlling $Al_2O_3$ layer formation. Since this work was carried out based upon alloys for IGTs applications, the critical $\Delta G_f$ remains unclear, and further oxidation analysis on low-Cr containing nickel-based superalloys is required.

# Appendix

## A.1 Glossary of Common Terms

Except where defined otherwise, the following abbreviations, acronyms or symbols can be taken to mean:

$\gamma$ .....$\gamma$-Ni phase

$\gamma'$ .....$\gamma'$-$Ni_3Al$ phase

$\Delta G_f$ .....Gibbs free energy of formation

$\Delta G_0$ .....standard free energy of formation

$T$ .....absolute temperature

$R$ .....gas constant

$a_M$ .....activity of element M in the multi-component system

$P_{O_2}$ .....Partial pressure of oxygen

$\Delta x$ .....thickness of oxide

$P_{O_2}^{outs}$ .....partial pressure of oxygen at outer surface of oxide

$P_{O_2}^{ins}$ .....partial pressure of oxygen at inter surface of oxide

$\sigma_t$ .....conductivity of the $M_xO_y$ oxide

$t_i$, .....transport number of cation ($0 < t < 1$)

$t_a$ .....transport number of anion ($0 < t < 1$)

$t_{el}$ .....transport number of electrons ($0 < t < 1$)

$z_c$ .....metal ion's valence

$z_a$ .....oxygen ion's valence

$e$ .....elementary charge

$\mu$ .....chemical potential

$k_t$ .....parabolic oxidation rate (theoretical)

$k_p$ .....parabolic oxidation rate (derived from thermogravimetric data)

$T_M$ .....Melting temperature

$b$ .....Burgers vector

$\rho$ .....dislocation density

$v$ .....average velocity of dislocation motion (i.e. glide rate) within matrix

$t$ .....time

$d$ .....diameter of γ' phase

$D_{eff}$ .....effective diffusion coefficient

$\gamma_{APB}$ .....anti-phase boundary (APB) energy

$r$ .....radius of precipitate

$f$ .....volume fraction of precipitate

$\tau_{CRSS}$ .....critical resolved shear stress

$\varepsilon$ .....strain

$\sigma$ .....stress

$\alpha$ .....thermal expansion coefficient

$c_e$ .....fatigue strength coefficient

$c_p$ .....fatigue ductility coefficient

$\sigma^{\gamma/\gamma'}$ .....γ/γ' interfacial energy per unit area

$N_\alpha$ .....total mole fraction of solute in γ phase

$V_m$ .....molar volume of the γ' phase

β .....an empirically determined constant

$\Delta H_m$ .....enthalpy of solution of 1 mole of γ' in the γ in equilibrium

$E$ .....Young's modulus

L .....Liquid

$c_o$ .....concentration of oxygen in the oxide

$D_o$ .....diffusion coefficient of oxygen

$k$ .....Boltzmann constant

$Val_i^{eff}$ .....effective valence

# A.2 List of Figures

# A.3 List of Tables

# References


1. Wee, D. M. and Suzuki, T. (1979). *The Temperature Dependence of Hardness of $L1_2$ Ordered Alloys*. Transactions of the Japan Institute of Metals **20** (11): p.634-646.
2. Nash, P., Singleton, M. F. and Murray, J. L. (1991). "*Al-Ni, Phase Diagrams of Binary Nickel Alloys*." ASM International; Available from http://crystdb.nims.go.jp/.
3. Reed, R. C. (2006). *The Superalloys -Fundamentals and Applications-*, Cambridge University Press.
4. Darolia, R. and Matey, D. M. Patent no. *US8710284*
5. Nabarro, F. R. N. and deVilliers, H. L. (1995). *The Physics of Creep*. London, Taylor & Francis.
6. Konter, M. and Thumann, M. (2001). *Materials and Manufacturing of Advanced Industrial Gas Turbine Components*. Journal of Materials Processing Technology **117** (3): p. 386-390.
7. Bensch, M., Preussner, J., Huttner, R., Obigodi, G., Virtanen, S., Gabel, J. and Glatzel, U. (2010). *Modelling and Analysis of the Oxidation Influence on Creep Behaviour of Thin-Walled Structures of the Single-Crystal Nickel-Base Superalloy Rene'N5 at 980°c*. Acta Materialia **58** (5): p.1607-1617.
8. Birks, N., Meier, G. and Pettit, F. (2006). *Introduction to the High-Temperature Oxidation of Metals*, Cambridge University Press.
9. Saunders, N. and Miodownik, A. P. (1998). *CALPHAD -Calculation of Phase Diagrams-a Comprehensive Guide*. Kidlington, Oxford, Elsevier Science.
10. Wagner, C. (1933). *The Theory of the Warm-up Process*. Zeitschrift Fur Physikalische Chemie-Abteilung B-Chemie Der Elementarprozesse Aufbau Der Materie **21** (1/2): p.25-41.
11. deWit, J. H. W. (1981). *High Temperature Oxidation of Metals*. Journal of Material Education **3**: p.333-377.
12. Kofstad, P. (1983). *Nonstoichiometry, Diffusion and Electrical Conductivity in Binary Metal Oxides*. Malabar (FL), Robert E. Krieger.
13. Pettit, F. S. (1967). *Oxidation Mechanisms for Nickel-Aluminum Alloys at Temperatures between 900°c and 1300°c*. Transactions of the Metallurgical Society of AIME **239** (9): p.1296-1305.
14. Giggins, C. S. and Pettit, F. S. (1971). *Oxidation of Ni-Cr-Al Alloys between 1000°c and 1200°c*. Journal of the Electrochemical Society **118** (11): p.1782-1790.
15. Brumm, M. W. and Grabke, H. J. (1992). *The Oxidation Behavior of NiAl-1. Phase Transformations in the Alumina Scale During Oxidation of NiAl and NiAl-Cr Alloys*. Corrosion Science **33** (11): p.1677-1690.
16. Doychak, J., Smialek, J. L. and Mitchell, T. E. (1989). *Transient Oxidation of Single-Crystal Beta- NiAl*. Metallurgical Transactions A: Physical Metallurgy and Materials Science **20** (3): p.499-518.
17. Rybicki, G. C. and Smialek, J. L. (1989). *Effect of the Theta-Alpha-$Al_2O_3$ Transformation on the Oxidation Behavior of Beta NiAl+ Zr*. Oxidation of Metals **31** (3-4): p.275-304.

18. Ryshkewitch, E. (1960). *Oxide Ceramics: Physical Chemistry and Technology*, Academic Press.
19. Shackelford, J. F. and Doremus, R. H. (2008). *Ceramic and Glass Materials: Structure, Properties and Processing*, Springer.
20. Quadakkers, W. J., Elschner, A., Speier, W. and Nickel, H. (1991). *Composition and Growth Mechanisms of Alumina Scales on FeCrAl-Based Alloys Determined by SNMS*. Applied Surface Science **52** (4): p.271-287.
21. Prescott, R., Mitchell, D. F., Sproule, G. I. and Graham, M. J. (1992). *Transport in Alpha-$Al_2O_3$ Scales on Fe-Al and Ni-Al Alloys at 1100°c*. Solid State Ionics **53**: p. 229-237.
22. Pint, B. A., Martin, J. R. and Hobbs, L. W. (1995). *The Oxidation Mechanism of Theta-$Al_2O_3$ Scales*. Solid State Ionics **78** (1-2): p.99-107.
23. Hagel, W. C. (1963). *Factors Controlling the High Temperature Oxidation of Chromium*. Transactions of the American Society of Metals Quarterly **56**: p.583-595.
24. McPherson, D. J. and Fontana, M. G. (1951). *Preparation and Properties of Titanium-Chromium Binary Alloys*. Transactions of the American Society for Metals **43**: p. 1098-1125.
25. Caplan, D. and Cohen, M. (1961). *The Volatilization of Chromium Oxide*. Journal of the Electrochemical Society **105** (5): p.438.
26. Tedmon, C. S. (1966). *Effect of Oxide Volatilization on Oxidation Kinetics of Cr and Fe-Cr Alloys*. Journal of the Electrochemical Society **113** (8): p.766-768.
27. McLean, D. (1966). *Physics of High Temperature Creep in Metals*. Reports on Progress in Physics **29**: p.1-33.
28. Dyson, B. F. (2009). *Microstructure Based Creep Constitutive Model for Precipitation Strengthened Alloys: Theory and Application*. Materials Science and Technology **25** (2): p. 213-220.
29. Reed, R. C., Tao, T. and Warnken, N. (2009). *Alloys-by-Design: Application to Nickel-Based Single Crystal Superalloys*. Acta Materialia **57** (19): p.5898-5913.
30. Caron, P. and Khan, T. (1983). *Improvement of Creep Strength in a Nickel-Base Single-Crystal Superalloy by Heat-Treatment*. Materials Science and Engineering **61** (2): p. 173-184.
31. Pollock, T. M. and Argon, A. S. (1994). *Directional Coarsening in Nickel-Base Single-Crystals with High-Volume Fractions of Coherent Precipitates*. Acta Metallurgica Et Materialia **42** (6): p.1859-1874.
32. Caron, P., Henderson, P. J., Khan, T. and McLean, M. (1986). *On the Effects of Heat-Treatments on the Creep-Behavior of a Single-Crystal Superalloy*. Scripta Metallurgica **20** (6): p.875-880.
33. Tetzlaff, U. and Mughrabi, H. (2000). *Enhancement of the High-Temperature Tensile Creep Strength of Monocrystalline Nickel-Base Superalloys by Pre-Rafting in Compression*. Superalloys 2000. In: T. M. Pollock, R. D. Kissinger, R. R. Bowman, et al. eds., Warrendale, Minerals, Metals & Materials Soc: p.273-282.
34. Mughrabi, H. (2009). *Microstructural Aspects of High Temperature Deformation of Monocrystalline Nickel Base Superalloys: Some Open Problems*. Materials Science and Technology **25** (2): p.191-204.
35. Nabarro, F. R. N. (1996). *Rafting in Superalloys*. Metallurgical and Materials Transactions A: Physical Metallurgy and Materials Science **27** (3): p.513-530.
36. Koizumi, Y., Zhang, J. X., Kobayashi, T., Yokokawa, T., Harada, H., Aoki, Y. and Arai, M. (2003). *Development of Next Generation Ni-Base Single Crystal Superalloys Containing Ruthenium*. Journal of the Japan Institute of Metals **67** (9): p.468-471.

37. Zhang, J. X., Murakumo, T., Harada, H. and Koizumi, Y. (2003). *Dependence of Creep Strength on the Interfacial Dislocations in a Fourth Generation SC Superalloy TMS-138*. Scripta Materialia **48** (3): p.287-293.
38. Zhang, J. X., Murakumo, T., Koizumi, Y., Kobayashi, T. and Harada, H. (2003). *Interfacial Dislocations and Creep Strength in a Fourth Generation SC Superalloy TMS-138*, Tainetsu Kinzoku Zairyo 123 research report **1**: p.289.
39. Zhang, J. X., Koizumi, Y., Kobayashi, T., Murakumo, T. and Harada, H. (2004). *Strengthening by Gamma/Gamma Prime Interfacial Dislocation Networks in TMS-162 - toward a Fifth-Generation Single-Crystal Superalloy*. Metallurgical and Materials Transactions A: Physical Metallurgy and Materials Science **35A** (6): p.1911-1914.
40. Yeh, A. C., Rae, C. M. F. and Tin, S. (2004). *High Temperature Creep of Ru-Bearing Ni-Base Single Crystal Superalloys*. Superalloys 2004. In: K. A. Green, T. M. Pollock, H. Harada, et al. eds., Warrendale(PA), Minerals, Metals & Materials Soc: p.677-685.
41. Erickson, G. L. (1996). *The Development and Application of CMSX-10*. Superalloys 1996. In: R. D. Kissinger, D. J. Deye, D. L. Anton, et al. eds., Warrendale (PA), Minerals, Metals & Materials Soc: p.35-44.
42. Sato, A., Koizumi, Y., Kobayashi, T., Yokokawa, T., Harada, H. and Imai, H. (2004). *TTT Diagram for TCP Phases Precipitation of 4th Generation Ni-Base Superalloys*. Journal of the Japan Institute of Metals **68** (8): p.507-510.
43. Sato, A., Harada, H., Yokokawa, T., Murakumo, T., Koizumi, Y., Kobayashi, T. and Imai, H. (2006). *The Effects of Ruthenium on the Phase Stability of Fourth Generation Ni-Base Single Crystal Superalloys*. Scripta Materialia **54** (9): p.1679-1684.
44. Reed, R. C., Cox, D. C. and Rae, C. M. F. (2007). *Damage Accumulation During Creep Deformation of a Single Crystal Superalloy at 1150°c*. Materials Science & Engineering, A: Structural Materials: Properties, Microstructure and Processing **448** (1-2): p.88-96.
45. Beardmore, P., Davies, R. G. and Johnston, T. L. (1969). *On the Temperature Dependence of the Flow Stress of Nickel-Base Alloys (Flow Stress Temperature Dependence of Ni-Cr-Al Alloys Consisting of Gamma Prime Dispersion in Ni Base Solid Solution)*. Transactions of the Metallurgical Society of AIME **245**: p.1537-1545.
46. Ardell, A. J. (1985). *Precipitation Hardening*. Metallurgical Transactions A: Physical Metallurgy and Materials Science **16** (12): p.2131-2165.
47. Huther, W. and Reppich, B. (1978). *Interaction of Dislocations with Coherent, Stress-Free, Ordered Particles*. Zeitschrift Fur Metallkunde **69** (10): p.628-634.
48. Jackson, M. P. and Reed, R. C. (1999). *Heat Treatment of Udimet 720Li: The Effect of Microstructure on Properties*. Materials Science & Engineering, A: Structural Materials: Properties, Microstructure and Processing **259** (1): p.85-97.
49. Hertzberg, R. W. (1996). *Deformation and Fracture Mechanics of Engineering Materials*, John Wiley & Sons
50. Manson, S. (1965). *Fatigue: A Complex Subject—Some Simple Approximations*. Experimental Mechanics **5** (7): p.193-226.
51. Mughrabi, H., Kraft, S. and Ott, M. (1996). *Specific Aspects of Isothermal and Anisothermal Fatigue of the Monocrystalline Nickel-Base Superalloy CMSX-6*. Superalloys 1996. In: R. D. Kissinger, D. J. Deye, D. L. Anton, et al. eds., Warrendale, Minerals, Metals & Materials Soc: p.335-344.
52. Solomon, H. D., Halford, G. R., Kaisand, L. R. and Leis, B. N. (1988). *Low Cycle Fatigue*. New York, ASTM.
53. Neu, R. W. and Sehitoglu, H. (1989). *Thermomechanical Fatigue, Oxidation, and Creep .1. Damage Mechanisms*. Metallurgical Transactions A: Physical Metallurgy and Materials Science **20** (9): p.1755-1767.

54. Pineau, A. and Antolovich, S. D. (2009). *High Temperature Fatigue of Nickel-Base Superalloys - a Review with Special Emphasis on Deformation Modes and Oxidation*. Engineering Failure Analysis **16** (8): p.2668-2697.
55. Moverare, J. J., Johansson, S. and Reed, R. C. (2009). *Deformation and Damage Mechanisms During Thermal-Mechanical Fatigue of a Single-Crystal Superalloy*. Acta Materialia **57** (7): p.2266-2276.
56. Sakamoto, M., Harada, H., Yokokawa, T., Koizumi, Y., Kobayashi, T., Zhou, H., Zhang, J. X. and Miyamoto, N. (2008). *Assessment on the Thermo-Mechanical Fatigue Properties of 98 Ni-Base Single Crystal Superalloys*. Superalloys 2008. In: R. C. Reed, K. A. Green, P. Caron, et al. eds., Warrendale, Minerals, Metals & Materials Soc: p.521-526.
57. Zhang, J. X., Harada, H., Ro, Y. and Koizumi, Y. (2006). *Superior Thermo-Mechanical Fatigue Property of a Superalloy Due to Its Heterogeneous Microstructure*. Scripta Materialia **55** (8): p.731-734.
58. Zhang, J. X., Harada, H., Ro, Y., Koizumi, Y. and Kobayashi, T. (2008). *Thermomechanical Fatigue Mechanism in a Modern Single Crystal Nickel Base Superalloy TMS-82*. Acta Materialia **56** (13): p.2975-2987.
59. Ohata, H., Yokokawa, T., Kobayashi, T., Ro, Y. and Harada, H. (2006). *Prediction of Thermal Mechanical Fatigue Properties of Ni-Base Single Crystal Superalloys*. Journal of the Japan Institute of Metals **70** (3): p.246-249.
60. Moverare, J. J. and Johansson, S. (2010). *Damage Mechanisms of a High-Cr Single Crystal Superalloy During Thermomechanical Fatigue*. Materials Science & Engineering, A: Structural Materials: Properties, Microstructure and Processing **527** (3): p.553-558.
61. Neu, R. W. and Sehitoglu, H. (1989). *Thermomechanical Fatigue, Oxidation, and Creep .2. Life Prediction*. Metallurgical Transactions A: Physical Metallurgy and Materials Science **20** (9): p.1769-1783.
62. Evans, A. G., He, M. Y., Suzuki, A., Gigliotti, M., Hazel, B. and Pollock, T. M. (2009). *A Mechanism Governing Oxidation-Assisted Low-Cycle Fatigue of Superalloys*. Acta Materialia **57** (10): p.2969-2983.
63. Ott, M. and Mughrabi, H. (1999). *Dependence of the High-Temperature Low-Cycle Fatigue Behaviour of the Monocrystalline Nickel-Base Superalloys CMSX-4 and CMSX-6 on the Gamma/Gamma' Morphology*. Materials Science and Engineering a-Structural Materials Properties Microstructure and Processing **272** (1): p.24-30.
64. Lifshitz, I. M. and Slyozov, V. V. (1961). *The Kinetics of Precipitation from Supersaturated Solid Solutions*. Journal of Physics and Chemistry of Solids **19** (1-2): p.35-50.
65. Wagner, C. (1961). *Theorie Der Alterung Von Niederschlagen Durch Umlosen (Ostwald-Reifung)*. Zeitschrift Fur Elektrochemie **65** (7-8): p.581-591.
66. Calderon, H. A., Voorhees, P. W., Murray, J. L. and Kostorz, G. (1994). *Ostwald Ripening in Concentrated Alloys*. Acta Metallurgica Et Materialia **42** (3): p.991-1000.
67. Li, X., Saunders, N. and Miodownik, A. P. (2002). *The Coarsening Kinetics of Gamma Prime Particles in Nickel-Based Alloys*. Metallurgical and Materials Transactions A: Physical Metallurgy and Materials Science **33** (11): p.3367-3373.
68. Boettinger, W. J., Kattner, U. R., Coriell, S. R., Chang, Y. A. and Mueller, B. A. (1995). *Development of Multicomponent Solidification Micromodels Using a Thermodynamic Phase Diagram Data Base*. Warrendale, Minerals, Metals & Materials Soc.
69. Karunaratne, M. S. A., Carter, P. and Reed, R. C. (2000). *Interdiffusion in the Face-Centred Cubic Phase of the Ni-Re, Ni-Ta and Ni-W Systems between 900 and 1300°c*. Materials Science & Engineering, A: Structural Materials: Properties, Microstructure and Processing **281** (1-2): p.229-233.
70. Hasselqvist, M. and McColvin, G. (2008). *Nickel-Base Superalloys*. Patent no. *WO2008046708A1*

71. Smialek, J. L., Barrett, C. A. and Schaeffer, J. C. (1997). *Design for Oxidation Resistance*. ASM International. eds., Materials Park (OH). **20** p.598-602.
72. Harada, H., Yamazaki, M. and Koizumi, Y. (1979). *A Series of Nickel-Base Superalloys on Gamma-Gamma Prime Tie Line of Alloy Inconel 713c*. Tetsu to Hagane **65** (7): p. 1049-1058.
73. Darolia, R., Lahrman, D. F., Field, R. D. and Sisson, R. (1988). *Formation of Topologically Closed Packed Phases in Nickel Base Single Crystal Superalloys*. Superalloys1988. In: S. Reichman, D. N. Duhl, G. Maurer, S. Antolovich and C. Lund, The Metallurgical Society: p.255-264.
74. Rae, C. M. F., Karunaratne, M. S. A., Small, C. J., Broomfield, R. W., Jones, C. N. and Reed, R. C. (2000). *Topologically Close Packed Phases in an Experimental Rhenium-Containing Single Crystal Superalloy*. Superalloys 2000. In: T. M. Pollock, R. D. Kissinger, R. R. Bowman, et al. eds., Warrendale, Minerals, Metals & Materials Soc: p.767-776.
75. Saunders, N., Li, X., Miodownik, A. P. and Schille, J. P. (2001). *Computer Modelling of Materials Properties*. Materials Design Approaches and Experiences. In: J. C. Zhao, M. Fahrmann and T. M. Pollock eds., Warrendale, Minerals, Metals & Materials Soc: p. 185-197.
76. Hino, T., Yoshioka, Y., Nagata, K., Kashiwara, H., Kobayashi, T. and Koizumi, Y. (1998). *Design of High Re Containing Single Crystal Superalloys for Industrial Gas Turbines*. Materials for advanced power engineering 1998, Forschungszentrum Julich.
77. Koizumi, Y., Koguchi, H., Yokokawa, T., Kobayashi, T., Osawa, M., Kimura, T. and Harada, H. (2004). *Effect of Ru Additions on the TCP-Phase Formation and Creep Strength of a Ni-Base Single Crystal Superalloy*. Journal of the Japan Institute of Metals **68** (2): p. 54-57.
78. Caron, P., Blackler, M., McColvin, G. M., Wahi, R. P., Escale, A. M. and Lelait, L. (2005). *Nickel-Based Superalloy Having Very High Registance to Hot-Corrosion for Monocrystalline Blades of Industrial Turbines*. Patent no. *US20050194068A1*
79. Walston, S., Cetel, A., MacKay, R., O'Hara, K., Duhl, D. and Dreshfield, R. (2004). *Joint Development of a Fourth Generation Single Crystal Superalloy*. Superalloys 2004. In: K. A. Green, T. M. Pollock, H. Harada, et al. eds., Warrendale, Minerals, Metals & Materials Soc: p.15-24.
80. Murakami, H., Yamagata, T., Harada, H. and Yamazaki, M. (1997). *The Influence of Co on Creep Deformation Anisotropy in Ni-Base Single Crystal Superalloys at Intermediate Temperatures*. Materials Science and Engineering: A **223** (1-2): p.54-58.
81. Hasselqvist, M., Reed, R. C., Moverare, J. J. and Sato, A. (2010). *New Turbine Alloys Which Combine Oxidation and Corrosion Resistance*. 1st International Symposium on Eurosuperalloys.
82. Miner.Jr, R. V. and Lowell, C. E. (1975). *Effects of Silicon Additions on Oxidation and Mechanical Behavior of the Nickel-Base Superalloy B-1900*. Ohio, Lewis Research Center, National Aeronautics and Space Administration.
83. Li, B. and Gleeson, B. (2006). *Effects of Silicon on the Oxidation Behavior of Ni-Base Chromia-Forming Alloys*. Oxidation of Metals **65** (1-2): p.101-122.
84. Sato, A., Harada, H., Ang, J., Koizumi, Y., Kobayashi, T., Kawagishi, K. and Imai, H. (2006). *Oxidation Resistance of Silicon-Containing 5th Generation Nickel-Base Single Crystal Superalloys*. Materials for Advanced Power Engineering 2006. In: J. Lecomte-Beckers, M. Carton, F. Schubert and P. J. Ennis eds., Liege, Schriften des Forschungszentrums julich. **53**: p.655-664.

85. Yeh, A. C., Kawagishi, K., Harada, H., Yokokawa, T., Koizumi, Y., Kobayashi, T., Ping, D. H., Fujioka, J. and Suzuki, T. (2008). *Development of Si-Bearing 4th Generation Ni-Base Single Crystal Superalloys*. Superalloys 2008. In: R. C. Reed, K. A. Green, P. Caron, et al. eds., Warrendale(PA), Minerals, Metals & Materials Soc: p.619-628.
86. Funkenbusch, A. W., Smeggil, J. G. and Bornstein, N. S. (1985). *Reactive Element - Sulfur Interaction and Oxide Scale Adherence*. Metallurgical Transactions A: Physical Metallurgy and Materials Science **16** (6): p.1164-1166.
87. Ikeda, Y., Tosa, M., Yoshihara, K. and Nll, K. (1989). *Detrimental Effect of S-Segregation to Adherence of $Al_2O_3$ Coating Layer on Stainless-Steels and Superalloys*. ISIJ International **29** (11): p.966-972.
88. Smialek, J. L. (2001). *Advances in the Oxidation Resistance of High-Temperature Turbine Materials*. Surface and Interface Analysis **31** (7): p.582-592.
89. Smialek, J. L. and Morscher, G. N. (2002). *Delayed Alumina Scale Spallation on Rene'N5+Y: Moisture Effects and Acoustic Emission*. Materials Science & Engineering, A: Structural Materials: Properties, Microstructure and Processing **332** (1-2): p.11-24.
90. Harris, K. and Wahl, J. B. (2004). *Improved Single Crystal Superalloys, CMSX-4 La+Y and CMSX-486*. Superalloys 2004. In: K. A. Green, T. M. Pollock, H. Harada, et al. eds., Warrendale(PA), Minerals, Metals & Materials Soc: p.45-52.
91. Bruno, G. and Pinto, H. C. (2004). *The Kinetics of the Gamma Prime Phase and Its Strain in the Nickel Base Superalloy SC16 Studied by in-Situ Neutron and Synchrotron Radiation Diffraction*. Superalloys 2004. In: K. A. Green, T. M. Pollock, H. Harada, et al. eds., Warrendale(PA), Minerals, Metals & Materials Soc: p.837-846.
92. Padture, N. P., Gell, M. and Jordan, E. H. (2002). *Materials Science - Thermal Barrier Coatings for Gas-Turbine Engine Apptications*. Science **296** (5566): p.280-284.
93. Pollock, T. M. and Argon, A. S. (1992). *Creep Resistance of CMSX-3 Nickel-Base Superalloy Single-Crystals*. Acta Metallurgica Et Materialia **40** (1): p.1-30.
94. He, M. Y. and Evans, A. G. (2010). *A Model for Oxidation-Assisted Low Cycle Fatigue of Superalloys*. Acta Materialia **58** (2): p.583-591.
95. Pint, B. A., DiStefano, J. R. and Wright, I. G. (2006). *Oxidation Resistance: One Barrier to Moving Beyond Ni-Base Superalloys*. Materials Science & Engineering, A: Structural Materials: Properties, Microstructure and Processing **415** (1-2): p.255-263.
96. Birks, N., Meier, G. H. and Pettit, F. S. (1994). *Forming Continuous Alumina Scales to Protect Superalloys*. Journal of the Minerals Metals & Materials Society **46** (12): p.42-46.
97. Gordon, A. P., Trexler, M. D., Neu, R. W., Sanders, J. T. J. and McDowell, D. L. (2007). *Corrosion Kinetics of a Directionally Solidified Ni-Base Superalloy*. Acta Materialia **55** (10): p.3375-3385.
98. Nijdam, T. J., Jeurgens, L. P. H. and Sloof, W. G. (2003). *Modelling the Thermal Oxidation of Ternary Alloys - Compositional Changes in the Alloy and the Development of Oxide Phases*. Acta Materialia **51** (18): p.5295-5307.
99. Yurek, G. (1987). *Corrosion Mechanisms*. New York, Marcel Dekker.
100. Gleeson, B. (2008). *Corrosion and Environmental Degradation*. In: M. Schutze eds., Weinheim, Wiley-VCH. **II**: p.173-228.
101. Li, C. W. and Kingery, W. D. (1984). *Structure and Properties of MgO and $Al_2O_3$ Ceramics*. Advances in Ceramics. eds., Columbus(OH), American Ceramic Society. **10**: p. 368-378.
102. Pint, B. A. and More, K. L. (2009). *Characterization of Alumina Interfaces in TBC Systems*. Journal of Materials Science **44** (7): p.1676-1686.
103. Knacke, O., Kubaschewski, O. and Hesselmann, K. (1991). *Thermo-Chemical Properties of Inorganic Substances I & Ii*. Berlin(Heidelberg), Springer.

104. *Thermotech Ni-Data Version 6*, Thermotech Ltd./Sente Software, Surrey Technology Centre, 40 Occam Road, GU2 7YG, United Kingdom
105. Wagner, C. (1950). *Solubility Relations in Ternary Solid Solutions of Ionic Compounds*. Journal of Chemical Physics **18** (1): p.62-68.
106. Pint, B. A. and Alexander, K. B. (1998). *Grain Boundary Segregation of Cation Dopants in Alpha-$Al_2O_3$ Scales*. Journal of the Electrochemical Society **145** (6): p.1819-1829.
107. Gobel, M., Rahmel, A. and Schutze, M. (1993). *The Isothermal-Oxidation Behavior of Several Nickel-Base Single-Crystal Superalloys with and without Coatings*. Oxidation of Metals **39** (3-4): p.231-261.
108. Meier, G. H., Pettit, F. S. and Onal, K. (2002). *Interaction of Steam/Air Mixtures with Turbine Airfoil Alloys and Coatings* Department of Materials Science & Engineering, 848 Benedum Hall, University of Pittsburgh, Pittsburgh, PA 15261
109. Kawagishi, K., Sato, A., Kobayashi, T. and Harada, H. (2007). *Oxidation Properties for 2nd-5th Generation Ni-Base Single-Crystal Superalloys at 1023, 1173 and 1373 K*. Journal of the Japan Institute of Metals **71** (3): p.313-319.
110. Chen, J. H., Rogers, P. M. and Little, J. A. (1997). *Oxidation Behavior of Several Chromia-Forming Commercial Nickel-Base Superalloys*. Oxidation of Metals **47** (5-6): p.381-410.
111. Onal, K., Maris-Sida, M. C., Meier, G. H. and Pettit, F. S. (2004). *The Effects of Water Vapor on the Oxidation of Nickel-Base Superalloys and Coatings at Temperatures from 700°c to 1100°c*. Superalloys 2004. In: K. A. Green, T. M. Pollock, H. Harada, et al. eds., Warrendale (PA), Minerals, Metals & Materials Soc: p.607-615.
112. Li, Y. L. and Morral, J. E. (2002). *A Local Equilibrium Model for Internal Oxidation*. Acta Materialia **50** (14): p.3683-3691.
113. Akhtar, A., Hegde, S. and Reed, R. C. (2006). *The Oxidation of Single Crystal Nickel-Based Superalloys*. Journal of the Minerals Metals & Materials Society **58** (1): p.37-42.
114. Wu, R. T. and Reed, R. C. (2008). *On the Compatibility of Single Crystal Superalloys with a Thermal Barrier Coating System*. Acta Materialia **56** (3): p.313-323.
115. Hasselqvist, M. (2010). *Private Discussion*.
116. Akhtar, A., Hook, M. S. and Reed, R. C. (2005). *On the Oxidation of the Third-Generation Single-Crystal Superalloy CMSX-10*. Metallurgical and Materials Transactions A: Physical Metallurgy and Materials Science **36A** (11): p.3001-3017.
117. Hasselqvist, M., Reed, R. C., Moverare, J. J. and Sato, A. (2010). *New Turbine Alloys Which Combine Oxidation and Corrosion Resistance*. 1st International Symposium on Eurosuperalloys.
118. Sato, A., Moverare, J. J., Hasselqvist, M. and Reed, R. C. (2011). *On the Mechanical Behaviour of a New Single Crystal Superalloy for Industrial Gas Turbine Applications* p., unpublished work.
119. Sato, A., Chiu, Y. L. and Reed, R. C. (2011). *Oxidation of Nickel-Based Single-Crystal Superalloys for Industrial Gas Turbine Applications*. Acta Materialia **59** (1): p.225-240.
120. Thompson, K., Lawrence, D., Larson, D. J., Olson, J. D., Kelly, T. F. and Gorman, B. (2007). *In Situ Site-Specific Specimen Preparation for Atom Probe Tomography*. Ultramicroscopy **107** (2-3): p.131-139.
121. Evans, H. E. and Donaldson, A. T. (1998). *Silicon and Chromium Depletion During the Long-Term Oxidation of Thin-Sectioned Austenitic Steel*. Oxidation of Metals **50** (5-6): p. 457-475.
122. Bennett, M. J., Desport, J. A. and Labun, P. A. (1984). *Analytical Electron-Microscopy of a Selective Oxide Scale Formed on 20-Percent-Cr-25-Percent-Ni-Nb Stainless-Steel*. Oxidation of Metals **22** (5-6): p.291-306.

123. Kim, S. S. and Sanders, T. H. (2001). *Thermodynamic Modeling of the Isomorphous Phase Diagrams in the Al2O3-Cr2O3 and V2O3-Cr2O3 Systems*. Journal of the American Ceramic Society **84** (8): p.1881-1884.
124. Prescott, R., Mitchell, D. F., Graham, M. J. and Doychak, J. (1995). *Oxidation Mechanisms of Beta- NiAl +Zr Determined by SIMS*. Corrosion Science **37** (9): p. 1341-1364.
125. Saito, Y., Takei, T., Hayashi, S., Yasumori, A. and Okada, K. (1998). *Effects of Amorphous and Crystalline $SiO_2$ Additives on Gamma-$Al_2O_3$-to-Alpha-$Al_2O_3$ Phase Transitions*. Journal of the American Ceramic Society **81** (8): p.2197-2200.
126. Pyczak, F., Devrient, B., Neuner, F. C. and Mughrabi, H. (2005). *The Influence of Different Alloying Elements on the Development of the Gamma/Gamma' Microstructure of Nickel-Base Superalloys During High-Temperature Annealing and Deformation*. Acta Materialia **53** (14): p.3879-3891.
127. Hasselqvist, M., Reed, R. C., Moverare, J. J. and Sato, A. (2010, submitted). *New Turbine Alloys Which Combine Oxidation and Corrosion Resistance*. 1st International Symposium on Eurosuperalloys.
128. Reed, R. C., Green, K. A., Caron, P., Gabb, T. P., Fahrmann, M. G. and Huron, E. S. (2008). Superalloys 2008. In: R. C. Reed, K. A. Green, P. Caron, et al. eds., Warrendale, John Wiley & Sons.
129. Stevens, R. A. and Flewitt, P. E. J. (1981). *The Dependence of Creep Rate on Microstructure in a Gamma'-Strengthened Superalloy*. Acta Metallurgica **29** (5): p.867-882.
130. Karunaratne, M. S. A. and Reed, R. C. (2003). *Interdiffusion of the Platinum-Group Metals in Nickel at Elevated Temperatures*. Acta Materialia **51** (10): p.2905-2919.
131. Ardell, A. J. and Nicholson, R. B. (1966). *On Modulated Structure of Aged Ni-Al Alloys*. Acta Metallurgica **14** (10): p.1295-1309.
132. Ardell, A. J. (1968). *An Application of Theory of Particle Coarsening - Gamma' Precipitate in Ni-Al Alloys*. Acta Metallurgica **16** (4): p.511-516.
133. Moverare, J. J. *Unpublished Work*.
134. Lerch, B. and Gerold, V. (1985). *Room Temperature Deformation Mechanisms in Nimonic 80a*. Acta Metallurgica **33** (9): p.1709-1716.
135. Petrenec, M., Obrtlik, K. and Polak, J. (2005). *Inhomogeneous Dislocation Structure in Fatigued Inconel 713 Lc Superalloy at Room and Elevated Temperatures*. Materials Science and Engineering A **400-401**: p.485-488.
136. Zhang, J. X., Ro, Y., Zhou, H. and Harada, H. (2006). *Deformation Twins and Failure Due to Thermo-Mechanical Cycling in TMS-75 Superalloy*. Scripta Materialia **54** (4): p. 655-660.
137. Meyers, M. A., Vohringer, O. and Lubarda, V. A. (2001). *The Onset of Twinning in Metals: A Constitutive Description*. Acta Materialia **49** (19): p.4025-4039.
138. Harris, K. and Erickson, G. L. (1984). *Single Crystal Alloy Technology*. Patent no. *US4643782*
139. Reed, R. C., Green, K. A., Caron, P., Gabb, T. P., Fahrmann, M. G. and Huron, E. S. (2008). *Proceedings of Superalloys2008, the 11th International Symposium for Superalloys*. In: R. C. Reed, K. A. Green, P. Caron, et al. eds., Warrendale(PA), USA, Minerals, Metals & Materials Soc.
140. Eliaz, N., Shemesh, G. and Latanision, R. M. (2002). *Hot Corrosion in Gas Turbine Components*. Engineering Failure Analysis **9** (1): p.31-43.
141. Moverare, J. J., Sato, A., Hasselqvist, M., Karlsson, F. and Reed, R. C. (2011). *A New Single Crystal Superalloy for Power Generation Applications*. 8th International Charles Parsons Turbine Conference, Portsmouth, UK.

142. Sato, A., Chiu, Y. L., Marquis, E. A. and Reed, R. C. (2011). *Characterisation of Oxide Scale Formation on a New Single Crystal Superalloy for Power Generation Applications*. Materials at High Temperatures. **Submitted**.
143. Kawagishi, K., Harada, H., Sato, A., Sato, A. and Kobayashi, T. (2006). *The Oxidation Properties of Fourth Generation Singlen-Crystal Nickel-Based Superalloys*. Journal of the Minerals Metals & Materials Society **58** (1): p.43-46.
144. Moverare, J. J., Sato, A., Johansson, S., Hasselqvist, M., Reed, R. C., Kanesund, J. and Simonsson, K. (2011). *On Localized Deformation and Recrystallization as a Damage Mechanisms During Thermomechanical Fatigue of Single Crystal Nickel-Based Superalloys*. Advanced Materials Research **278**: p.357-362.
145. Sato, A., Moverare, J. J., Hasselqvist, M. and Reed, R. C. (2011). *On the Mechanical Behaviour of a New Single Crystal Superalloy for Industrial Gas Turbine Applications* Metallurgical and Materials Transactions A **Submitted**.
146. Oishi, Y. and Kingery, W. D. (1960). *Self-Diffusion of Oxygen in Single Crystal and Polycrystalline Aluminum Oxide*. Journal of Chemical Physics **33** (2): p.480-486.
147. Göbel, M., Rahmel, A. and Schutze, M. (1993). *The Isothermal-Oxidation Behavior of Several Nickel-Base Single-Crystal Superalloys with and without Coatings*. Oxidation of Metals **39** (3-4): p.231-261.
148. Liu, C. T., Sun, X. F., Guan, H. R. and Hu, Z. Q. (2005). *Oxidation of the Single-Crystal Ni-Base Superalloy DD32 Containing Rhenium in Air at 900 and 1000°c*. Surface & Coatings Technology **197** (1): p.39-44.
149. Edmonds, I. E., Evans, H. E., Jones, C. N. and Broomfield, R. W. (2008). *The Kinetics of Oxidation of Ru-Bearing Nickel-Bearing Nickel-Based Superalloys*. Materials Science Forum **595-598**: p.59-67.
150. Suzuki, A. S., Kawagishi, K., Yokokawa, T., Harada, H. and Kobayashi, T. (2011). *Prediction of Initial Oxidation Behavior of Ni-Base Single Crystal Superalloys by Regression Analysis*. Scripta Materialia **65** (1): p.49-52.